UNIVERSIDADE FEDERAL DE SANTA MARIA
CENTRO DE CIÊNCIAS NATURAIS E EXATAS
PROGRAMA DE PÓS-GRADUAÇÃO EM FÍSICA

Hekatelyne Prestes Carpes

CINEMÁTICA E EXCITAÇÃO DO GÁS EM GALÁXIAS COM EMISSÃO MEGAMASER DE OH

Santa Maria, RS
2018

Hekatelyne Prestes Carpes

CINEMÁTICA E EXCITAÇÃO DO GÁS EM GALÁXIAS COM EMISSÃO MEGAMASER DE OH

Tese de Doutorado apresentada ao Programa de Pós-Graduação em Física, Área de Concentração em Física, da Universidade Federal de Santa Maria (UFSM, RS), como requisito parcial para obtenção do grau de **Doutor em Física**.

ORIENTADOR: Prof. Rogemar A. Riffel

COORIENTADORA: Prof.ª Dinalva A. Sales

Santa Maria, RS
2018

Carpes, Hekatelyne
CINEMÁTICA E EXCITAÇÃO DO GÁS EM GALÁXIAS COM EMISSÃO MEGAMASER DE OH / Hekatelyne Carpes.- 2018.
74 p.; 30 cm

Orientador: Rogemar Riffel
Coorientadora: Dinalva Sales
Tese (doutorado) - Universidade Federal de Santa Maria, Centro de Ciências Naturais e Exatas, Programa de Pós-Graduação em Física, RS, 2018

1. Galáxias em Interação 2. Megamaser de OH I. Riffel, Rogemar II. Sales, Dinalva III. Título.

Sistema de geração automática de ficha catalográfica da UFSM. Dados fornecidos pelo autor(a). Sob supervisão da Direção da Divisão de Processos Técnicos da Biblioteca Central. Bibliotecária responsável Paula Schoenfeldt Patta CRB 10/1728.

End. Eletr.: hekatelyne.carpes@gmail.com

Hekatelyne Prestes Carpes

CINEMÁTICA E EXCITAÇÃO DO GÁS EM GALÁXIAS COM EMISSÃO MEGAMASER DE OH

Tese de Doutorado apresentada ao Programa de Pós-Graduação em Física, Área de Concentração em Física, da Universidade Federal de Santa Maria (UFSM, RS), como requisito parcial para obtenção do grau de **Doutor em Física**.

Aprovado em 29 de junho de 2018:

Rogemar A. Riffel, Dr. (UFSM)
(Presidente/Orientador)

Dinalva A. Sales, Dra. (FURG)
(Coorientadora)

Jáderson da Silva Schimóia, Dr. (UFSC)

Juliana Cristina Motter, Dra. (UFFS)

Sandro Barboza Rembold, Dr. (UFSM)

Tiago Vecchi Ricci, Dr. (UFFS)

Santa Maria, RS
2018

DEDICATÓRIA

Aos meus avós Maria Nilza Duarte e Adão Prestes (in memorian)

AGRADECIMENTOS

Agradeço aos meus pais por me darem a vida, pela oportunidade de estudar, pela comida na mesa, pelo afeto, senso de responsabilidade e zelo. Agradeço a minha mãe pelo cuidado incondicional, pela preocupação, por me ensinar a ler e a escrever, me ajudar nos trabalhos da escola e ser um exemplo de honestidade e caráter.

Aos meus avós por cuidarem de mim e serem sempre tão presentes em todos os momentos da minha vida. Por me ensinarem desde cedo que estudar é importante, mesmo que eles não tenham feito isso. Por me buscarem na escola, me ensinarem a jogar baralho, por deixarem eu desmontar as coisas dentro de casa. Ao meu avô por me deixar pegar a máquina de escrever escondido, à minha avó por me ensinar a fazer crochê e por tantas outras coisas que eu guardo com tanto carinho no meu coração.

Aos meus irmãos pela presença que faz eu sentir vontade de ser alguém melhor, para que eles tenham com quem contar independente da situação. Por todas as trocas e pela oportunidade de crescer, aprender a dividir e cuidar. Ao Icaro por ser esse irmão incrível, pela amizade e cumplicidade.

Agradeço ao meu noivo por sonhar os meus sonhos e ser meu maior incentivador. Por ser meu porto-seguro, me dar certezas, leveza e amor. Por ser extremamente paciente e por nunca deixar de sorrir. Por ser a razão da minha vontade de chegar em casa e por fazer o meu café todos os dias.

Ao Pink e ao Guto que sempre foram excelentes companhias nas madrugadas e os melhores ouvintes nos momentos mais difíceis.

Ao meu orientador, Dr. Rogemar A. Riffel por toda confiança que sempre depositou em mim. Pela excelente orientação, por responder os e-mails e por realmente se importar com o andamento do trabalho. Por passar segurança e contagiar com o gosto pela ciência. Por ser extremamente compreensivo, e sempre responder nossas perguntas por mais triviais que pareçam, sem julgamentos. Por ser exemplo de cientista e ser-humano.

Agradeço à minha coorientadora, Dra. Dinalva Sales, por me inserir no projeto e por disponibilizar os dados utilizados neste trabalho, sem os quais não seria possível chegar até aqui.

Agradeço aos meus colegas de laboratório por tornarem o percurso mais alegre. Pela troca de experiências e por todo suporte que só quem passa pela mesma situação pode proporcionar. Por todos os encontros terapêuticos, mate e risadas. Com certeza a vida é bem melhor com os amigos do LAE.

Aos colaboradores dos artigos pelas contribuições, em especial à Dra. Thaisa Storchi-Bergmann e ao Dr. Andrew Robinson pela leitura criteriosa.

And the men who hold high places
Must be the ones who start
To mold a new reality
Closer to the heart
Closer to the heart
The blacksmith and the artist
Reflected in their art
They forge their creativity
Closer to the heart
Yeah, closer to the heart
Philosophers and plowmen
Each must know his part
To sow a new mentallity
Closer to the heart
Closer to the heart
You can be the captain
And I will draw the chart
Sailing into destiny
Closer to the heart
Closer to the heart

(Neil Peart, Peter Talbot - RUSH)

RESUMO

CINEMÁTICA E EXCITAÇÃO DO GÁS EM GALÁXIAS COM EMISSÃO MEGAMASER DE OH

AUTORA: Hekatelyne Prestes Carpes
ORIENTADOR: Rogemar A. Riffel
COORIENTADORA: Dinalva A. Sales

Apresentamos um estudo multicomprimento de onda de galáxias com emissão megamaser de OH. São apresentados dados ópticos de espectroscopia de campo integral obtidos com o instrumento GMOS-IFU, dados rádio obtidos com o radiointerferômetro VLA e dados obtidos com o HST. A partir destes dados foi possível obter informações acerca da dinâmica e excitação do gás nas galáxias IRASF23199+0123 e IRAS03056+2034. Os objetivos que norteiam este trabalho são a identificação do mecanismo central de ionização do gás nesses objetos e propor um cenário capaz de justificar a presença de emissão de megamaser de OH. As observações da galáxia IRASF23199+0123 permitiram mostrar que este sistema é formado por duas galáxias em interação, sendo que no membro leste (IRAS23199E) foram detectadas duas fontes de emissão de megamasers de OH e os dois membros apresentam emissão rádio estendida em 3 e 20cm com pico no núcleo. Os dados ópticos de espectroscopia de campo integral cobrem uma região no interior de IRAS23199E com $\sim$ 6 kpc e com resolução de 2.3 kpc. Os mapas de fluxo construídos a partir desses dados evidenciaram três regiões com emissão extranuclear que foram atribuídas a complexos de formação estelar. Descobrimos a presença de um núcleo Seyfert 1, devido a detecção de uma componente larga, na linha de emissão de Hα proveniente da BLR. Além disso, a análise da cinemática do gás sugere a presença de movimentos não circulares que podem estar associados a presença de outflows provenientes do núcleo e inflow em sua vizinhança. A análise dos dados obtidos para IRAS03056+2034 não indica evidências morfológicas de interação com outras galáxias, mas indica diversas regiões de formação estelar ao longo dos braços espirais. A comparação dos dados obtidos com o instrumento GMOS-IFU e o HST permitiram identificar um anel de regiões de formação estelar circumnuclear. Foram construídos diagramas de diagnóstico que junto com o cálculo da temperatura de brilho e do índice espectral nos permitem concluir que a excitação do gás não se deve apenas a um Starburst, mas também a presença de um AGN. A análise da cinemática do gás sugere a presença de inflows em direção ao núcleo, coincidentes com a posição de um braço espiral descontínuo que é observado em uma imagem obtida com o HST.

Palavras-chave: Galáxias. Dinâmica e Excitação. IRASF23199+0123. IRAS03056+2034

ABSTRACT

GAS KINEMATICS AND EXCITATION IN OH MEGAMASER GALAXIES

AUTHOR: Hekatelyne Prestes Carpes
ADVISOR: Rogemar A. Riffel
CO-ADVISOR: Dinalva A. Sales

We present a multiwavelength study of galaxies that host OH Megamaser emission. We used integral field unit spectroscopic data obtained with the GMOS-IFU instrument, radio data obtained with VLA and HST data for IRASF23199+0123 and IRAS03056+2034. From this data we are able to obtain information about gas dynamics and excitation in the galaxies IRASF23199+0123 and IRAS03056+2034. The main goals of this work are the identification of the central engine that ionizes the gas in these objects e propose a scenario in order to justify the OH megamaser emission. The observations of IRASF23199+0123 allow us to show that this system is formed by two interacting galaxies, in which the eastern member (IRAS23199E) presents two OH Megamaser emission hosts and the two members present extended radio emission in 3 and 20cm with the peak at the nucleus. The IFU spectroscopic data covers the inner region of IRAS23199E with $\sim$ 6 kpc and 2.3kpc of resolution. The flux maps constructed from this data reveal three extranuclear regions that are attributed to star forming complexes. We discovered a Seyfert 1 nucleus in IRAS23199E, due to the detection of a broad component, in the Hα emission-line from the BLR. Besides, the gas kinematics analysis suggests the presence of non circular motions that could be associated to the presence of outflows from the nucleus and inflows in its vicinity. The data analysis for IRAS03056+2034 does not indicate morphological evidence of interactions with other galaxies, but indicates several star forming regions along the spiral arms. The comparison between GMOS-IFU and HST observations allows the identification of a circumnuclear star forming ring. We built diagnostic diagrams that in addiction with the brightness temperature value and spectral index allow us to conclude that the gas excitation is due to not only to Starburst but also due to the presence of an AGN. The analysis of the gas kinematics suggests the presence of inflows towards to the nucleus, and coincident to the position of a patchy spiral arms that is observed in the HST image.

Keywords: Galaxies. Dynamics and Excitation. IRASF23199+0123. IRAS03056+2034

LISTA DE FIGURAS

SUMÁRIO

1 INTRODUÇÃO

1.1 GALÁXIAS EM INTERAÇÃO

Nesta tese estudamos galáxias que apresentam intensa emissão maser de OH. Estas galáxias em geral apresentam algum tipo de interação com o ambiente. Neste capítulo apresentamos uma revisão acerca de galáxias em interação, emissão maser e atividade nuclear em galáxias.

No passado, galáxias eram tratadas como sistemas isolados e não interagentes. Hoje, sabemos que as galáxias estão sujeitas aos efeitos do ambiente no qual estão inseridas, assim como seus halos. De fato, cada halo passa por cerca de três eventos de *major mergers* depois que o progenitor principal adquire 1% de sua massa atual (LI et al., 2007).

O aumento do número de catálogos de galáxias trouxe consigo exemplos de galáxias com morfologias peculiares, com presença de caudas e cor azulada. As características desses sistemas altamente perturbados despertaram interesse no sentido de tentar compreender suas propriedades físicas e químicas. Estudos revelam que as interações entre galáxias são causadoras de um amplo conjunto de fenômenos físicos e morfológicos, como caudas de maré, núcleos cinematicamente desacoplados e aumento da taxa de formação estelar (WOODS; GELLER, 2007). A Figura 1.1 apresenta uma imagem em luz visível da galáxia Arp 188 (a galáxia Girino) obtida com o telescópio espacial Hubble (HST - *Hubble Space Telescope*). A galáxia Girino é um excelente exemplo de galáxias em interação, com caudas de maré facilmente identificáveis.

Encontros colisionais entre dois sistemas não são facilmente compreendidos. Sendo assim, simulações numéricas são utilizadas a fim de prever o comportamento futuro do sistema no que diz respeito a morfologia e alterações em suas propriedades físicas. Todavia, quando a velocidade do encontro dos dois sistemas é muito maior do que a dispersão de velocidades interna (encontro *high-speed*), existe a possibilidade de estimar analiticamente a variação na energia interna do sistema. Por outro lado, se a velocidade do encontro entre os dois corpos não é grande quando comparada a dispersão de velocidades interna do sistema, o encontro pode ocasionar a captura do sistema menos massivo ou ainda os dois corpos se fundirem. Esta última situação recebe o nome de merger galáctico.

O merger galáctico é um tipo de interação bastante violenta. As causas de sua ocorrência variam, bem como a evolução de um merger, dependem fortemente das características dos sistemas envolvidos, tais como a velocidade da colisão, tamanho relativo entre os corpos interagentes, sua composição e ângulos de colisão. Nesse sentido, destacam-se dois tipos de situação: *minor merger* e *major merger*.

Considere $q = M_1/M_2$, onde M_1 e M_2 são as massas de duas galáxias em in-

Figura 1.1 – Imagem da galáxia Arp 188 (Galáxia Girino) obtida com o HST.

Fonte: Imagem gerada a partir de dados do Arquivo do HST. Disponível em https://hypescience.com/wp-content/uploads/2012/11/TadpoleGalaxyPS1V9snyder900.jpg.

teração e $M_1 \geq M_2$. Caso $q \geq 4$ ($q \leq 4$), dizemos que ocorre um minor (major) merger galáctico. Apesar de colisões entre galáxias de tamanhos comparáveis representarem eventos bastante dramáticos, os minor mergers são mais prováveis, ocorrendo com frequências pelo menos uma ordem de magnitude maior do que os major mergers (HERNQUIST; MIHOS, 1995).

Durante o merger de galáxias ocorrem variações no potencial gravitacional que ocasionam alterações das órbitas das estrelas e suas velocidades. As interações entre galáxias são responsáveis pela formação de caudas de maré e de pontes de interação (TOOMRE; TOOMRE, 1972). Além disso, alguns tipos de mergers galácticos apresentam aumento na formação estelar. Com efeito, no momento de fusão torques gravitacionais ocasionam perda de momento angular do gás. Uma consequência imediata disso é o surgimento de fluxos de gás que escoam em direção ao centro da galáxia e fornecem o combustível necessário para desencadear a formação de estrelas (MIHOS; HERNQUIST, 1996; BOURNAUD et al, 2010) . Essa gama de efeitos depende fortemente do ambiente e da época em que se deu a interação.

As galáxias luminosas e ultra luminosas no Infravermelho (em inglês, (U)LIRGs (Ultra) Luminous Infra-red galaxies) recebem esse nome por apresentarem luminosidades que ultrapassam 10^{11} e 10^{12} $L_{\odot}$ respectivamente, no Infravermelho (8 – 1000 μm) (SOIFER et al., 1987). Sabemos que esses objetos são tipicamente o resultado de interações e/ou mergers galácticos (SANDERS; MIRABEL, 1996).

A descoberta dessa nova classe de objetos foi protagonizada pelo satélite IRAS (Infrared Astronomy Satellite), lançado em janeiro de 1983. Suas observações cobriram cerca de 96$\%$ do céu nas bandas centradas em 12, 25, 60 e 100 μm, permitindo a detecção de cerca de 350 mil fontes de emissão infravermelha. As informações coletadas pelo satélite IRAS de LIRGs e ULIRGs foram organizadas por SOIFER (1987) em um catálogo de galáxias usando observações em 60 μm, e ficou conhecido como BGS (Bright Galaxy Sample). Uma revisão desse catálogo foi realizada em 2005 por SANDERS $\&$ MIRABEL (1996) e incorporada ao RBGS (Revised Bright Galaxy Sample).

1.2 EMISSÃO ESTIMULADA: MASER E MEGAMASERS

Elétrons estão dispostos em orbitais de maneira discreta, assumindo diferentes energias em cada nível quântico, podendo transitar entre os mesmos. Um elétron excitado pode decair para um estado de menor energia que não esteja previamente ocupado. No momento do decaimento, ocorre a emissão de um fóton. Caso essa situação ocorra sem influência externa, a emissão é dita espontânea e a fase e direção associadas ao fóton são aleatórias. Porém, pode ocorrer que um fóton com energia específica atinja o elétron excitado, ocasionando seu decaimento para um nível menos energético e dando origem a um novo fóton com as mesmas características do fóton incidente. Esse tipo de emissão é dita estimulada e sua formulação teórica foi desenvolvida por Albert Einstein em 1917.

MASERs (Microwave Amplification by Stimulated Emission of Radiation) astronômicos figuram entre as importantes descobertas da astronomia molecular. Os MASERs apresentam características interessantes pois todos os fótons que são emitidos como resultado da emissão estimulada apresentam a mesma energia, fase, polarização e direção do fóton incidente. O campo magnético que está associado ao fóton em movimento causa a oscilação de átomos ou de moléculas. Tal oscilação, que está diretamente relacionada às propriedades do fóton incidente, transfere essas propriedades aos próximos fótons que estão sendo gerados por emissão estimulada. Essa radiação amplificada pode ser identificada nos espectros como sendo linhas de emissão bastante intensas e estreitas, como ilustrado na Figura 1.2, que apresenta exemplos de espectros com emissão MASER de água descobertos na direção do núcleo de oito galáxias.

Os fótons produzidos por emissão estimulada poderiam ser absorvidos ao invés de continuarem perturbando outros elétrons, mas isso não ocorre. De fato, considere um

Figura 1.2 – Espectros com emissão maser de água descobertos em direção ao núcleo de oito galáxias (identificadas em cada painel). A linha vertical acima de cada espectro representa a velocidade sistêmica da galáxia e a incerteza correspondente de $\pm$ 1 σ é indicada pela barra horizontal.

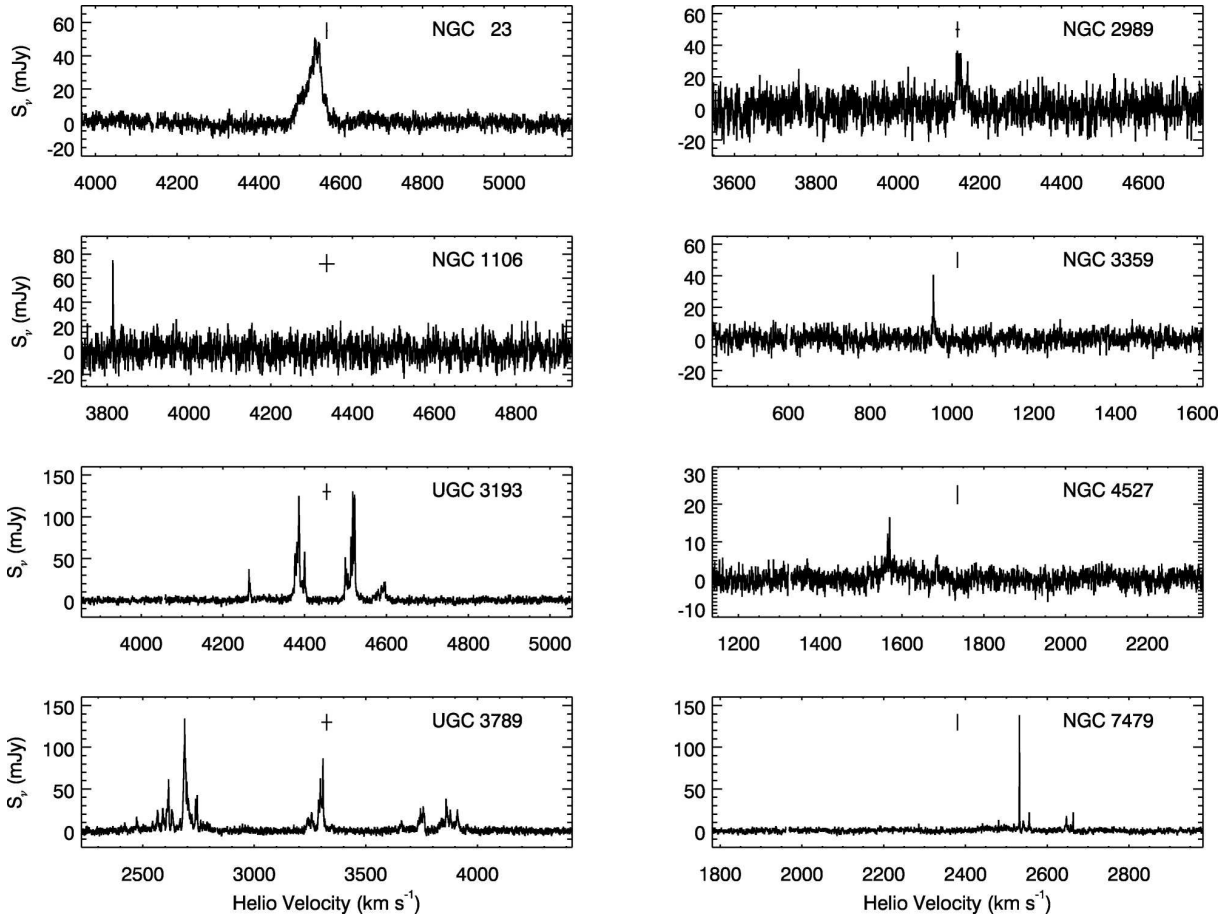

Fonte: Imagem retirada de (BRAATZ; GUGLIUCCI, 2008).

sistema quântico com apenas dois estados E_1 e E_2 (com N_1 e N_2 partículas, respectivamente), E_1 o estado fundamental e que a taxa de fótons absorvidos produzidos por emissão estimulada seja diretamente proporcional a N_1 ou N_2, respectivamente.

Se $N_1 > N_2$, a absorção ocorre mais rápido do que a emissão estimulada, e nesse caso não há a produção de um MASER. Se $N_1 = N_2$, a taxa de fótons produzidos por emissão estimulada será igual a taxa de fótons absorvidos e não há a produção de um maser. Já no caso em que $N_2 > N_1$, isto é, quando há um maior número de partículas no estado excitado do que no estado fundamental (*inversão da população*) há produção de MASER. Nesse caso, a taxa com a qual os fótons são produzidos através de emissão estimulada é maior do que a taxa com a qual os fótons são absorvidos. Dessa forma, haverá um número de fótons emitidos por emissão espontânea que irá realimentar o sistema proporcionando que a emissão estimulada continue acontecendo e favorecendo a produção de um MASER. A figura 1.3 apresenta um esquema demonstrando de forma simplificada o processo

de emissão estimulada.

Figura 1.3 – Representação esquemática do processo de emissão estimulada

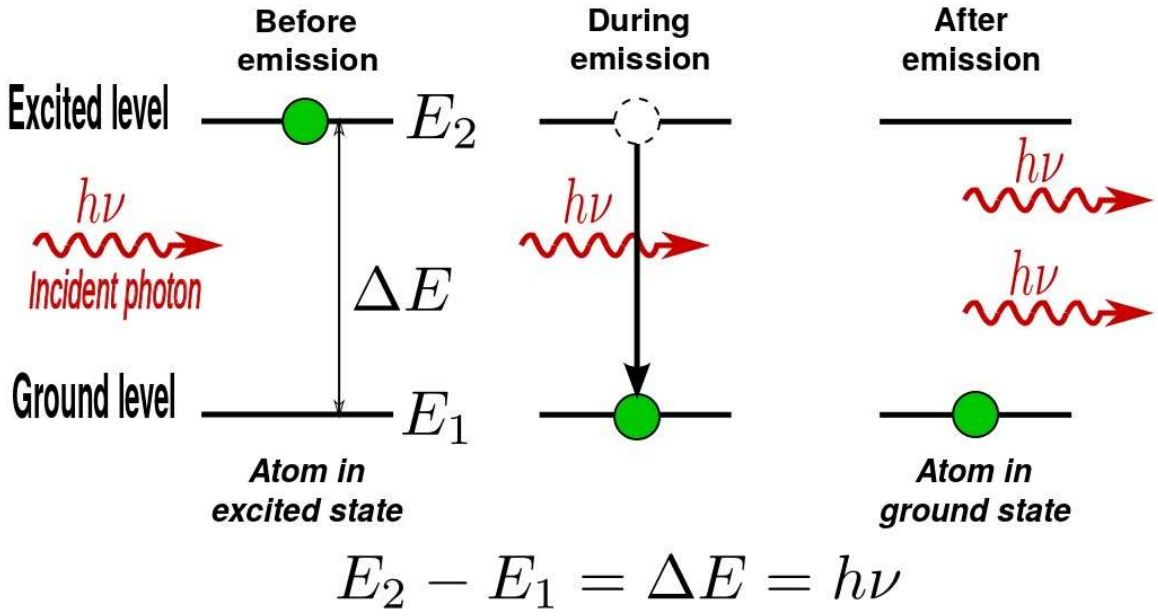

Fonte: https://upload.wikimedia.org/wikipedia/commons/0/09/StimulatedEmission.svg

Para que ocorra a inversão da população dos níveis, é necessário um sistema quântico com três estados ou mais. Com efeito, considere três estados E_1 (com N_1 partículas), E_2 (com N_2 partículas) e E_3 (com N_3 partículas) como sendo o estado fundamental, o primeiro estado excitado e o segundo estado excitado, respectivamente. Se todas as partículas estão dispostas no estado E_1 e uma grande quantidade de energia for acrescida ao sistema (*pumping*), a maioria das partículas irá para o estado E_3.

Alguns elétrons do estado E_3 irão emitir fótons de maneira espontânea e decair para o estado E_2, assim como alguns elétrons que decairam para o estado E_2 irão emitir espontaneamente um fóton e decair para E_1. Se o tempo de uma transiçao ($E_3 \rightarrow$E$_2$) for menor do que para ocorrer a transição ($E_2 \rightarrow$E$_1$) então podemos concluir que mais elétrons irão permanecer em E_2 do que em E_1 ou E_3. O que ilustra a situação $N_2 > N_1$ e em outras palavras significa que ocorreu a inversão da população.

MASERS galácticos costumam ser emitidos em regiões de formação estelar e próximos a objetos estelares jovens, como proto estrelas e regiões HII compactas. Moléculas foram detectadas pela primeira vez no meio interestelar em 1940 quando linhas de absorção de CH, CH^+ e CN foram evidenciadas no espectro de estrelas quentes (SWINGS; ROSENFELD, 1937). Essas moléculas apresentam transições na parte visível do espectro eletromagnético e portanto são passíveis de detecção por telescópios ópticos. Depois disso, em 1963, foi descoberto o radical OH, hidroxila (WEINREB et al., 1963). Por cerca de 5 anos, a hidroxila foi a única molécula perceptível em rádio até que entre 1968 e 1969 foram descobertas as moléculas NH_3 (CHEUNG et al., 1969), H_2CO (SNYDER et al.,

1969) e H_2O (CHEUNG et al., 1969). Nesse período ocorreu um grande desenvolvimento da astronomia molecular e tornou-se evidente que moléculas complexas poderiam formar-se no meio interestelar, sendo que mais de 70 moléculas já foram descobertas no meio interestelar.

Na Via Láctea, existe evidência de emissão MASER de OH, H_2O, SiO e CH_3OH (REID, 2002). Todas as fontes emissoras parecem ter sido originadas em gás molecular quente presente em regiões de formação estelar (GENZEL et al., 1978) e fortemente associadas a regiões HII ultra-compactas, fontes de emissão infravermelha obscurecidas e com ejeções de matéria.

A primeira detecção de emissão MASER de água em uma fonte extragaláctica ocorreu em 1977. Localizada na região HII IC133 e pertencente ao disco de M33, a emissão foi detectada pelo rádio interferômetro Effelsberg de 100 m de diâmetro (CHURCHWELL et al., 1977). As características da emissão maser extragaláctica se mostraram semelhantes as dos masers encontrados na Galáxia. No ano seguinte, outros masers foram detectados em regiões diferentes de M33 e IC342 (HUCHTMEIER et al., 1978).

Logo em seguida, em 1979, o rádio telescópio brasileiro de 13,7 m situado em Itapetinga, detectou emissão maser de água em NGC 4945. Na época, esse era o maser extragaláctico mais intenso, sendo 10 vezes mais brilhante do que os masers galácticos detectados até então (SANTOS; LEPINE, 1979). Uma segunda emissão maser de água mais intensa foi detectada pouco tempo depois pelo telescópio Parkes de 64 m e a fonte era a galáxia Circinus (GARDNER; WHITEOAK, 1982). Essas detecções favoreceram a hipótese de que os masers provém de regiões altamente densas e de intensos campos de radiação, alimentados por estrelas jovens e quentes, em nuvens moleculares situadas nos núcleos galácticos (GARDNER; WHITEOAK, 1982).

Outras detecções desse tipo foram possíveis com o radiotelescópio *Owens Valley Radio Observatory*, de 40 m, que realizou um survey procurando especificamente masers extragalácticos como os citados anteriormente. O resultado foi a detecção de mais quatro fontes de emissão de maser de água em NGC 4285, NGC 1068, M 82 e NGC 6946 (CLAUSSEN; HEILIGMAN; LO, 1984; CLAUSSEN; LO, 1986).

Masers de água extragalácticos apresentam luminosidades que chegam a 450 $L_\odot$. No princípio, as altas luminosidades desse tipo de emissão eram atribuídas a um grande número de masers interestelares, como os encontrados em W49N, situados em regiões de surtos de formação estelar. Assim, as estrelas jovens e quentes seriam as responsáveis por fornecer o *pumping* que origina o maser (GARDNER; WHITEOAK, 1982)(CLAUSSEN; HEILIGMAN; LO, 1984). Entretanto, observações de alta resolução espacial realizadas pelo telescópio VLA (Very Large Array) mostraram que a variação da emissão maser ocorre em questão de poucos meses. Esse fato invalidou o modelo no qual acreditava-se que a grande luminosidade dos masers de água era resultado da soma das luminosidades de masers independentes, cada um deles alimentado pelo grande número de estrelas jovens

presentes em starbursts (CLAUSSEN; LO, 1986).

Em seguida, foi proposto que a luminosidade dos masers de água poderia ser originada em nuvens densas de gás em um disco circumnuclear excitado por um núcleo ativo (CLAUSSEN; LO, 1986). O ponto central para criação dessa hipótese é de que os masers nucleares de água não são iguais aos masers galácticos, pois seriam originados em nuvens densas e sua fonte de energia seria um AGN e não as estrelas quentes que estariam na região.

A fonte de emissão maser em NGC 4258, detectada com o VLBA (*Very Long Baseline Array*) por CLAUSSEN et al. (1984) forneceu uma importante evidência observacional para explicar a existência de um disco Kepleriano de acreção no núcleo galáctico, corroborando assim o paradigma corrente de que a acreção de matéria por um buraco negro supermassivo é o mecanismo que justifica a emissão de energia extremamente intensa em Núcleos Ativos de Galáxias (AGNs – *Active Galactic Nuclei*)(SALPETER, 1964; LYNDEN-BELL, 1969). A emissão do megamaser de água nesse objeto também foi utilizada como ferramenta para mapear o toróide em torno de um AGN (MIYOSHI, 1996).

A detecção de masers também é relevante no que diz respeito à determinação de distâncias extragalácticas. Medidas do movimento próprio de masers associados à M33, por exemplo, foram realizadas com o intuito de determinar a distância até esta galáxia (BRUNTHALER et al, 2002; ARGON et al, 2004) . Emissão maser de água foi encontrada em NGC 4258. A emissão partindo do disco de acreção também foi utilizada nesse caso para inferir distâncias até galáxias externas. Partindo de algumas hipóteses, a medida realizada e a análise do mapeamento das órbitas circulares do gás forneceram o valor de distância de 7.2 $\pm$ 0.5 Mpc (HERRNSTEIN et al., 1999). Até agora, essa é a determinação mais precisa de distância até um objeto extragaláctico. O buraco negro supermassivo com a estimativa de massa mais precisa é o de NGC 4258, de 3.9 $\times 10^7 M_\odot$, determinada devido à presença de emissão maser(HERRNSTEIN et al., 1998).

Foram detectadas emissões maser de H_2O e OH em galáxias externas, com luminosidades cerca de 10^6 vezes maior do que a dos masers galácticos típicos (SANTOS; LEPINE, 1979; BAAN; WOOD; HASCHICK, 1982). Essas detecções com luminosidades extremas receberam o nome de megamasers. Megamasers ocorrem em geral, em regiões com abundância de gás molecular de alta densidade (> 10^6 cm^{-3}). No caso de megamasers de água, essas regiões ficam localizadas a alguns parsecs de distância de um AGN, ou dentro de uma região nuclear de cerca de 100 parsecs em galáxias Starburst no caso de megamasers de OH.

1.2.1 Megamasers de OH

As linhas de emissão megamaser de OH costumam ser encontrados em LIRGs, diferente dos megamasers de água. Os primeiros megamasers extragalácticos de OH foram detectados na galáxia espiral NGC253 (WHITEOAK; GARDNER, 1973); (GARDNER; WHITEOAK, 1975) e logo em seguida em M82. A emissão proveniente dessas fontes surpreendeu por sua intensidade que era cerca de dez vezes mais brilhante do que a associada outros masers galácticos.

Um exemplo de fonte de emissão megamaser de OH é a galáxia ARP220, identificada com o telescópio Arecibo (BAAN; WOOD; HASCHICK, 1982). Apresentando luminosidade de 400 $L_{\odot}$, cerca de 10^8 vezes maior do que a dos masers encontrados em W3(OH), sendo a emissão não polarizada. Essas propriedades são semelhantes às dos masers encontrados em NGC253 e M82, mas com um alargamento significativo na linha de emissão de OH (400 km s^{-1}) e luminosidade maior, que pode ser resultado da presença de muitos masers de OH associados com regiões HII (BAAN; WOOD; HASCHICK, 1982).

A descoberta do megamaser de ARP220 implicou na realização de um *survey* com objetivo de encontrar outros megamasers de OH usando telescópios de grande área coletora. Sob o cenário de que emissão megamaser de OH é a amplificação de um contínuo em rádio que aparece em segundo plano, foram realizadas observações que procuravam emissão megamaser em galáxias com absorção de H I, contínuo forte em rádio, fontes de radiação infravermelha, galáxias IRAS e Markarian (BAAN, 1985)(SCHMELZ et al., 1986).

No início da procura por megamasers de OH, a cada 240 galáxias candidatas a propiciar a emissão, apenas três apresentavam de fato (BAAN; HASCHICK; SCHMELZ, 1985). Foi proposta a associação do fenômeno megamaser de OH com atividades *starburst*, pois o meio em que elas ocorrem é o mesmo que fornece condições para emissão megamaser. Dentre elas, forte radiação infravermelha, gás com alta densidade e presença de fontes de emissão rádio (BOTTINELLI et al., 1985).

Emissão megamaser de OH pode ser utilizada justamente para traçar regiões de alta densidade [n(H_2)=$10^{5-7}$$cm^{-3}$] e especula-se que uma separação nas componentes da emissão megamaser pode estar associada a ejeções de matéria de pouca densidade, mas a altas velocidades (BAAN; HASCHICK; HENKEL, 1989).

O cenário de que nesse tipo de emissão há a amplificação do contínuo rádio presente nas LIRGs não é totalmente aceito. Razões para o descrédito nessa hipótese ficaram mais evidentes a partir dos dados obtidos com o VLBI para ARP220. Nesse levantamento, foi constatado que cerca de dois terços da emissão maser proveniente desse objeto é produzida em estruturas com volume de poucos pc^3, geralmente partindo de dentro do núcleo de ARP220 , mas sem coincidir com a emissão relacionada com a amplificação do contínuo em rádio (LONSDALE et al., 1998).

Outros megamasers de OH foram detectados com VLBI tendo como fontes IIIZW35,

IRAS17208-0014 (DIAMOND et al., 1999), IRAS12032+1707 (LONSDALE et al., 2003), Mrk231 (KLÖCKNER; BAAN; GARRETT, 2003), Mrk273 (KLÖCKNER; BAAN, 2004) e IRAS14070+0525 (PIHLSTRÖM et al., 2005), sendo que as últimas apresentam emissão estendida em um disco circumnuclear, o que corrobora o modelo proposto.

Com o intuito de expandir a amostra de megamasers já catalogados, foi realizado um survey em 300 galáxias IRAS em $z > 0.1$ com o telescópio Arecibo (DARLING; GIOVANELLI, 2002). O resultado foi a detecção de mais de 100 megamasers de OH em galáxias luminosas no infravermelho.

1.3 STARBURSTS E NÚCLEOS ATIVOS EM GALÁXIAS EM INTERAÇÃO

Sabemos que ULIRGs são objetos extremamente luminosos e que são possivelmente o resultado da fusão de galáxias (SANDERS et al., 1987);(KIM et al., 2002). O que ainda não está bem estabelecido são os agentes desencadeadores de toda essa emissão no infravermelho. Os dois fenômenos apontados como os principais são a presença de um AGN ou formação estelar intensa (Starburst). ULIRGs podem abrigar tanto Starbursts quanto AGNs e em algumas ocasiões esses fenômenos podem coexistir (SANDERS; MIRABEL, 1996).

A maior dificuldade encontrada no estudo óptico desses objetos é que ULIRGs são ambientes extremamente encobertos de poeira e a observação de suas regiões centrais é uma tarefa difícil. A precisão nas conclusões depende fortemente da qualidade das informações obtidas, mas em alguns casos as linhas de emissão são muito fracas, dificultando a análise. Evidências sugerem que em alguns casos a poeira nuclear é espessa até mesmo para observações realizadas em raios X, o que sugere que a identificação equivocada de AGNs não acontece com frequência (DARLING; GIOVANELLI, 2006).

Enquanto os detalhes sobre a fonte de energia nas ULIRGs permanecem incertos, a conexão causal entre a atividade ultra luminosa e as interações galácticas é evidente. ULIRGs, em sua maioria, apresentam evidências morfológicas de fortes interações, através de núcleos duplos, distorcidos e assinaturas de caudas de maré. Ainda que a recíproca não seja verdadeira, isto é, nem todas as galáxias que interagem fortemente apresentam atividade ultraluminosa. Nesse sentido, podemos citar as galáxias Antena (NGC4038 e NGC4039 – mostrada na Figura 1.4) ou NGC7252, que passaram por colisões violentas mas apresentam luminosidades que são uma ordem de magnitude menores do que as ULIRGs mais extremas.

Sobre o mecanismo central nesses objetos ser um starburst ou um AGN, o primeiro pré-requisito é que exista um enorme suprimento de combustível na forma de gás. Caso as colisões nesses sistemas sejam suficientes para levar gás dos discos galácticos para os núcleos, os inflows de gás podem ser os responsáveis por alimentar esse mecanismo.

No momento em que o gás atinge o interior do sistema, ele pode se fragmentar e formar estrelas (a uma taxa de aproximadamente 100 $M_{\odot}$/ano para fornecer a luminosidade observada) ou continuar a fluir para o interior da galáxia ou abastecer um AGN.

1.4 MOTIVAÇÃO E OBJETIVOS

O presente trabalho tem o objetivo de identificar o mecanismo central de geração de energia (AGN e/ou Starburst) em galáxias com emissão megamaser de OH e propor um cenário que justifique a presença de emissão megamaser para dois sistemas: IRAS23199+0123 e IRAS03056+2034, que são (U)LIRGs fontes de emissão megamaser de OH. Galáxias com essa emissão característica formam uma subclasse de ULIRGs emitindo em 1665 e 1667 MHz. Existem evidências de que esses objetos abriguem um AGN com alto potencial energético que ainda está imerso em densas camadas de poeira e gás (HO, 2005). Estudos sugerem ainda a presença de um toroide, previsto pelo modelo unificado de AGNs (ANTONUCCI, 1993). Estudar essa classe de objetos é importante para compreender o processo de formação estelar, crescimento do buraco negro supermassivo e a natureza do gás envolvido nesses ambientes de fusão.

Nessa tese apresentaremos os resultados obtidos através de uma análise espectroscópica óptica de campo integral (IFU) com a finalidade de estudar a dinâmica e a excitação do gás presente nos núcleos desses objetos. Os dados espectroscópicos são complementados com imagem de banda larga e estreita no ótico e imagens rádio. Esse trabalho tem como objetivos específicos:

- Mapear a cinemática e excitação do gás nas regiões centrais dos objetos utilizando espectroscopia de campo integral;
- Comparar as distribuições de fluxos com a imagem em grande escala obtidas com o telescópio espacial Hubble a fim de identificar estruturas morfológicas, regiões de formação estelar;
- Analisar os mecanismos de excitação do gás através de razões de linhas e diagramas de diagnóstico;
- Ajustar um modelo de disco em rotação aos campos de velocidades observados;
- Analisar os resíduos dos ajustes do campo de velocidades ao modelo de disco em rotação a fim de identificar inflows/outflows de gás;
- Comparar os dados obtidos com as imagens rádio, buscando por associações entre os resíduos do modelo cinemático e estruturas de emissão em rádio, a fim de identificar/correlacionar estruturas;

- Estimar valores para as propriedades físicas das regiões de formação estelar, tais como: massa de gás ionizado, taxa de formação estelar, e taxa de fótons ionizantes.

Esse trabalho está estruturado da seguinte forma: no Capítulo 2 serão apresentados detalhes sobre a obtenção e redução dos dados. No capítulo 3 apresentamos detalhe sobre a metodologia deste trabalho. No capítulo 4 apresentaremos os resultados obtidos para IRASF23199+0123 na forma de artigo. No capítulo 5 apresenta-se o artigo referente a galáxia IRAS03056+2034. No capítulo 6 são apresentadas as conclusões e perspectivas deste trabalho.

Figura 1.4 – Imagem composta (HST e ALMA) da galáxia Antena. O azul representa a radiação visível (estrelas jovens). As observações realizadas com o ALMA aparecem em vermelho, rosa e amarelo e evidenciam nuvens de gás denso e frio que dão origem a novas estrelas.

Fonte: Imagem retirada de *https://www.eso.org/public/images/eso1137a/*

2 OBTENÇÃO E REDUÇÃO DOS DADOS

Os dados obtidos para realização desse trabalho fazem parte de um estudo multi-comprimento de onda de galáxias OH Megamaser com o objetivo de relacionar o estado de fusão (merger) das galáxias à fase de evolução/crescimento do núcleo ativo e/ou Starburst nuclear, bem como a concentração e estrutura do gás ionizado na região central (em escalas de sub-kiloparsec).

O projeto ao qual os dados estão vinculados consiste no estudo de uma amostra de 15 galáxias com emissão Megamaser de OH que já foram observadas com o Telescópio Espacial Hubble, com a *Advanced Camera for Surveys* (ACS) usando os filtros de banda larga F814W e banda estreita FR656N nas linhas de Hα+[NII]. Estas imagens fornecem informações acerca da emissão contínua na banda I e da emissão do gás. Além disso, o projeto conta com dados de arquivo do *Very Large Array* (VLA), nas bandas X (8-10 GHz), L (1-2 GHz) e das linhas do maser de OH (1665/1667 MHz) na banda L, e dados espectroscópicos ópticos que foram coletados utilizando o instrumento GMOS do telescópio Gemini (instrumento GMOS-IFU) para alguns dos objetos da amostra.

Nessa tese, analisamos dados obtidos com os instrumentos Gemini Multi-Object Spectrograph (GMOS) dos telescópios Gemini operando no modo de Unidade de Campo Integral (IFU – *Integral Field Unit*), com o HST e VLA para as galáxias IRAS23199+0123 e IRAS03056+2034. IRAS23199+0123 apresenta redshift z=0.13569, o que corresponde a uma distância de 558 Mpc, onde 1$''$ corresponde a 2.7 kpc na galáxia, assumindo a constante de Hubble como H_0=73 Km^{-1}Mpc^{-1}. A fonte de emissão megamaser foi detectada pelo telescópio Arecibo em um survey que coletou informações sobre 52 objetos, com 0.1< z <0.26 (DARLING; GIOVANELLI, 2001). A Figura 2.1 mostra o espectro extraído do trabalho citado. DARLING $\&$ GIOVANELLI (2006) realizaram um estudo espectroscópico com dados obtidos com o telescópio Palomar com o objetivo de estudar as propriedades dos objetos catalogados com o survey. Nesse estudo, identificaram que a emissão nuclear de IRASF23199+0123 é devido a presença de um núcleo Seyfert, baseado na análise das razões das linhas de emissão.

IRAS03056+2034 é uma galáxia espiral [SB(rs)B (VAUCOULEURS et al., 1991)] que apresenta emissão megamaser de OH. A detecção desta emissão foi realizada utilizando o telescópio Nancay, em 1990 (BOTTINELLI et al., 1990). BAAN et al., (1998) realizaram um estudo espectroscópico com dados obtidos com o telescópio Hale no Observatório Palomar e obtiveram a classificação espectral de 42 galáxias megamaser de OH, baseada em razões de linhas. Uma das consequências desse estudo foi a classificação de IRAS03056+2034 como uma galáxia Starburst.

2.1 DADOS OBTIDOS COM O INSTRUMENTO GMOS-IFU

A coleta dos dados espectroscópicos ópticos foi realizada utilizando os Telescópios Gemini de 8.1 metros de diâmetro. Os telescópios Gemini estão localizados em Mauna Kea (Gemini Norte), no Havaí e em Cerro Pachón (Gemini Sul), no Chile, fornecendo cobertura total de ambos hemisférios celestes. Os dados foram obtidos utilizando o instrumento GMOS (HOOK et al., 2004) no modo IFU (ALLINGTON-SMITH et al., 2002). A configuração utilizada durante a coleta dos dados deste trabalho permite a obtenção de 1500 espectros (um para cada fibra) simultaneamente, sendo 1000 espectros do campo principal e 500 do campo do céu. Os campos principal e do céu são compostos por um arranjo de lentes hexagonais que cobrem $7'' \times 5''$ do campo principal e $3.5'' \times 5''$ do campo do céu quando opera no modo duas fendas. Já quando opera no modo uma fenda, as lentes cobrem $3.5'' \times 5''$ do campo principal e $1.75'' \times 5''$ do campo do céu.

Durante as observações, a luz é coletada e atinge os dois arranjos de lentes hexagonais sendo conduzida através de fibras ópticas até o espectrógrafo. Este apresenta dois caminhos ópticos, um que é otimizado para o vermelho e o outro para o azul. É possivel realizar o bloqueio do caminho óptico “azul” e quando isso ocorre, a metade “vermelha” do arranjo apresenta cobertura espectral máxima. Já quando as duas metades são utilizadas simultaneamente (modo duas fendas), a cobertura espectral diminui pela metade e a cobertura espacial dobra. Nos dois modos de observação os espectros incidem em um conjunto de 3 detectores com um pequeno “gap” entre eles que corresponde a poucos ângstrons.

Com a unidade de campo integral são obtidos espectros de um campo bidimensional e é possível gerar à partir deles um cubo de dados. Como mostrado na figura 2.2, um cubo de dados fornece informações em três dimensões, sendo duas dimensões espaciais e uma espectral. Dessa forma, é possível extrair um espectro para cada pixel espacial do cubo de dados ou ainda construir imagens em uma faixa espectral específica.

A obtenção dos dados espectroscópicos ópticos para IRASF23199+0123 foi realizada com o telescópio Gemini Sul, sob o projeto GS-2013B-Q-97 (PI: Dinalva Sales), em 29 de agosto de 2013. Os dados obtidos com o instrumento GMOS correspondem apenas à região central da galáxia ao leste, visto que IRASF23199+0123 é um par de galáxias, conforme imagens obtidas com o Telescópio Hubble. Dessa forma, o núcleo leste foi escolhido para ser observado por apresentar estrelas guias brilhantes presentes no campo de observação e possuir uma emissão mais compacta nas imagens do HST. Nesse momento, não sabíamos que IRASF23199+0123 era um par de galáxias e nem tínhamos informações sobre a localização do megamaser. O eixo maior da IFU foi orientado ao longo do PA=215°, aproximadamente ao longo do eixo maior da galáxia. As observações foram realizadas com o GMOS operando no modo uma fenda. O tempo total de exposição foi de 4800 segundos e foi dividido em quatro exposições individuais de 1200 segundos. As

observações foram realizadas com a rede B600 combinada com o filtro GG455. Essa configuração resultou em uma cobertura espacial de $5.0'' \times 3.5''$ e em uma cobertura espectral de 450 até 750 nm, com resolução espectral de 1.7 Å, que foi obtida medindo a largura a meia altura (Full Width at Half-Maximum - FWHM) de linhas de emissão típicas da lâmpada de Ar utilizado para calibrar os espectros em comprimento de onda, e observados na mesma noite das observações da galáxia. A resolução angular de 0.85" foi estimada através da medida do FWHM das estrelas de campo presentes na imagem de aquisição, e que corresponde a $\sim$2.3 kpc na galáxia.

Os dados de espectroscopia óptica para IRAS03056+2034 foram obtidos com o Telescópio Gemini Norte, nos meses de Outubro, Novembro e Dezembro de 2013, sob o projeto GN-2013B-Q-97 (PI: Dinalva Sales). As observações foram realizadas com o GMOS operando no modo fenda única, com a rede B600 combinada com o filtro G5307 e com o eixo maior da IFU orientada ao longo do PA=120°, aproximadamente ao longo do eixo maior da galáxia. O tempo total de integração foi de 12000 segundos, separadas em 10 exposições individuas de 1200 segundos. As observações cobriram um intervalo espectral que inclui as linhas Hα, [NII]λ6583, [SII]λ6717, Hβ, [OIII]λ5007 e [OI]λ6300. Os dados obtidos apresentaram resolução espectral de 1.8 Å, que foi obtida através da medida do FWHM das linhas de emissão da lâmpada de Ar que foi utilizada para calibrar em comprimento de onda, correspondendo a 90 km s^{-1}. E uma resolução angular de 0.9″, obtida a partir da medida do FWHM de estrelas de campo presentes na imagem de aquisição, e correspondendo a 506 pc na galáxia.

2.1.1 Processamento dos dados obtidos

O processo de redução dos dados de espectroscopia óptica foi realizado utilizando o software IRAF (*Image Reduction and Analysis Facility*) e os pacotes desenvolvidos para a redução dos dados dos Telescópios Gemini, em particular para o instrumento GMOS. Os procedimentos para redução dos dados deste trabalho seguem o padrão realizado para redução de dados espectroscópicos.

Primeiro é realizado um seccionamento da imagem, para que possamos determinar a área útil da mesma (excluir as bordas do CCD). Logo após foi subtraído o nível de pedestral eletrônico do CCD, utilizando imagens de bias. Isso se faz necessário pois a cada pixel da imagem é associado um valor de contagens que independe do tempo de exposição e do objeto observado.

Para corrigir a variação fibra a fibra ao longo do CCD, todas as imagens foram divididas pela imagem de flat-field normalizada.

Para o tipo de observação realizada, determinamos o traço dos espectros sobre o detector e realizamos a extração dos mesmos. Depois da extração, é determinada a varia-

ção pixel-a-pixel ao longo do caminho de extração dos espectros e aplica-se essa correção aos espectros do objeto, já extraídos. Logo em seguida, é realizada calibração em comprimento de onda, subtração do céu e calibração em fluxo. A calibração em comprimento de onda é realizada tomando-se como base linhas de emissão presentes no espectro de uma lâmpada observada na mesma noite da obtenção dos dados de ciência. A calibração relativa em fluxo foi realizada integrando-se o espectro de uma estrela padrão como referência, observada como parte das calibrações padrão do projeto e não necessariamente na mesma noite e condições fotométricas da observação dos dados para as galáxias.

A etapa final, consiste em gerar os cubos de dados, com amostragem espacial de $0.1'' \times 0.1''$. São obtidos um cubo para cada exposição do objeto e eles são combinados logo em seguida, através de uma média realizada pela tarefa *gemcombine*. Durante a combinação dos cubos foi utilizado como referência o pico da emissão do contínuo e ainda foi realizada a descontaminação por raios cósmicos com o algortimo *avsigclip*. O resultado desse procedimento é um único cubo de dados para cada objeto, através do qual serão realizadas as medidas e posterior análise.

2.2 OBTENÇÃO E REDUÇÃO DOS DADOS COLETADOS COM O HST

O HST é um telescópio espacial refletor com espelho principal de 2,4 metros de diâmetro e conta com cinco instrumentos que atuam desde o infravermelho, passando pelo óptico até o ultravioleta. Foi lançado pela NASA em abril de 1990 a bordo do ônibus espacial Discovery e foi equipado com câmeras e espectrógrafos. A energia que mantém o telescópio em funcionamento provém de dois painéis solares de 2,45 m $\times$ 7,56. O Telescópio tem 13,2 metros de comprimento, 4,2 metros de diâmetro e massa de 11 110 kg no momento de seu lançamento.

Neste trabalho foram utilizados dados obtidos com o HST para ambas as galáxias estudadas. As imagens de IRASF23199+0123 e IRAS03056+2034 foram coletadas utilizando a câmera ACS (Advanced Camera for Surveys), conforme mencionado anteriormente, e pertencem a um survey com o objetivo de observar uma amostra de galáxias megamaser (Programa 11604; PI: D. J. Axon). O tempo total de integração foi de 600 segundos com o filtro de banda larga F814W, 200 segundos com o filtro de banda média FR914M e 600 segundos com o filtro de banda estreita FR656N banda estreita, que inclui as linhas de H_α e [NII] λ6548, 6583.

O processamento das imagens[1] foi realizado utilizando o software IRAF. Primeiramente foi realizada a remoção dos raios cósmicos com a tarefa LACOS (DOKKUM, 2001). Para construção da imagem de Hα+[NII] foi estimada primeiramente a taxa de contagem

[1] A redução dos dados obtidos com o HST foi realizada por colaboradores do projeto

de algumas estrelas tanto para a banda média (FR914M) quanto para a banda estreita (FR656N). Esse procedimento permitiu definir um fator de escala médio que foi aplicado às imagens de banda média. Como resultado disso, foi obtida uma nova imagem corrigida que foi subtraída da imagem de banda estreita. Finalmente, a imagem final foi inspecionada para garantir que os resíduos nas posições das estrelas de fundo fossem insignificantes. Esse procedimento resulta em incertezas típicas que variam de 5 até 10 % para o fluxo.

2.3 OBTENÇÃO E REDUÇÃO DOS DADOS COLETADOS COM O RADIOINTERFERÔMETRO VLA

O telescópio *Karl G. Jansky Very Large Array* (VLA) é um radiointerferômetro que está situado na Planície de San Augustin, no Novo México. Localiza-se a 2124m acima do nível do mar e faz parte do *National Radio Astronomy Observatory* (NRAO). O interferômetro é formado por 27 antenas independentes, cada uma com um disco de 25 metros de diâmetro. As antenas estão dispostas ao longo de três braços com 21 km cada, formando uma estrutura em forma de Y e que podem ser realocadas. As diferentes configurações do arranjo interferométrico resultam em resoluções angulares de 0.2"a 0.04", com cobertura espectral de 74 MHz até 50 GHz.

IRASF23199+0123 foi observada com o VLA em 20 de abril de 2014. As observações incluíram imageamento nas bandas X (8-10 GHz/ contínuo) e L (1-2 GHz/ contínuo) e observações espectroscópicas na banda L, com espectro centrado nas linhas maser de OH em 1665 e 1667 MHz. As observações das bandas L e X incluíram, respectivamente, exposições de três e dez minutos alternando com exposições de três minutos do calibrador de fase J2310+0513. Para a banda L o feixe restaurador foi de 1,69” $\times$ 1,28”, e PA=14° e r.m.s de 0,024mJy/beam. Já para a banda X, o feixe restaurador foi de 0,339” $\times$ 0,260”, e PA=29° e o r.m.s. foi de 0.093 mJy/beam.

A redução dos dados obtidos com o telescópio VLA [2] foi executada utilizando as rotinas correspondentes no software CASA (*Common Astronomy Software Applications*)(MCMULLIN et al., 2007). As imagens de contínuo foram geradas utilizando síntese de multi-frequências (CONWAY; CORNWELL; WILKINSON, 1990);(RAU; CORNWELL, 2011) e deconvoluídas usando o algoritmo CLEAN (SCHWAB, 1984).

Os dados de arquivo de IRAS03056+2034 em 1,425 GHz pertencem ao projeto AB660 e foram coletados em 14 de Dezembro de 1992. Os dados foram reduzidos seguindo o procedimento padrão com o software AIPS. A imagem final foi criada após calibrações realizadas com as tarefas CALIB e IMAGR, de forma iterativa.

O r.m.s. da imagem é de 0,007 mJy/beam. O feixe restaurado foi de 1.49”$\times$1.38”

[2] A redução dos dados obtidos com o VLA foi realizada por colaboradores do projeto

com PA=35° e o pico da emissão no núcleo rádio é de 11 mJy/beam.

Figura 2.1 – Espectro com a detecção do megamaser de OH descoberto em IRASF23199 por (DARLING; GIOVANELLI, 2001). Nesse espectro, a linha 1667.359 MHz é utilizada como frequência de repouso para a escala de velocidade. As setas indicam a velocidade esperada para as linhas 1667.359 MHz (esquerda) e 1665.4018 MHz (direita) com base no redshift, com barras de erro indicando a incerteza no redshift. As linhas sólidas verticais indicam a localização do máximo da função de autocorrelação e as linhas tracejadas indicam a posição esperada da linha 1665 MHz. Uma coincidência entre os dois indicadores pode representar uma detecção confiável da linha 1665 MHz. As linhas tracejadas horizontais indicam a forma (mas não a magnitude absoluta) das ”baselines” subtraídas de cada espectro calibrado. O quadro abaixo do espectro mostra o espectro dos pesos, indicando a fração de RFI-livre registrado em cada canal.

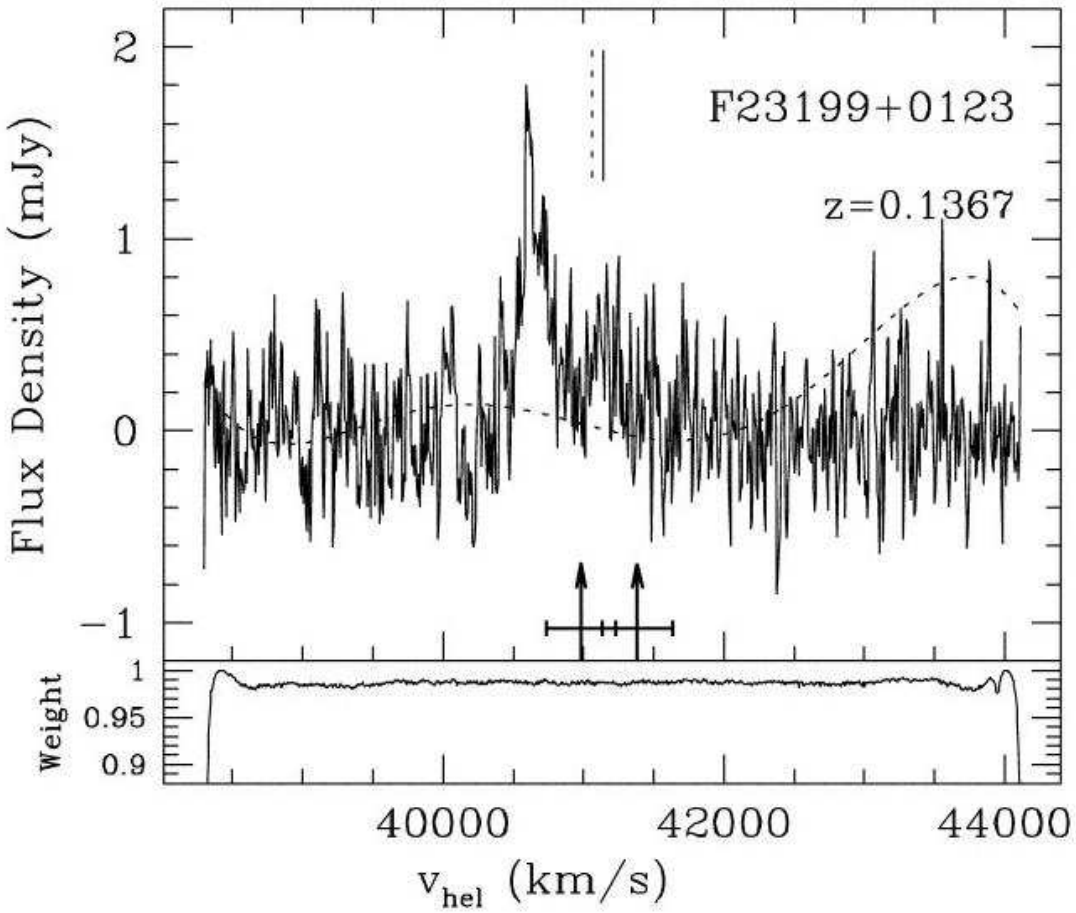

Fonte: Imagem retirada de DARLING; GIOVANELLI, 2001

Figura 2.2 – Representação esquemática de um cubo de dados

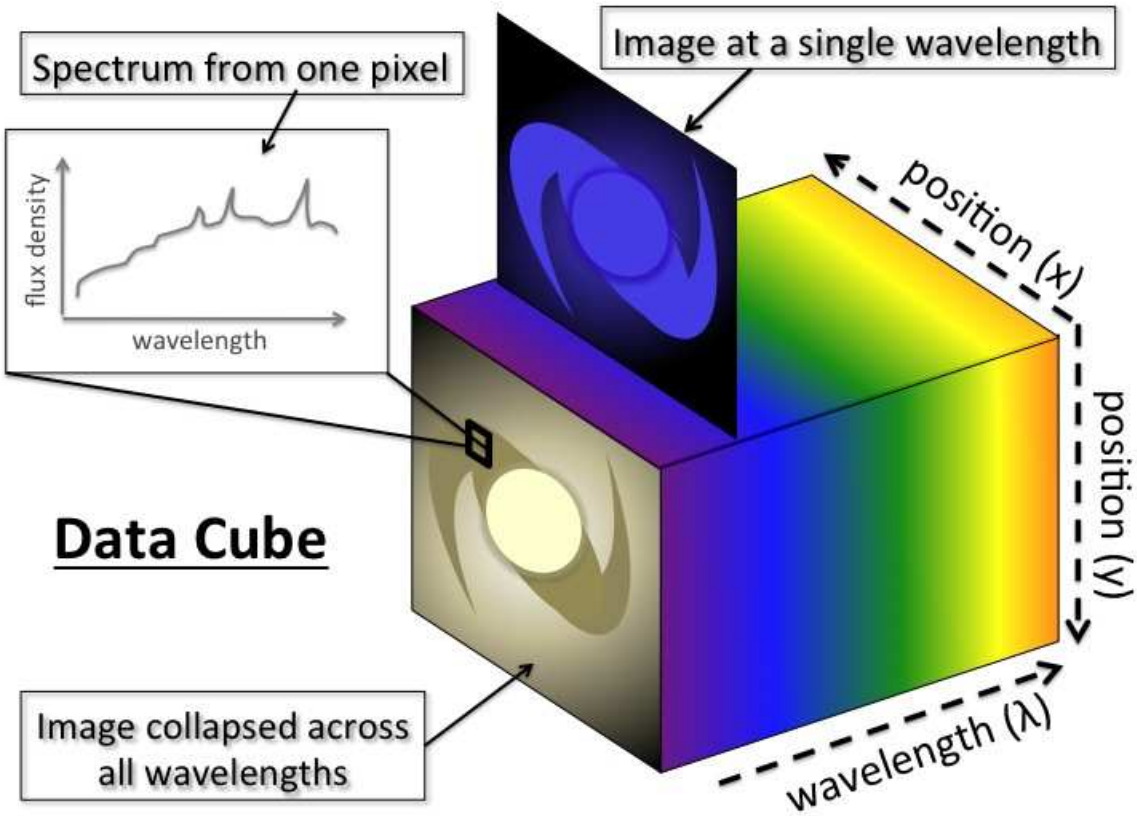

Fonte: Imagem disponível em http://eso.org/ charriso/images/datacube.jpg

3 METODOLOGIA

Com o objetivo de investigar o dinâmica e a excitação do gás nas galáxias da amostra, construímos mapas bidimensionais a partir de ajustes das linhas de emissão por curvas gaussianas. Foram construídos mapas para as distribuições de fluxos e razões de linhas, mapas de dispersão de velocidades, campos de velocidades, diagramas de diagnóstico e ajuste do modelo de disco em rotação ao campo de velocidades. Após a redução dos dados e obtenção do cubo de dados de cada galáxia, os espectros apresentaram baixa razão sinal-ruído. Dessa forma, os cubos foram filtrados utilizando um filtro de Butterworth através da rotina *bandpass-filter.pro*, em IDL, que permite a escolha frequência de corte (ν) e a ordem do filtro (n). Nós utilizamos n=5 w ν=0.15 Ny, que foram escolhidos através da comparação do cubo filtrado com o original. Para valores mais baixos de ν, apesar de ser realizada e remoção do ruído, a filtragem exclui emissão proveniente da galáxia, enquanto para valores mais altos de ν o procedimento de filtragem não é eficiente.

3.1 FILTRO DE BUTTERWORTH

Filtros seletores podem ser utilizados com os mais variados propósitos como eliminação de ruídos de determinada frequência, atenuar certas bandas de frequência em sistemas acústicos de rádios, eliminar ruídos em sons e imagens, e separar faixas de frequências para auto falantes, por exemplo. Os filtros dividem-se em duas categorias, chamadas de passa alta e passa baixa. Como o próprio nome sugere, os filtros passa alta eliminam as frequências mais baixas e os filtros de passa baixa eliminam as frequências mais altas, conferindo efeitos de suavização e realce, respectivamente. Nesse trabalho será utilizado o filtro passa baixa de Butterworth.

A utilização da Transformada de Fourier em imagens permite que a função seja analisada no domínio de frequências espaciais. A filtragem ocorre no domínio de frequências e pode ser descrita em algumas etapas. Primeiro obtém-se a transformada de Fourier $F(u, v)$ associada à imagem que será tratada. Logo em seguida, multiplica-se $F(u, v)$ por uma função filtro $H(u, v)$. Essa multiplicação tem por objetivo suprimir algumas componentes de frequência indesejadas e é realizada ponto a ponto. Por último obtém-se a transformada inversa do produto $F(u, v)H(u, v)$ para que seja possível retornar ao domínio espacial e completar o procedimento. Isso é possível pois a operação de convolução no domínio espacial é equivalente a uma multiplicação no domínio de frequências. Essa afirmação é corroborada pelo Teorema da Convolução.

O filtro de Butterworth utilizado nesse trabalho pode ser representado pela equação

$$H(u,v) = \frac{1}{1 + [D(u,v)/D_0]^{2n}}, \tag{3.1}$$

onde $D(u,v)$ é a distância entre os pontos (u,v) e (0,0) no domínio de frequências (o ponto (0,0) está no centro da imagem correspondente a Transformada de Fourier) e D_0 é a distância em relação ao ponto (0,0) a partir da qual todas as componentes de frequência serão eliminadas. Da equação acima, podemos concluir que quanto maior o valor de n (ordem do filtro) , mais abrupto será o corte. A escolha da ordem do filtro e frequência de corte foi realizada comparando-se as imagens do contínuo reconstruídas a partir dos cubos filtrados com imagens de contínuo obtidas dos cubos originais de forma a excluir somente ruído dos cubos de dados, preservando as informações referentes ao objeto.

3.2 AJUSTE DOS PERFIS

Foram realizados ajustes de curvas gaussianas aos perfis das linhas de emissão do gás para as duas galáxias, usando uma versão modificada da rotina PROFIT (emission line PROfile FITting routine (RIFFEL, 2010). A rotina fornece como saída mapas de fluxo, velocidade e dispersão de velocidades para cada linha de emissão ajustada.

Os ajustes foram realizados para as linhas Hα, [NII]$\lambda\lambda$6548, 6583, [OI]λ6300 e [OIII]λ5007. Os fluxos são obtidos pela integração da curva gaussiana e as velocidades são obtidas com base no comprimento de onda central das linhas e usando a equação para o efeito Doppler relativístico.

No caso de IRAS23199, os espectros nucleares apresentam emissão das linhas [NII]$\lambda\lambda$6548, 6583, Hα e [OI]λ6300, de forma que as linhas de [NII]$\lambda\lambda$6548,6583+Hα estão sobrepostas em uma base larga vista para Hα. O ajuste das linhas de [NII]$\lambda\lambda$6548, 6583 e Hα foi realizado simultaneamente. No interior de uma região central com 0.8", de raio os ajustes de uma gaussiana por linha de emissão não reproduziram os perfis de maneira satisfatória enquanto que para posições fora dessa região o ajuste de uma única componente por linha foi satisfatório.

Para regiões mais afastadas de 0.8" do núcleo procedemos com o ajuste de uma gaussiana por linha de emissão mantendo fixa a cinemática das linhas de [N II] para que tenham as mesmas velocidades e dispersão de velocidades, fixamos a razão [NII]λ6583/[NII]λ6548 ao seu valor teórico (3). E o contínuo foi ajustado por uma função linear.

Na região interna ao círculo de 0.8" as linhas de [NII] foram ajustadas por uma única componente e o perfil de Hα foi ajustado por uma componente estreita e mais duas componentes largas. Na figura 3.1 apresentamos um exemplo dos perfis de [NII]+Hα utilizando-se 5 curvas gaussianas, três para as componentes estreitas e duas para representar a componente larga de Hα da região nuclear de IRAS23199, a fim de melhor reproduzir o perfil

observado. Como pode ser visto nesta figura, o procedimento adotado resulta em um ajuste satisfatório para os perfis observados.

Figura 3.1 – Exemplo de ajuste de um espectro nuclear de IRAS23199. Os perfis observados estão representados em preto, o ajuste em vermelho e as componentes individuais estão representadas por linhas pontilhadas azuis.

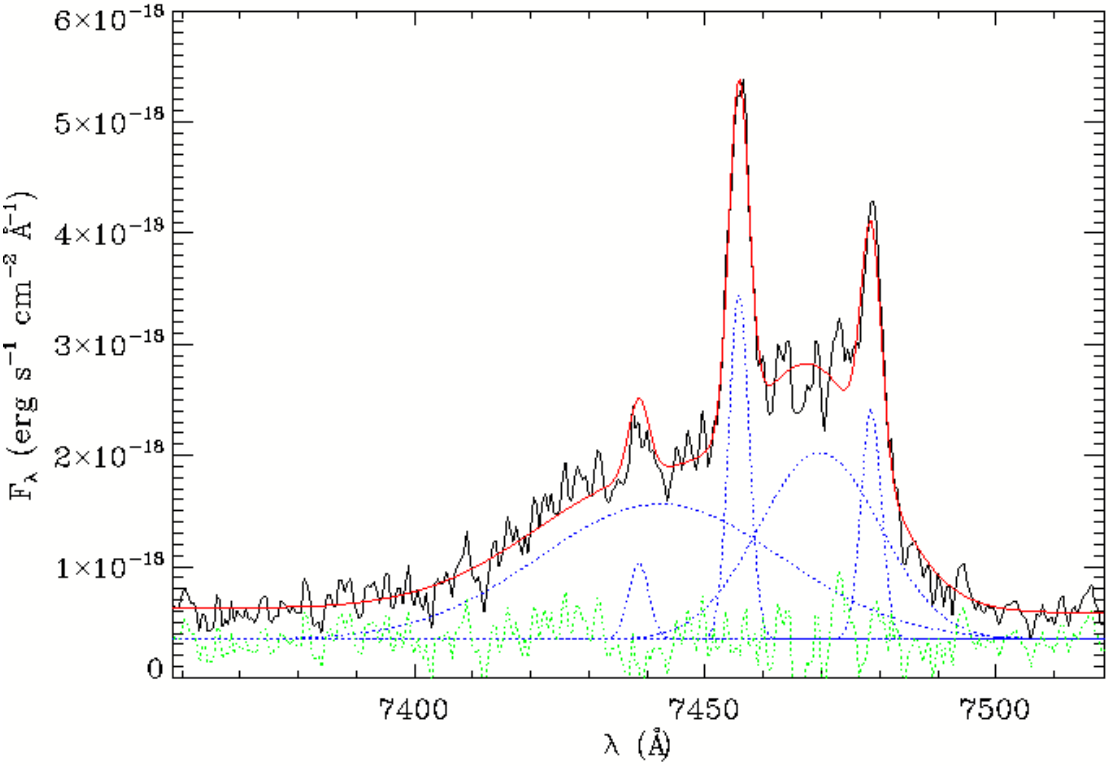

3.3 MECANISMOS DE EXCITAÇÃO DO GÁS: DIAGRAMAS DE DIAGNÓSTICO

As razões entre os fluxos das linhas de emissão são importantes indicadores quando há o interesse em determinar o mecanismo de excitação do gás emissor. Nesse sentido, foram construídos os diagramas BPT (BALDWIN; PHILLIPS; TERLEVICH, 1981) e WHAN (FERNANDES et al., 2010).

Os diagramas BPT são construídos baseando-se em quatro razões de linhas: [NII]λ6583/Hα, [OIII]/Hβ, [SII]λ6717/Hα e [OI]λ6300/Hα e permitem a distinção quanto a fonte de ionização ser devido a um AGN ou a uma região de formação estelar. Apresentam ainda a vantagem de que como são feitas razões de intensidades de linhas próximas em comprimento de onda, os efeitos de extinção não são relevantes.

A figura 3.2 mostra três dos diagramas de diagnóstico mais utilizados no óptico, obti-

dos para a galáxia IRAS03056. O eixo x apresenta as razões [NII]λ6583/Hα, [SII]λ6717/Hα e [OI]λ6300/Hα, respectivamente enquanto o eixo y apresenta a razão [OIII]λ5007/Hβ. As linhas tracejadas indicam o critério proposto por KEWLEY et al, (2001) que separa regiões ionizadas por AGN e Starburst (pontos acima da linha de Kewley correspondem a ionização devido a AGN e abaixo a Starburst) e foram derivadas a através de um estudo teórico baseado em síntese de população estelar e modelos de fotoionização. Por sua vez, (KAUFFMANN et al., 2003) propuseram a separação de ionização devido a AGN e Starburst revisando o critério proposto por (KEWLEY et al., 2001) e propondo a linha contínua presente nos três diagramas.

Figura 3.2 – Painel da esquerda: Diagrama BPT obtido para a galáxia IRAS03056 com [NII]/Hα versus [OIII]/Hβ. As linhas contínua e tracejada representam os critérios propostos por Kauffmann e Kewley, respectivamente. Painel central: diagrama de diagnóstico com [SII]λ6717/Hα versus [OIII]/Hβ. Painel da direita: Diagrama de diagnóstico com [OI]λ6300/Hα versus [OIII]/Hβ. Os asteriscos vermelhos correspondem a medidas realizadas a partir de um espectro nuclear e o ponto verde corresponde a medidas encontradas na literatura

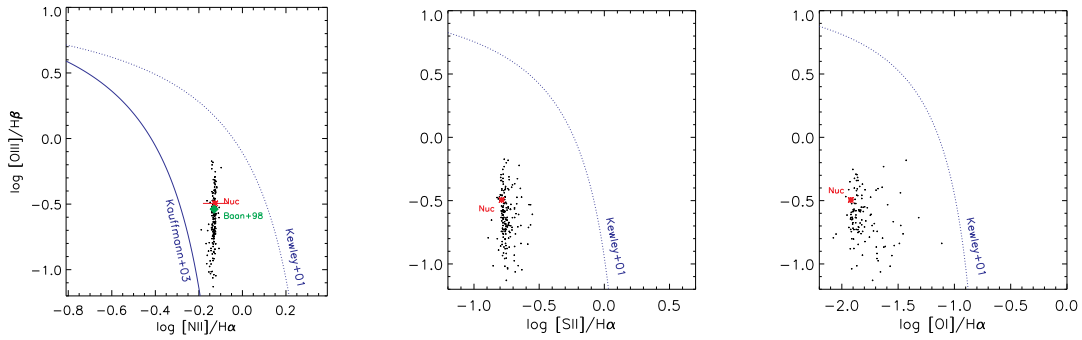

Fonte: A autora

CID FERNANDES, et al (2010) propos um diagrama de diagnóstico alternativo, que consiste em gráfico da largura equivalente de Hα (EqW) versus a razão [NII]λ6583/Hα. Enquanto para a elaboração de um diagrama BPT são necessárias no mínimo a medida do fluxo de quatro linhas de emissão, no diagrama WHAN precisamos apenas de medidas para [NII]λ6583 e Hα. O diagrama WHAN permite a separação entre Starbursts, galáxias Seyfert (sAGN) e AGNs de baixa luminosidade (wAGN). Ainda é possível realizar a separação da população de wAGNs entre aqueles que são excitados por um AGN central de galáxias ”aposentadas", onde a emissão do gás pode ser devido a sua excitação por estrelas quentes, na fase pós AGB, nas quais a largura equivalente de Hα seja menor do que 3 Å. A figura 3.3 ilustra o diagrama WHAN obtido para a galáxia IRAS23199, como exemplo.

3.4 MODELO DE ROTAÇÃO

Embora o comportamento dos campos de velocidades das galáxias estudadas não seja passível de interpretação trivial, nos fornecem indícios de rotação do gás. Com o objetivo de descrever esse comportamento analiticamente, foi proposto ajuste de um modelo de disco em rotação aos campos de velocidades. Esse modelo parte do pressuposto de que o gás move-se em órbitas circulares no plano da galáxia e está sujeito a um potencial gravitacional central.

Nesse modelo, a equação para o campo de velocidade (KRUIT; ALLEN, 1978);(BERTOLA et al., 1991) é dado por

$$V_{mod}(R,\psi) = v_s + \frac{AR\cos(\psi-\psi_0)\sin(i)\cos^p(i)}{\{R^2[\sin^2(\psi-\psi_0)+\cos^2(i)\cos^2(\psi-\psi_0)]+{c_0}^2\cos^2(i)\}^{\frac{p}{2}}} \tag{3.2}$$

onde R e ψ são as coordenadas de cada pixel no plano do céu, v_s é a velocidade sistêmica da galáxia, A é a amplitude da curva de rotação, ψ_0 é o ângulo de posição do eixo maior, i é a inclinação do disco com relação ao plano do céu (i=0 para um disco face-on), p é um parâmetro de ajuste do modelo (para p=1 a curva de rotação para raios maiores é assintóticamente plana e para p=3/2 o sistema apresenta massa finita) e c_0 é um parâmetro de concentração, definido como o raio onde a curva de rotação atinge 70 % de sua amplitude de velocidade.

O ajuste do campo de velocidades observado foi realizado através de um algoritmo de ajustes por mínimos quadrados não linear de Levenberg-Marquardt, utilizando estimativas iniciais para os parâmetros e proporcionando o ajuste dos parâmetros livres. Utilizamos a rotina *MPFITFUN* (MARKWARDT, 2009), escrita em IDL, para realizar a solução do problema de mínimos quadrados.

Como exemplo, apresenta-se no painel da direita da Figura 3.4 o resultado de um ajuste de modelo de disco em rotação utilizando a equação 3.2 ao campo de velocidade de Hα observado (mostrado no painel da esquerda).

A figura 3.4 ilustra o resultado de um ajuste de modelo de disco em rotação ao campo de velocidade de Hα observado para a galáxia 3C33 (COUTO, G. et al., 2017). Nesse caso, o modelo ajuste do modelo de disco em rotação fornece uma boa representação do campo de velocidades de Hα, mostrando que o mesmo é dominado por rotação. O ajuste forneceu os seguintes parâmatros: A= 453 km/s e orientação da linhas dos nodos de ψ_0=83°.3.

Figura 3.3 – Diagrama WHAN obtido para a galáxia IRAS23199, evidenciando as diferentes classificações propostas por CID FERNANDES et al, (2010). Cada cruz corresponde a um spaxel individual do cubo de dados, o triângulo vermelho representa o núcleo; triângulos azuis representam as regiões A, B, C e D que correspondem a supostas regiões de formação estelar.

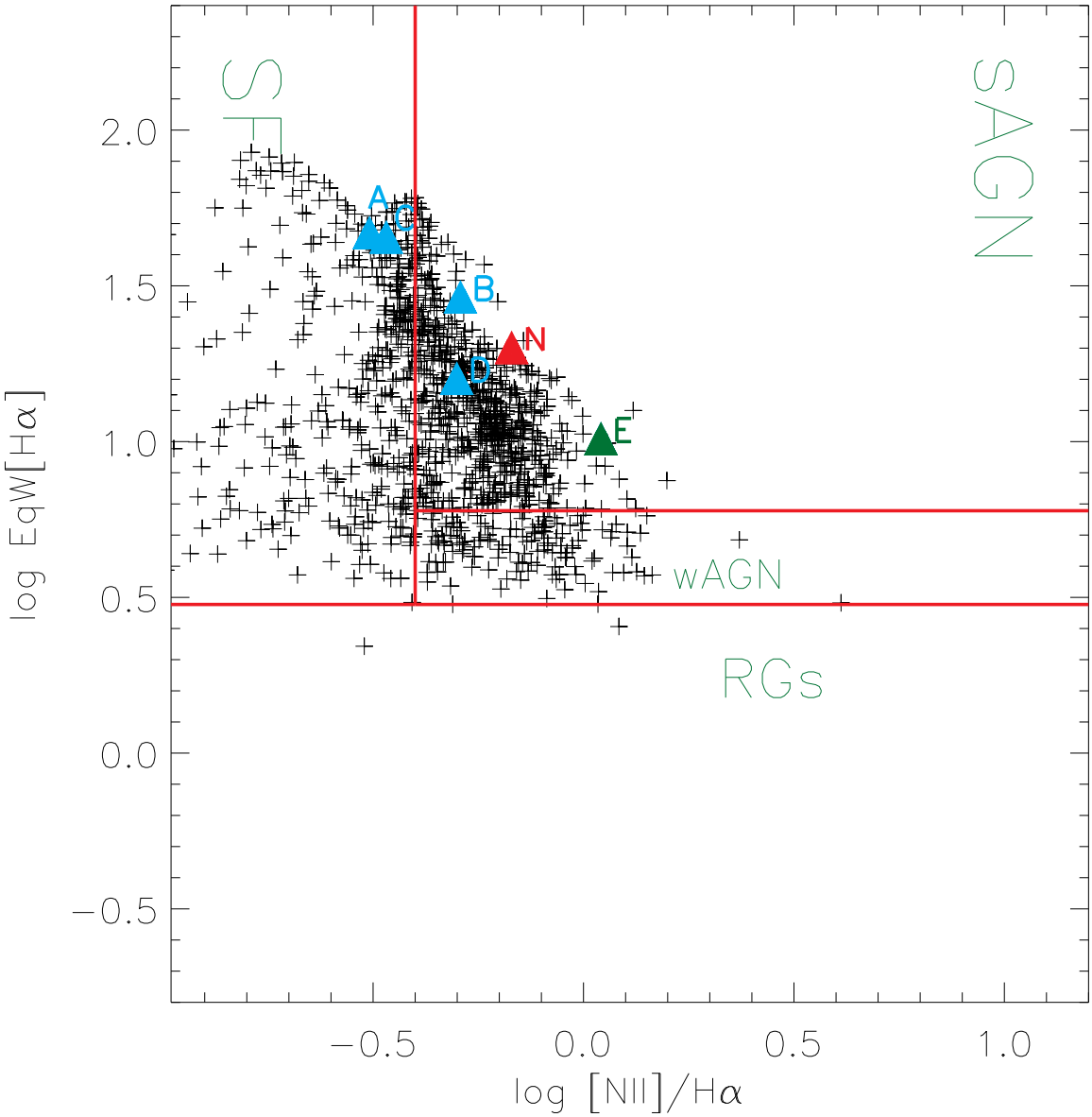

Fonte: A autora

Figura 3.4 – Exemplo de ajuste do modelo de disco em rotação para a galáxia 3C33. O campo de velocidades observado foi obtido através de ajustes de Gauss-Hermite ao perfil da linha de Hα (esquerda) e o modelo de disco em rotação está representado no painel da direita.

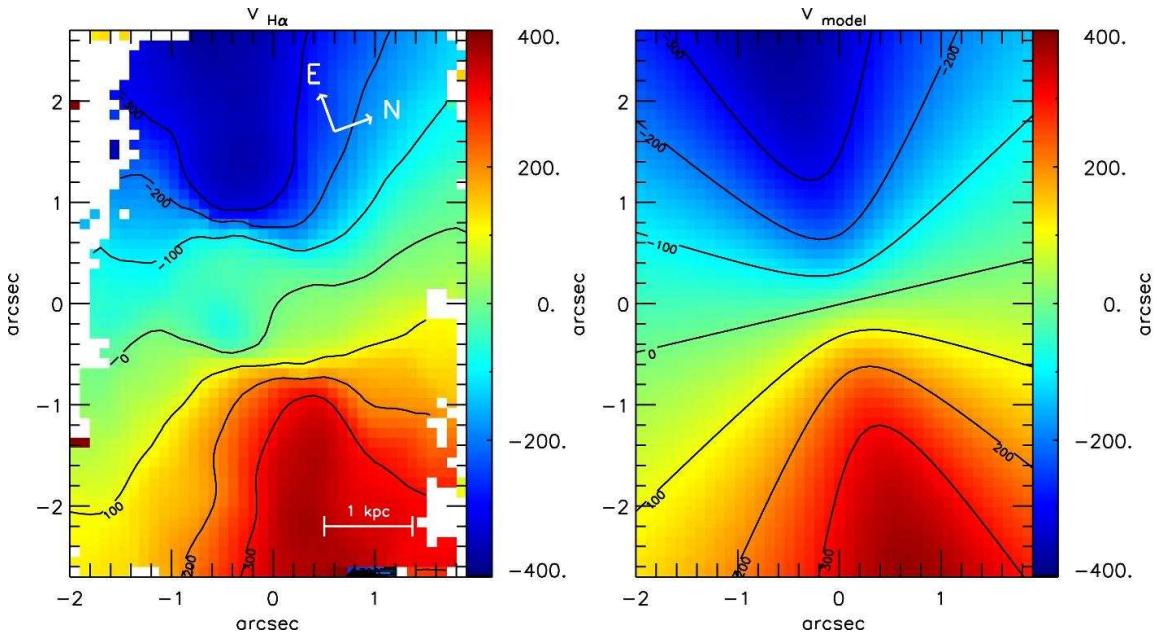

Fonte: Adaptado de (COUTO; STORCHI-BERGMANN; SCHNORR-MÜLLER, 2017)

4 RESULTADOS E DISCUSSÕES PARA IRASF23199+0123

Os resultados e discussões dessa tese encontram-se nos artigos entitulados: ”Gemini IFU, VLA, and HST observations of the OH Megamaser galaxy IRASF23199+0123: the hidden monster and its outflow” (HEKATELYNE et al., 2018a) e ”Star Formation and gas inflows in the OH Megamaser galaxy IRAS03056+2034” (HEKATELYNE et al., 2018b).

Além dos artigos referentes a esta tese, a doutoranda é coautora de mais um trabalho submetido à publicação,mostrado no apêndice desta tese. Os dados utilizados neste trabalho foram reduzidos pela doutoranda, que participou também da fase de interpretação dos resultados. Realizou a redução dos dados e ajustes das linhas de emissão para a galáxia IRAS11506-3851, que resultarão em outro artigo. Foi PI de duas propostas submetidas ao Observatório Gemini e aprovadas, resultando na observação de mais duas galáxias. Neste capítulo apresenta-se o primeiro artigo e o segundo será apresentado no capítulo 5.

[1] https://academic.oup.com/journals/pages/access_purchase/rights_and_permissions_publication_rights.

Monthly Notices of the ROYAL ASTRONOMICAL SOCIETY

MNRAS **474,** 5319–5329 (2018) doi:10.1093/mnras/stx3100
Advance Access publication 2017 December 1

Gemini IFU, VLA, and *HST* observations of the OH megamaser galaxy IRAS F23199+0123: the hidden monster and its outflow

C. Hekatelyne,[1]★ Rogemar A. Riffel,[1] Dinalva Sales,[2] Andrew Robinson,[3] Jack Gallimore,[4] Thaisa Storchi-Bergmann,[5] Preeti Kharb,[6] Christopher O'Dea[3,7] and Stefi Baum[7,8]

[1]*Departamento de Física, CCNE, Universidade Federal de Santa Maria, 97105-900 Santa Maria, RS, Brazil*
[2]*Instituto de Matemática, Estatística e Física, Universidade Federal do Rio Grande, 96203-900 Rio Grande, Brazil*
[3]*School of Physics and Astronomy, Rochester Institute of Technology, 84 Lomb Memorial Drive, Rochester, NY 14623, USA*
[4]*Department of Physics, Bucknell University, Lewisburg, PA 17837, USA*
[5]*Departamento de Astronomia, Universidade Federal do Rio Grande do Sul, 9500 Bento Gonçalves, 91501-970 Porto Alegre, Brazil*
[6]*National Centre for Radio Astrophysics, Tata Institute of Fundamental Research, S. P. Pune University Campus, Post Bag 3, Ganeshkhind, Pune 411 007, India*
[7]*Department of Physics and Astronomy, University of Manitoba, Winnipeg, MB R3T 2N2, Canada*
[8]*Center for Imaging Science, Rochester Institute of Technology, 84 Lomb Memorial Drive, Rochester, NY 14623, USA*

Accepted 2017 November 20. Received 2017 November 20; in original form 2017 August 25

ABSTRACT

We present Gemini Multi-Object Spectrograph (GMOS) Integral field Unit (IFU), Very Large Array (VLA), and *Hubble Space Telescope* (*HST*) observations of the OH megamaser (OHM) galaxy IRAS F23199+0123. Our observations show that this system is an interacting pair, with two OHM sources associated with the eastern (IRAS 23199E) member. The two members of the pair present somewhat extended radio emission at 3 and 20 cm, with flux peaks at each nucleus. The GMOS-IFU observations cover the inner ∼6 kpc of IRAS 23199E at a spatial resolution of 2.3 kpc. The GMOS-IFU flux distributions in Hα and [N II] λ6583 are similar to that of an *HST* [N II]+Hα narrow-band image, being more extended along the north-east–south-west direction, as also observed in the continuum *HST F814W* image. The GMOS-IFU Hα flux map of IRAS 23199E shows three extranuclear knots attributed to star-forming complexes. We have discovered a Seyfert 1 nucleus in this galaxy, as its nuclear spectrum shows an unresolved broad (full width at half-maximum ≈2170 km s^{-1}) double-peaked Hα component, from which we derive a black hole mass of $M_{\rm BH} = 3.8^{+0.3}_{-0.2} \times 10^6$ M$_\odot$. The gas kinematics shows low velocity dispersions (σ) and low [N II]/Hα ratios for the star-forming complexes and higher σ and [N II]/Hα surrounding the radio emission region, supporting interaction between the radio plasma and ambient gas. The two OH masers detected in IRAS F23199E are observed in the vicinity of these enhanced σ regions, supporting their association with the active nucleus and its interaction with the surrounding gas. The gas velocity field can be partially reproduced by rotation in a disc, with residuals along the north–south direction being tentatively attributed to emission from the front walls of a bipolar outflow.

Key words: galaxies: individual: IRAS F23199+0123 – galaxies: ISM – galaxies: kinematics and dynamics.

1 INTRODUCTION

(Ultra)luminous infrared galaxies ([U]LIRGs) are among the most luminous objects in the Universe showing infrared (IR) luminosities of $L_{\rm IR} > 10^{12}$ L$_\odot$. These objects are believed to represent a key stage in the evolution process of galaxies in which tidal torques associated with mergers drive gas into the galaxy core, leading to the feeding/triggering of nuclear starbursts or the fuelling of embedded active galactic nuclei (AGN; e.g. Sales et al. 2015).

These merging systems provide a conducive environment for OH maser emission and approximately 20 per cent of [U]LIRGs contain extremely luminous OH masers, emitting primarily in the 1667 and 1665 MHz lines with luminosities 10^{2-4} L$_\odot$

★ E-mail: hekatelyne.carpes@gmail.com

(Darling & Giovanelli 2002; Lo 2005). The OH megamasers (OHMs) are commonly associated with merging systems, but the environment that produces this phenomenon is still not completely understood. Many OHM hosts present a composite spectrum, showing both AGN and starburst features. A possible explanation for these features is that they originate in a central AGN, contaminated by emission of circumnuclear star-forming regions, as the sampling of the observations usually corresponds to more than 1 kpc at the galaxies. Alternatively, the OHM galaxies could represent a transition stage between a starburst and the eruption of an AGN, as suggested by Darling & Giovanelli (2006).

Considering the above scenario, it becomes relevant to investigate the nature of the gas ionization source of OHM galaxies. In this paper, we present Gemini Multi-Object Spectrograph (GMOS) Integral Field Unit (IFU) observations, Very Large Array (VLA) continuum data, and *Hubble Space Telescope* (*HST*) narrow- and broad-band images of the galaxy IRAS F23199+0123, which is an interacting pair of ULIRGs that presents OHM emission. This galaxy is part of a sample of 15 OHM galaxies, for which we have already *HST* images from a project that has the overall goal of relating the merger state and OH maser properties to AGN and starburst nuclear activity. We have selected targets for IFU observations from the 15 galaxies observed with *HST*, on the basis of the morphology revealed by the images. This paper is a pilot study based on multiwavelength observations, aimed to study the gas kinematics and excitation of one OHM galaxy and that we hope to extend to the whole sample.

IRAS F23199+0123 has a redshift $z = 0.13569$ (Darling & Giovanelli 2006), corresponding to a distance of 558 Mpc for which 1 arcsec corresponds to 2.7 kpc at the galaxy, assuming a Hubble constant of $H_0 = 73\,\mathrm{km\,s^{-1}\,Mpc^{-1}}$. Its OH maser emission was first detected in the Arecibo survey that observed 52 objects with $0.1 < z < 0.26$ (Darling & Giovanelli 2001). Darling & Giovanelli (2006) used spectroscopic data obtained with the Palomar 5-m telescope with the Double Spectrograph in order to perform an optical spectroscopic study of the properties of the sample of the Arecibo survey and identified the nuclear emission of IRAS F23199+0123 as being due to a Seyfert 2 nucleus, based on emission-line ratios.

Our GMOS-IFU data comprise observations of the central region of the eastern galaxy of the IRAS F23199+0123 pair and our aim is to map the distribution and kinematics of the optical line emitting gas and investigate the excitation mechanism of the nuclear emission. This is the first time that OHM galaxies have been observed with an Integral Field Spectrograph, allowing a two-dimensional look at the gas excitation and kinematics in detail. This paper is organized as follows. Section 2 describes the observations and data reduction procedure, and Section 3 explains the emission-line fitting process and present maps for the emission-line flux distributions and kinematics, as well as the *HST* and VLA radio continuum images, while in Section 4 the results are discussed. Finally, the conclusions of this work are presented in Section 5.

2 OBSERVATIONS AND DATA REDUCTION

2.1 VLA radio continuum data

We observed IRAS F23199+0123 with the Karl G. Jansky Very Large Array (VLA) on 2014 April 20. The observations included *X*-band (8–10 GHz) continuum, *L*-band (1–2 GHz) continuum, and *L*-band spectral line observations of the redshifted OH (1665/1667 MHz) maser lines. The *L*-band and *X*-band observations comprised, respectively, three and one 10-min scans, alternating with 3-min scans of the phase calibrator, J2320+0513. We observed the source 3C 48 in both *X* band and *L* band for flux and bandpass calibration.

The VLA pipeline in CASA (McMullin et al. 2007) was used for data reduction. This includes initial data flagging and phase, flux, and bandpass calibrations. The continuum images were generated using multifrequency synthesis (e.g. Conway, Cornwell & Wilkinson 1990; Rau & Cornwell 2011) with natural weighting and deconvolved using the Cotton–Schwab variant of the CLEAN algorithm (Schwab 1984). Imaging included simultaneous deconvolution of neighbouring radio sources within the primary beam. We applied three rounds of phase-only self-calibration based on CLEAN models for the radio continuum (self-calibration is reviewed by Pearson & Readhead 1984). For the *L*-band continuum image, the restoring beam is $1.69 \times 1.28\,\mathrm{arcsec^2}$, position angle (PA) = 14°, and the background rms is $0.024\,\mathrm{mJy\,beam^{-1}}$. The restoring beam of the *X*-band continuum image is $0.339 \times 0.260\,\mathrm{arcsec^2}$, PA = 29°, and the background rms is $0.0093\,\mathrm{mJy\,beam^{-1}}$. The radio continuum images are presented in Fig. 2.

The spectral line visibilities were continuum subtracted in two steps. First, we produced CLEAN continuum models based on line-free channels, and the CLEAN models were subtracted from the observed visibilities. Second, we removed any residual continuum using the CASA task UVCONTSUB; the continuum was determined by averaging visibility spectra over line-free channels. The continuum-subtracted, spectral line data cube was produced using standard Fourier inversion and CLEAN deconvolution. The expected line width of the 1667 MHz feature is 0.68 MHz (Darling & Giovanelli 2001); therefore, to improve the signal-to-noise ratio, we binned the spectral line data to 0.23 MHz channels (roughly 1/3 line width). The restoring beam of the OH spectral line cube is $1.77 \times 1.36\,\mathrm{arcsec^2}$, PA 14°, and the typical background rms for a single 0.23 MHz channel is $0.44\,\mathrm{mJy\,beam^{-1}}$.

2.2 *Hubble Space Telescope* data

HST images of IRAS F23199+0123 were acquired using the Advanced Camera for Surveys (ACS) with the broad-band filter *F814W*, the narrow-band filter *FR656N*, and medium-band *FR914M* filter as part of a snapshot survey program to observe a sample of OHMGs (Program id 11604; PI: D. J. Axon). The total integration time was 600 s in the broad-band (*I*) *F814W* filter, 200 s in the medium-band filter, and 600 s in the narrow-band Hα *FR656N* filter. The bandpass of the *FR656N* narrow-band filter includes both Hα and [N II] λ6548, 6583 emission lines. We have processed the final images in order to remove cosmic rays using IRAF task LACOS_IM (van Dokkum 2001). The continuum-free Hα+[N II] image of IRAS F23199+0123 was constructed according to the following the steps: (i) the count rates of a few stars were obtained in both the medium-band (*FR914M*) and narrow-band (*FR656N*) ramp filter images; (ii) from the count rate ratios the mean scaling factor was computed and applied to the medium-band *FR914M* image; (iii) the scaled *FR914M* image was then subtracted from the narrow-band *FR656N* image. We next visually inspected our continuum subtracted Hα+[N II] image to assure that the residual fluxes of foreground stars were negligible within the uncertainties. This procedure results in typical flux uncertainties of 5–10 per cent (see Hoopes, Walterbos & Rand 1999; Rossa & Dettmar 2000, 2003).

The *HST* images (see Fig. 4) show for the first time that IRAS F23199+0123 is indeed an interacting pair and we have obtained IFS of the eastern member of the par (hereafter IRAS 23199E).

2.3 GMOS IFU data

IRAS 23199E was observed using the GMOS (Hook et al. 2004) IFU (Allington-Smith et al. 2002) as part of the program GS-2013B-Q-86 (PI: D. Sales). Only the eastern nucleus was observed, as it presents a steep continuum flux distribution and with bright guide stars available in the GMOS patrol field. The major axis of the IFU was oriented along PA = 215°, approximately along the major axis of the galaxy. The total on source exposure time was 4800 s divided into four individual exposures of 1200 s each. The observations were performed on 2013 August 29 using the B600 grating with the IFU in the one slit mode, in combination with the *GG455* filter. This set-up resulted in an angular coverage of 5.0 × 3.5 arcsec^2, covering the spectral region from 450 to 750 nm at a spectral resolution of 1.7 Å, as obtained from the measurement of the full width at half-maximum (FWHM) of typical emission lines of the Ar lamp spectrum used for the wavelength calibration.

The data reduction process was performed using routines of the GEMINI package in the Image Reduction and Analysis Facility (IRAF; Tody 1986, 1993) software and followed the standard procedure of spectroscopic data reduction (Lena 2014). First, we subtracted the bias level from each image, performed flat-fielding and trimming. Then, we applied wavelength calibration to the data using the spectra of arc lamps as references and subtracted the sky emission. Finally, we performed flux calibration using a sensitivity function obtained from the spectrum of the H600 photometric standard star observed during the same night of the object observations.

Finally, data cubes for each individual exposures were created at an angular sampling of 0.1 × 0.1 arcsec^2, which were then median combined using the IRAF GEMCOMBINE task to obtain the final data cube for the object. The peak of the continuum emission was used as a reference during the mosaicking of the individual data cubes and we used the AVSIGCLIP algorithm for bad pixel/cosmic ray removal. We estimated the angular resolution as 0.85 arcsec from the measurement of the FWHM of the flux distribution of field stars present in the acquisition image of the galaxy. This angular resolution corresponds to ∼2.3 kpc at the galaxy for its adopted distance (d = 558 Mpc).

In order to remove noise from the final data cube, we performed a spatial filtering using a Butterworth bandpass filter (Gonzalez & Woods 2002; Menezes, Steiner & Ricci 2014; Menezes et al. 2015) via the IDL routine BANDPASS_FILTER.PRO,[1] which allows the choice of the cut-off frequency (ν) and the order of the filter n. A low value of n (e.g. 1) is close to a Gaussian filter, while a high value (e.g. 10) corresponds to an ideal filter. We used $n = 5$ and $\nu = 0.15$ Ny, chosen by comparing the filtered cube with the original one. For lower values of ν, besides the removal of spatial noise, the filter excludes also emission from the galaxy, while for larger values of ν the filtering procedure is not efficient. The filtering process does not change the angular resolution of the data and all measurements presented in the forthcoming sections were done using the filtered cube.

3 RESULTS

3.1 Hα+[N II] GMOS-IFU spectra

In order to map line fluxes, line-of-sight velocity (V_{LOS}), and velocity dispersion (σ) of the emitting gas, we fitted the emission-line profiles of Hα and [N II]λλ6548, 6583 with Gaussian curves. The fitting was performed using modified versions of the line-PROfile FITting (PROFIT) routine (Riffel 2010), which provides as outputs the emission-line flux, the centroid velocity, the velocity dispersion and their corresponding uncertainties. Besides the [N II]+Hα emission lines, the nuclear spectrum includes also the [O I] λ6300.3 emission line, which shows a similar profile to that of the [N II] and Hα narrow components, being well reproduced by a single Gaussian curve.

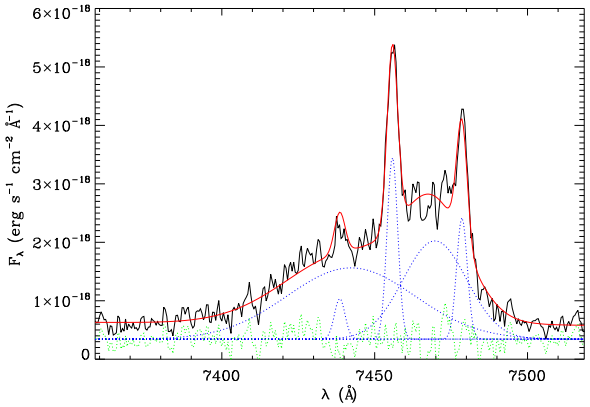

Figure 1. Fit of the nuclear spectrum (within 0.8 arcsec from the nucleus) of IRAS 23199E comprising the Hα+[N II] complex. The observed profile is shown in black, while the blue dotted lines represent the broad and narrow components. The red line is the result of the fit, and the green dotted line shows the residual of the fit plus an arbitrary constant.

The fitting process for the Hα and [N II] λλ6548, 6583 emission lines was performed simultaneously. We noticed that in the inner 0.8 arcsec radius (corresponding to about two resolution elements), the fitting of a single Gaussian component for each emission line does not reproduce the observed profile, while at larger distances from the nucleus a single component provides a good fit. Thus, at locations farther then 0.8 arcsec from the nucleus (defined as the location of the peak of the continuum emission) we fitted the Hα+[N II] complex using one Gaussian per line, adopting the following constraints: (i) we kept tied the kinematics of the [N II] lines, such that the two lines have the same velocity and velocity dispersion, and (ii) fixed the [N II] λ6583/[N II] λ6548 intensity ratio to its theoretical value (3). The underlying continuum was fitted by a linear function.

Within 0.8 arcsec from the nucleus, we tested two possibilities for the fit to the Hα+[N II] complex. In the first, we fitted the line profiles using four Gaussian curves, in order to include a broad component to represent Hα. The resulting fit does not reproduce the observed profiles adequately. In the second fit, the [N II] lines were fitted by a single Gaussian component, while the Hα profile was fitted by the same narrow component plus two broad components. This procedure resulted in a better fit to the profiles. As the presence of two broad components is restricted to the nucleus and the corresponding emission is not resolved, we propose that they actually represent a single double-peaked line originating in the broad-line region (BLR). Such double-peaked components are not uncommon in AGN (e.g. Storchi-Bergmann et al. 2017).

In Fig. 1 we show the resulting fit of the nuclear spectrum, where the observed profiles are shown in black, the best-fitting model in red and the individual components as dotted blue lines. As the emission of the BLR is not resolved, the width and central wavelength of each broad component and their relative fluxes were kept fixed for

[1] The routine is available at: https://www.harrisgeospatial.com/docs/bandpass-filter.html

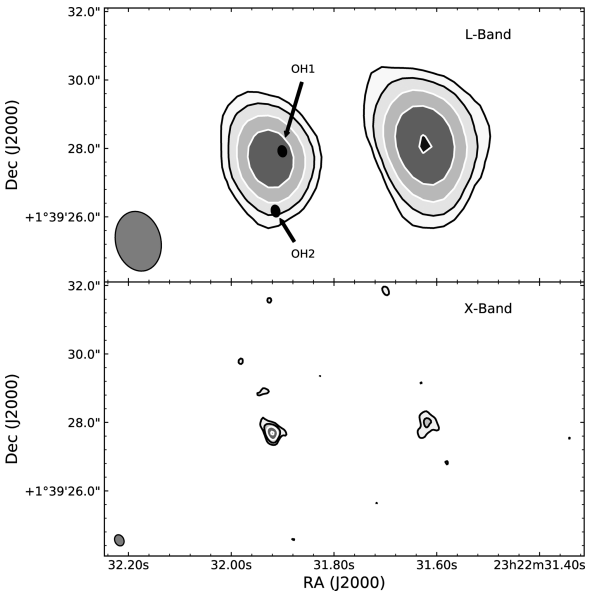

Figure 2. Top panel: VLA *L*-band (1.6 GHz) continuum image of IRAS F23199+0123, shown as filled contours. The contours are (black) 0.071 (3σ), 0.15, (white) 0.32, 0.69, and 1.5 mJy beam^{-1}. The OH1 and OH2 labels identify the locations where the OH maser sources were detected (see Fig. 3). Bottom panel: VLA *X*-band (8 GHz) continuum image of IRAS F23199+0123, shown as filled contours. The contours are (black) 0.0278 (3σ), 0.0647, (white) 0.150, and 0.349 mJy beam^{-1}.

all spaxels, while their amplitudes were allowed to vary to enable for smearing by the seeing. The values of the centroid velocities and velocity dispersions were obtained by fitting an integrated spectrum of the inner 0.8 arcsec. The centroid velocities relative to the systemic velocity are -416 and 668 km s^{-1} for the blueshifted and redshifted components, respectively. The corresponding velocity dispersions are $\sigma = 955$ km s^{-1} for the blue component and $\sigma = 475$ km s^{-1} for the red component. In the hypothesis described above that these two components represent a single double-peaked line, this line profile has a FWHM of 2170 km s^{-1}. The systemic velocity adopted in this paper is $v_s = 37\,947 \pm 2$ km s^{-1} (corrected for the heliocentric rest frame), as derived by the modelling of the gas velocity field as discussed in Section 4.3.

3.2 OH maser spectra

Fig. 3 shows the VLA OH spectra extracted at the positions of the eastern (IRAS 23199E) and western nuclei. OH masers are detected only towards the eastern nucleus. Two line features appear in the spectrum, which we label 'OH1', detected at 5.4σ significance, and 'OH2', a 4.1σ detection. To within the measurement uncertainties, OH1 matches the central frequency and peak flux density of the maser feature detected by Darling & Giovanelli (2001). To our knowledge, OH2 has never been detected before; OH2 falls outside the bandpass of the Darling & Giovanelli (2001) Arecibo observations. The position of OH1 and OH2 defections is identified in the top panel of Fig. 2.

Fig. 3 shows that OH1 appears to identify with the 1665 MHz line at the redshift of the eastern nucleus. Assuming OH1 is indeed the 1665 MHz line, its centroid velocity would be $v = +85 \pm 28$ km s^{-1} relative to systemic in the rest frame of the eastern nucleus. OH2

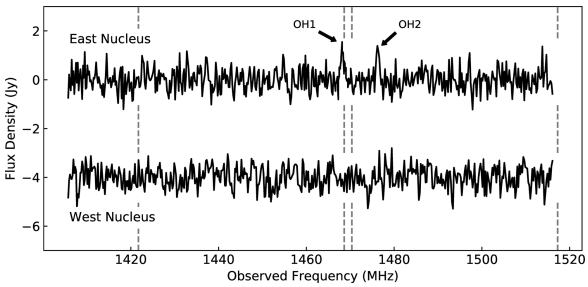

Figure 3. VLA OH maser spectra of the eastern (top) and western (bottom, offset by -4 mJy) nuclei. The vertical, dashed grey lines mark the expected, redshifted frequencies for the 1612, 1665, 1667, and 1712 MHz maser features. Two spectral features are detected at the position of the eastern nucleus, marked OH1 and OH2. OH1 was originally detected by Darling & Giovanelli (2001); OH2 is a new detection.

is however significantly offset from the expected heliocentric frequencies of possible emission lines. It may identify either with 1665 MHz line at $v = -1557 \pm 22$ km s^{-1} or the 1667 MHz line at $v = -436 \pm 29$ km s^{-1} relative to systemic.

3.3 *HST* images

Fig. 4 presents the *HST* broad-band continuum *F814W* image (top panel) and the narrow-band Hα+[NII] image (bottom panel) of the inner 20×20 arcsec^2 of IRAS F23199+0123, which reveal that this system is an interacting pair. The images in the left-hand panels show both galaxies of the pair, while the right-hand panels show a zoomed in view of IRAS 23188E within the same field of view of the GMOS IFU observations. The green box in the left-hand panels corresponds to the field of view of our GMOS data. The *HST* images were rotated to the same orientation of the GMOS data.

The *F814W* continuum image of IRAS 23199E presents the highest intensity levels in an elongated structure at PA $\approx 45^\circ$ suggesting that the galaxy is highly inclined. The western galaxy of the pair shows a less elongated flux distribution, suggesting a more face-on orientation, although the flux distribution towards the centre is not uniform, but presents a complex structure. The *F814W* image also reveals a structure that resembles a spiral arm to the north that seems to connect the two galaxies, which may be a tidal tail connecting the two galaxies. The linear distance between the galaxy nuclei, projected in the plane of the sky is 24 kpc, assuming a distance to the galaxy of 558 Mpc. This is a lower limit as we do not know the orientation of the plane containing both galaxies or their nuclei relative to the plane of the sky.

The bottom left-hand panel of Fig. 4 shows the continuum-free *HST* Hα+[N II] narrow-band image of the two galaxies. The bottom right-hand panel shows a zoom of the region observed with GMOS-IFU, covering the central part of IRAS 23199E. The Hα+[N II] flux distribution is similar to that of the continuum, and suggests the presence of two tidal tails, one to the north-east and another to the south-west of the nucleus.

3.4 Emission-line flux distributions

The top panels of Fig. 5 present the flux distributions in the narrow components of Hα (left) and [N II] λ6583 (right) emission lines. The colour bars show the flux in logarithmic units of erg s^{-1} cm^2, and the grey regions represent masked locations where the uncertainty

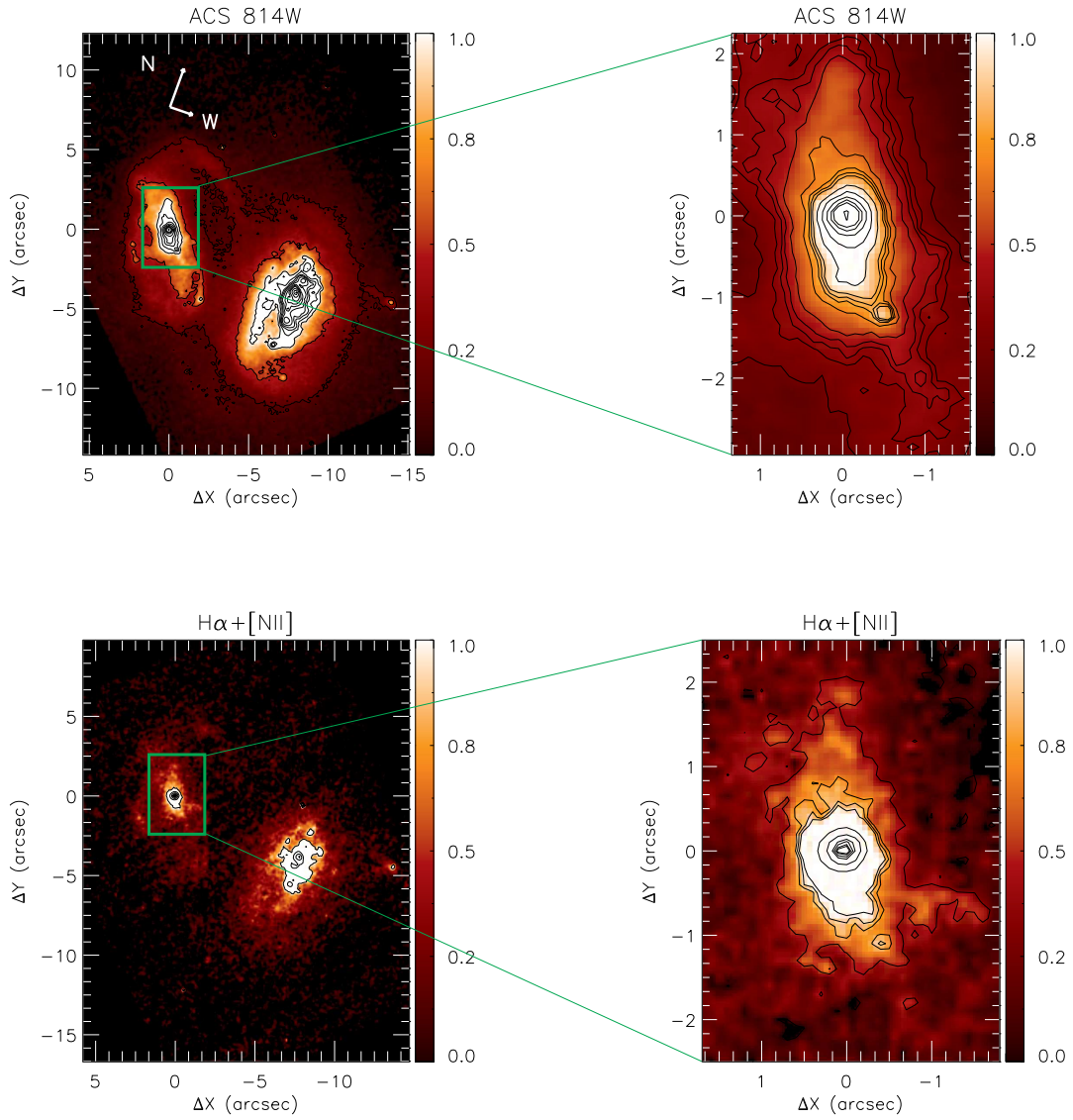

Figure 4. Top panels: left – large-scale image (ACS/*HST F814W* – *i* band); right – zoom of the region observed with GMOS. Bottom panels: left – *HST* large-scale continuum-free Hα+[N II] image; right – zoom at the region observed with GMOS IFU. The green boxes show the GMOS IFU field of view (3.5×5.5 arcsec^2) and the colour bars show the fluxes in arbitrary units.

in the flux is larger than 30 per cent. The central cross marks the location of the nucleus, defined as the position of the peak of the flux distribution of the broad Hα component and is labelled with the letter N in Fig. 5. The two lines show similar flux distributions, with the emission within the inner ∼1 arcsec being elongated in the north-east–south-west direction. At least three extranuclear knots of emission, labelled A, B, and C in Fig. 5, are observed in the Hα flux map, at (x, y) angular distances relative to the nucleus of (−0.6, −2.2 arcsec), (−1.0, 1.8 arcsec), and (1.0, −0.6 arcsec). We note that these knots are not observed in the *HST* [N II]+Hα image.

3.5 Gas velocity fields and velocity dispersion maps

The central panels of Fig. 5 present the line-of-sight velocity ($V_{\rm LOS}$) fields for the Hα (left) and [N II] λ6583 (right) emission lines. White regions were masked following the same criteria used for the flux maps, described above. The systemic velocity of $V_{\rm s} = 37\,947$ km s^{-1} was subtracted from the observed velocities, as derived from the modelling of the Hα velocity field with a rotating disc model (see Section 4.3).

The velocity fields derived from Hα and [N II] emission lines are similar, presenting redshifts to the west and blueshifts to the east of the nucleus with velocities reaching up to 200 km s^{-1}. The zero velocity line presents an S-shape and values close to the systemic velocity are observed at ∼2 arcsec to the north of the nucleus.

The bottom panels of Fig. 5 show the velocity dispersion (σ) maps for Hα (left) and [N II] λ6583 (right), corrected for the instrumental broadening. These maps show values ranging from ∼40 to 150 km s^{-1}, with the highest values observed cospatially with the S-shaped zero velocity curve of the $V_{\rm LOS}$ maps (central panels). In

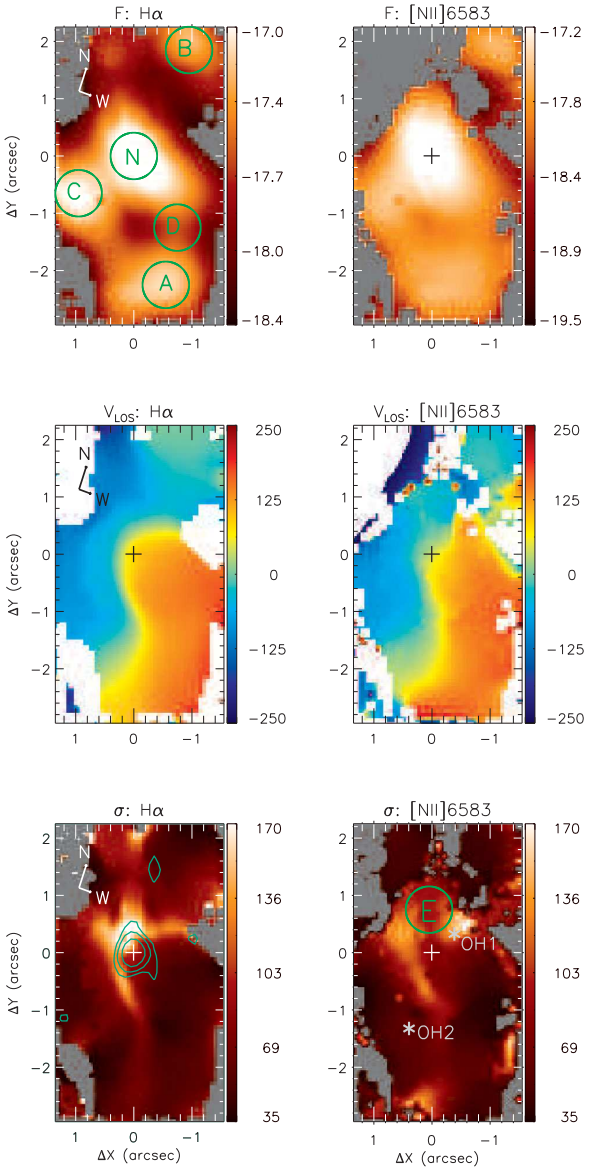

Figure 5. Top panels: flux maps in the Hα (left) and [N II] λ6583 (right) emission lines. The colour bars show the fluxes in logarithmic units of erg s^{-1} cm^{-2}. Central panels: line-of-sight velocity fields for the Hα (left) and [N II] (right) emitting gas. The colour bars show the velocities in units of km s^{-1}, after the subtraction of the systemic velocity of the galaxy. Bottom panels: velocity dispersion maps for the Hα (left) and [N II] (right) emission lines, corrected for the instrumental broadening. The colour bars show the σ values in units of km s^{-1}. The central cross in all panels marks the position of the nucleus and grey regions in the flux and σ maps and white regions in the V_{LOS} maps represent masked locations, where the signal-to-noise ratio was not high enough to obtain reliable fits to the emission-line profiles or locations with no line detection. The green contours in the velocity dispersion map of Hα line are from the 3-cm radio image. The grey asterisks labelled as OH1 and OH2 mark the locations where the maser emission has been detected.

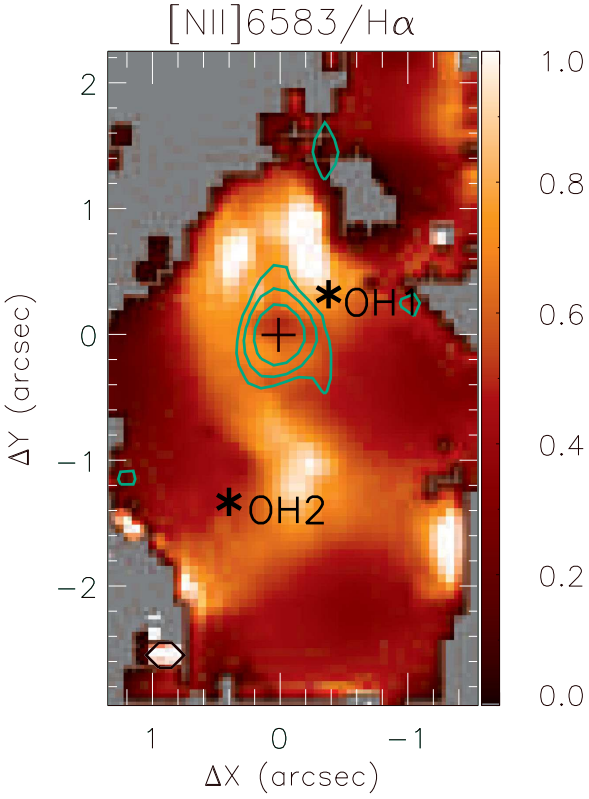

Figure 6. [N II]/Hα flux ratio map for IRAS 23199E. Grey regions correspond to masked locations where no reliable measurements are available. The green contours in the map are from the 3-cm radio image. The black asterisks labelled as OH1 and OH2 mark the position of the maser emission.

addition, some high σ values are seen for Hα at 1.5 arcsec northeast of the nucleus, where the velocity fields present the highest blueshifts. The smallest values of σ are cospatial with the extranuclear knots of emission observed in the emission-line flux distributions in the top panels of Fig. 5.

4 DISCUSSION

In this work, we present for the first time high-quality *HST* images of IRAS F23199+0123. These images allowed us to identify that this system is indeed composed by two members and discern tidal structures. Thus, this is the first time that this system has been established to be an interacting galaxy pair.

4.1 Gas excitation and diagnostic diagrams

The [N II] λ6583/Hα flux ratio can be used to map the gas excitation (e.g. Baldwin, Phillips & Terlevich 1981; Cid Fernandes et al. 2010), with values [N II] λ6583/Hα $\leq$ 1 corresponding to gas ionized by young stars, while larger values correspond to gas excited by a central AGN or shocks (e.g. Storchi-Bergmann et al. 2007; Cid Fernandes et al. 2011).

In Fig. 6 we present the [N II] λ6583/Hα ratio map for IRAS 23199E. Grey regions correspond to locations masked due to poor fits. The map shows values ranging from ∼0.2 to 1, with the highest values observed approximately coincident with the region with the highest σ values (bottom panels of Fig. 5), while the

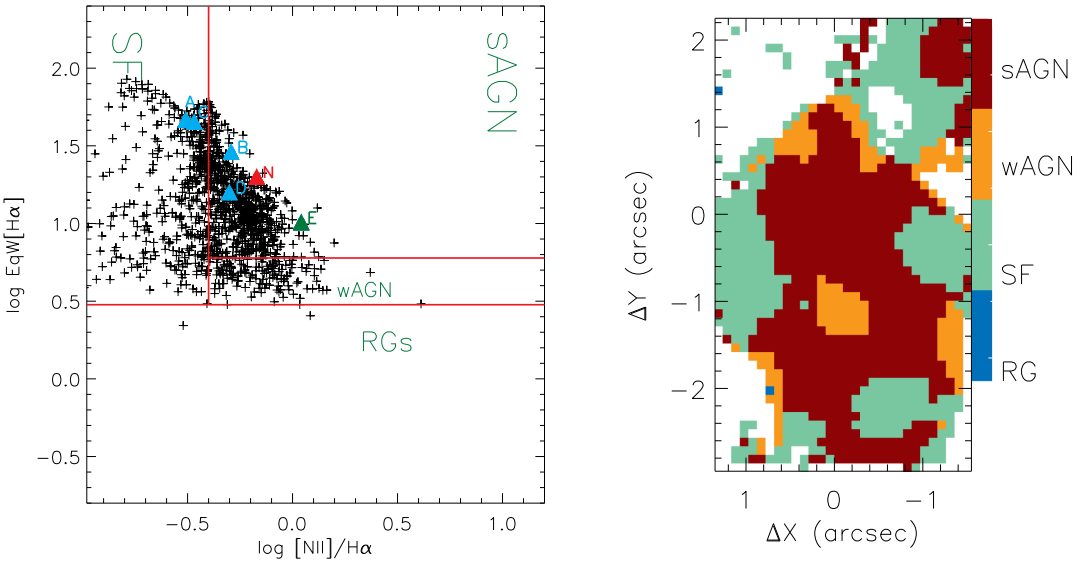

Figure 7. Left: the WHAN diagram for IRAS 23199E showing the different excitation regions (Cid Fernandes et al. 2010). Each cross corresponds to an individual spaxel of the IFU data cube; the red triangle represents the nucleus; blue triangles are for regions A, B, C, and D identified in the Hα flux map of Fig. 5; and the green triangle corresponds to the region E identified in the [N II] σ map of Fig. 5. Right: excitation map identifying the regions within the field of view corresponding to different excitation mechanisms: strong AGN (sAGN), weak AGN (wAGN), star-forming (SF), and retired galaxy (RG).

lowest values are observed in the knots of enhanced Hα emission (top left-hand panel of Fig. 5). We interpret these latter locations as complexes of star-forming regions.

The fact that the locations with the highest [N II] λ6583/Hα ratios are cospatial with the highest σ values suggests that shocks contribute to the gas excitation. We have extracted a spectrum within a circular aperture of 0.4 arcsec radius in one of these locations, labelled E in Fig. 5. We have measured the line ratios and equivalent width of Hα from this spectrum, to plot this region in the diagnostic diagram WHAN (Cid Fernandes et al. 2010). This diagram has been proposed as an alternative to the BPT diagrams of Baldwin et al. (1981), and is a plot of the Hα equivalent width against the [N II] λ6583/Hα flux ratio. While BPT diagrams need four emission lines to separate the regions ionized by AGN or starburst, the WHAN diagram requires just Hα and [N II]. The WHAN diagram enables a separation between starbusts, Seyfert galaxies (sAGN) and low-luminosity AGNs (wAGN). It is also possible to separate wAGN population, where the emitting gas is excited by a central AGN from retired galaxies (RG), where the gas emission may be due to excitation by hot, evolved (post-asymptotic giant branch – post-AGB) stars, in which case the Hα equivalent width is smaller than 3 Å (e.g. Belfiore et al. 2016; Brum et al. 2017).

The WHAN diagram for IRAS 23199E is shown in the left-hand panel of Fig. 7, while the right-hand panel of this figure shows the corresponding excitation map, with the distinct excitation classes identified. The red triangle represents the nucleus, as obtained from the fitting of the line profiles from an integrated nuclear spectrum within 0.4 arcsec radius. Although the Hα broad component is seen to up to 0.8 arcsec from the nucleus – due to the wings of the point spread function (PSF), the smaller aperture of 0.4 arcsec was chosen here to focus on the AGN emission, most of which is contained within this aperture (the PSF FWHM measured from field stars flux distribution is 0.85 arcsec). The blue triangles correspond to the extranuclear locations identified in Fig. 5. The green triangle corresponds to the spectrum from region E described above where there is an enhancement of both the line ratio and the velocity dispersion σ. All points are located within the region expected for emission of gas excited by an AGN or starburst. In particular, the point corresponding to the nucleus is clearly located within the sAGN region (strong AGN), indicating that the nuclear emission originates in a Seyfert-type AGN, in agreement with the presence of the broad Hα component. In addition to the nucleus, region E can also be classified as sAGN. At this location, the [N II] λ6583/Hα ratio is even larger than for the nucleus, possibly that shocks contribute to the gas excitation. The blue triangles corresponding to the extranuclear regions identified in Fig. 5 are located very close to the line that separates starburst from sAGN excitation, indicating that both the central AGN and star-forming regions contribute to the gas excitation at these locations.

We note that there is a general trend for higher [N II] λ6583/Hα to be associated with larger σ values. Some of these regions surround the contours of the 3-cm radio emission, as shown in Fig. 6. We thus attribute the gas emission at high-σ and [N II]/Hα ratio as at least being partly produced by excitation of the gas by shocks associated with produced by the radio-emitting plasma. There are also some regions to the south of the nucleus where there is no radio emission but there is still enhancement of the σ and line ratios, which we attribute to the presence of additional perturbations possibly due to the interaction between the two galaxies in IRAS F23199+0123.

4.2 Star-forming regions

As discussed in previous sections, we identify several knots of enhanced Hα emission, associated with star-forming regions. These knots are labelled A, B, and C in Fig. 5. In order to characterize the star formation at these locations, we use the integrated fluxes within the circular apertures shown in Fig. 5. These fluxes have been used to estimate physical properties of the star-forming regions that are

Table 1. Physical properties of the star-forming regions in IRAS 23199E.

Region	$L_{H\alpha}$ (10^{41} erg s^{-1})	EqW [Hα]	M (10^5 M$_\odot$)	log Q[H$^+$] (s^{-1})	SFR (M$_\odot$ yr^{-1})
A	0.12	44.41	3.06	52.10	0.09
B	0.07	28.41	1.78	51.87	0.05
C	0.16	45.84	4.08	52.23	0.12

listed in Table 1. In order to estimate the mass of ionized gas we used (Peterson 1997)

$$\frac{M}{\mathrm{M}_\odot} \approx 2.3 \times 10^5 \frac{L_{41}(\mathrm{H}\alpha)}{n_3^2}, \quad (1)$$

where L_{41}(Hα) is the Hα luminosity in units of 10^{41} erg s^{-1} and n_3 is the electron density (N_e) in units of 10^3 cm^{-3}. We have assumed $N_e = 300$ cm^{-3}, which is the mean value of electron density of circumnuclear star-forming regions derived from the [S II] λ 6717/λ 6731 intensity ratio (Díaz et al. 2007; Dors et al. 2008). The values of the mass of ionized gas for each star-forming complex are in the range (1.78–4.08) $\times$ 10^5 M$_\odot$.

We estimated the rate of ionizing photons Q[H$^+$] and star formation rate (SFR) under the assumption of a continuous star-forming regime. The rate of ionizing photons for each star-forming region was derived using Osterbrock (1989)

$$Q[\mathrm{H}^+] = \frac{\alpha_B L_{H\alpha}}{\alpha_{H\alpha}^{EFF} h \nu_{H\alpha}}, \quad (2)$$

where α_B is the hydrogen recombination coefficient to all energy levels above the ground level, $\alpha_{H\alpha}^{EFF}$ is the effective recombination coefficient for Hα, h is the Planck constant, and $\nu_{H\alpha}$ is the frequency of the Hα line. Using $\alpha_B = 2.59 \times 10^{13}$ cm^3 s^{-1} and $\alpha_{H\alpha}^{EFF} = 1.17 \times 10^{-17}$ cm^3 s^{-1} (Osterbrock 1989) we obtain

$$\left(\frac{Q[\mathrm{H}^+]}{\mathrm{s}^{-1}}\right) = 1.03 \times 10^{12} \left(\frac{L_{H\alpha}}{\mathrm{s}^{-1}}\right). \quad (3)$$

The SFR was computed using the following relation (Kennicutt 1998):

$$\frac{\mathrm{SFR}}{\mathrm{M}_\odot\ \mathrm{yr}^{-1}} = 7.9 \times 10^{-42} \frac{L_{H\alpha}}{\mathrm{erg\ s}^{-1}}. \quad (4)$$

SFRs derived for the star-forming regions of IRAS 23199E are in the range 0.05–0.12 M$_\odot$ yr^{-1}, consistent with a moderate star-forming regime. These SFRs fall within the range observed for circumnuclear star-forming regions in nearby Seyfert galaxies, derived using optical (Dors et al. 2008) and near-IR (Falcón-Barroso et al. 2014; Riffel et al. 2016) emission lines and are consistent with the average value of SFR = 0.14 M$_\odot$ yr^{-1} for a sample of 385 galaxies.

The values of the ionizing photons rate are in the range log Q[H$^+$] = (51.87–52.23) s^{-1} and are in agreement with previous reported values for circumnuclear star-forming regions in nearby galaxies (e.g. Wold & Galliano 2006; Galliano & Alloin 2008; Riffel et al. 2009, 2016).

The masses of ionized gas derived for the star-forming complexes in IRAS F23199E are in the range of (1.78–4.08) $\times$ 10^5 M$_\odot$, and agree with those previously obtained for star-forming regions surrounding Seyfert nuclei (e.g. Riffel et al. 2016).

We can also use the far-infrared (FIR) luminosity of galaxy to calculate the SFR (Kennicutt 1998):

$$\mathrm{SFR}(\mathrm{M}_\odot\ \mathrm{yr}^{-1}) = 4.5 \times 10^{-44} L_{FIR}\ (\mathrm{erg\ s}^{-1}), \quad (5)$$

where L_{FIR} is the IR luminosity integrated over the mid- and far-IR spectrum (8–1000 μm). Using $L_{FIR} = 1.35 \times 10^{11}$ erg s^{-1} (Darling & Giovanelli 2006), we obtain SFR $\approx$ 61 M$_\odot$ yr^{-1}. This value is much higher than those obtained for each star-forming region (shown in Table 1) and suggests that most of the FIR luminosity may not be due to star formation, but to the AGN, or most of the star formation is embedded in dust.

4.3 Gas kinematics

The velocity fields shown in Fig. 5 are complex, but they suggest the presence of a rotation pattern with the line of nodes oriented approximately along the east–west direction. In order to describe analytically this behaviour, we used a simple rotation model (van der Kruit & Allen 1978; Bertola et al. 1991), which assumes that the gas moves in circular orbits in the plane of the galaxy, within a central gravitational potential. In this model, the rotation velocity field is given by

$$V_{mod}(R,\psi) = v_s + \frac{A\,R\cos(\psi-\psi_0)\sin(i)\cos^p(i)}{\{R^2[\sin^2(\psi-\psi_0)+\cos^2(i)\cos^2(\psi-\psi_0)]+c_0{}^2\cos^2(i)\}^{\frac{p}{2}}}, \quad (6)$$

where R and ψ are the coordinates of each pixel in the plane of the sky, v_s is the systemic velocity of the galaxy, A is the velocity amplitude, ψ_0 is the major axis position angle, i is the disc inclination relative to the plane of the sky ($i = 0$ for face-on disc), p is a model fitting parameter (for $p =$ 1 the rotation curve at large radii is asymptotically flat while for $p =$ 3/2 the system has a finite mass), and c_0 is a concentration parameter, defined as the radius where the rotation curve reaches 70 per cent of its velocity amplitude.

The [N II] and Hα emission lines present similar velocity fields (Fig. 5), so we have chosen the Hα velocity field to perform the fit, as this line is stronger than [N II] λ6583 at most locations.

The observed velocities were fitted with the equation above using the MPFITFUN routine (Markwardt 2009) in IDL,[2] which performs a non-linear least-squares fit, after initial guesses for the parameters. During the fit, the position of the kinematical centre was kept fixed to the position of the peak of the flux distribution of the broad Hα component, adopted as the location of the nucleus of the galaxy and the parameter p was kept fixed at $p = 1.5$, as done in previous works (e.g. Brum et al. 2017).

The resulting best-fitting model is shown in the central panel of Fig. 8 and its parameters are $A = 349 \pm 26$ km s^{-1}, $v_s = 37\,947 \pm 2$ km s^{-1} (corrected for the heliocentric rest frame), $\psi_0 = 95^\circ \pm 2^\circ$, $c_0 = 1.6 \pm 0.1$ arcsec, $i = 41^\circ \pm 6^\circ$. The systemic velocity of the galaxy can be compared with previous measurements.

[2] http://www.harrisgeospatial.com/ProductsandSolutions/Geospatial Products/IDL.aspx

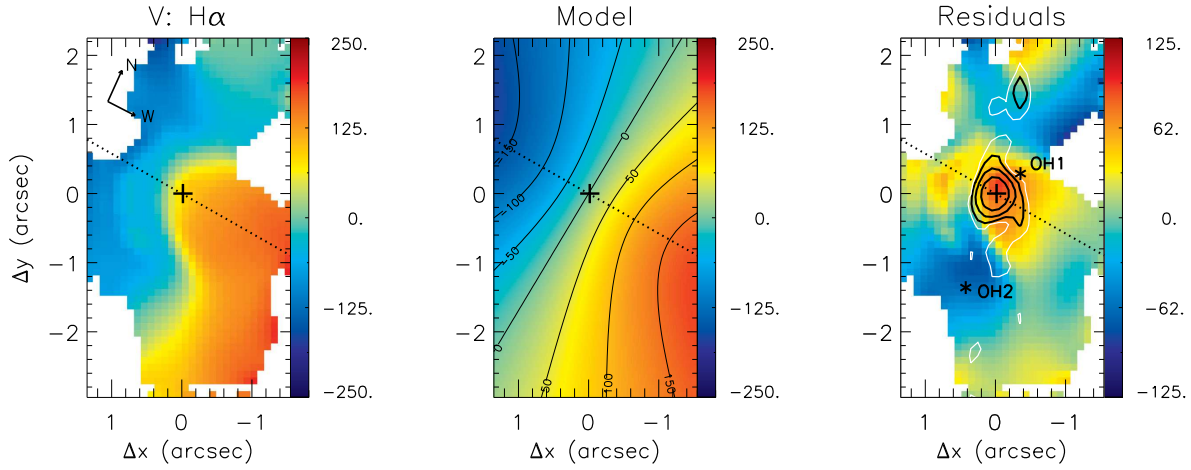

Figure 8. Observed Hα velocity field (left), rotating disc model (centre), and residual between the two (right). The central cross marks the position of the nucleus, the white regions are masked locations where we were not able to fit the emission-line profiles, and the dotted lines represent the orientation of the line of nodes. The black contours in the residual map are from the 3-cm radio image with the same flux levels as shown in Fig. 2, and the white contours show radio contours at the 1.5σ level. The black asterisks labelled OH1 and OH2 mark the position of the maser sources.

Lawrence et al. (1999) described the construction of the QDOT survey, which consists of IR properties and redshifts of an all-sky sample of 2387 *IRAS* galaxies. They obtained a systemic velocity for IRAS F23199+0123 of 40 981 km s^{-1}. On the other hand, Darling & Giovanelli (2006) performed an optical spectrophotometric study of resolved spectra of multiple nuclei merging systems that hosts OHM sources and obtained $v_s = 40\,679 \pm 2$ km s^{-1}. We note that the systemic velocity derived here is smaller than those obtained in previous studies. We speculate that this difference may be due to the fact that previous works possibly have observed the western nucleus, which is brighter, since at that time it was not known that IRAS F23199+0123 is composed by two members.

Besides the disc rotation model, Fig. 8 shows also the observed Hα velocity field in the left-hand panel and the residual map between the observed velocities and the model in the right-hand panel. The residual velocity map shows values much smaller than the observed velocity amplitude, but residuals of up to 100 km s^{-1} are present at some locations. Blueshifts are seen to the south and north of the nucleus, while redshifts are observed at the nucleus and its surroundings.

In order to investigate the origin of the velocity residuals, we have overlaid the contours from the 3-cm radio image on the residual map shown in the right-hand panel of Fig. 8. In this figure, we have plotted also the radio contours at the 1.5σ level (in white), as these levels show that faint radio emission is elongated towards the region where blueshifts are observed to the north of the nucleus. At the 3σ level there is just a hint of this elongation. This apparent association of the extended radio emission (although at faint levels) with the blueshifts in the map of velocity residuals suggests that the radio-emitting plasma may play a role in the gas kinematics and a possible interpretation is that the blueshifted residuals are due gas pushed away from the nucleus by a radio jet. Other indications of the interaction between the radio plasma and the emitting gas are the higher velocity dispersion and [N II]/Hα values surrounding the radio structures, as seen in Figs 5 and 6. Similar results have been found for other galaxies and interpreted as originating from the interaction of the radio jet with the ambient gas (e.g. Riffel et al. 2006; Riffel, Storchi-Bergmann & Riffel 2015).

We speculate that the observed blueshifts originate in outflows along a bicone oriented in the north–south direction with its axis approximately in the plane of the sky. The blueshifts would come from the front walls (nearside) of the cones to both sides of the nucleus, while the redshifts from the back (farside) walls are not observed probably due to obscuration. The redshifts that are observed surrounding the nucleus could be due to inflows towards the nucleus, probably due to gas motions associated with the interaction between the two galaxies of the pair.

Finally, it is interesting to note that the OH masers are observed in the vicinity of the active nucleus of IRAS F23199E, close to regions of enhanced velocity dispersion and [N II]/Hα ratio in the emitting gas. This suggests that the maser sources are associated with the AGN, perhaps produced in gas compressed in an interaction with expanding radio plasma. We also notice that the redshifted maser source (OH1) is located in a region with redshifted residuals, while the blueshifted maser source (OH2) is located in a region of blueshifted residuals, suggesting that the OH2 source is participating in the outflow.

4.4 The nature of the nuclear emission

Darling & Giovanelli (2006) presented a study of the optical properties of the Arecibo Observatory OHM survey sample, with the aim of investigating the types of nuclear environments that produce OHMs. They determined that IRAS F23199+0123 harbours a Seyfert 2 nucleus, based on an optical spectrum but the spectra used for the classification includes both nuclei, thus it was not possible to reveal the nature of each nucleus separately.

With our data we have discovered that IRAS 23199E harbours a Seyfert 1 nucleus, as we clearly detected a broad unresolved Hα component at the nucleus and the WHAN diagram is consistent with Seyfert-like gas excitation there. The double-peaked nature of this broad component suggests it is due to unresolved disc rotation in the BLR, as many recent studies have supported a flattened geometry for this region (Storchi-Bergmann et al. 2017). In the narrow-line region (NLR), jet–cloud interaction may give rise to double-peaked lines (e.g. Capetti et al. 1999; O'Dea et al. 2002;

Kharb et al. 2017) and another possibility is that some interaction with the radio emission may be happening in the BLR in this particular case. The discrepancy between Darling's classification and ours can be understood if Darling & Giovanelli (2006) observed the western nucleus, which appears brighter in our *HST* image and in the Sloan Digital Sky Survey (SDSS) image (Bundy et al. 2015; Albareti et al. 2017).

We estimate the mass of the central black hole using the empirical relation given by Greene & Ho (2005):

$$\frac{M_{\rm BH}}{\rm M_\odot} = (2.0^{+0.4}_{-0.3}) \times 10^6 \left(\frac{L_{\rm H\alpha}}{10^{42}\,\rm erg\,s^{-1}}\right)^{0.55\pm0.02} \left(\frac{\rm FWHM_{H\alpha}}{10^3\,\rm km\,s^{-1}}\right)^{2.06\pm0.06}, \quad (7)$$

where $M_{\rm BH}$ is the black hole mass, $L_{\rm H\alpha}$ is the luminosity, and $\rm FWHM_{H\alpha}$ is the full width at half-maximum of the broad component. The luminosity was calculated as the sum of the luminosities of both components, resulting in $L_{\rm H\alpha} \approx 1.8 \times 10^{41}\,\rm erg\,s^{-1}$. We obtained the $\rm FWHM_{H\alpha}$ of $2170\,\rm km\,s^{-1}$ directly from the observed profile. Using these values we have estimated a black hole mass of $3.8^{+0.3}_{-0.2} \times 10^6\,\rm M_\odot$.

5 CONCLUSIONS

We present a multiwavelength study of the OHM galaxy IRAS F23199+0123 using the *HST*, VLA, and Gemini North Telescope. Our *HST* images show that this system is an interacting pair of galaxies and used integral field spectroscopic data obtained with the GMOS-IFU to observe its eastern nucleus, which we call IRAS F23199E. Our observations cover the inner $9.5 \times 13\,\rm kpc^2$ of the galaxy at a spatial resolution of 2.3 kpc and velocity resolution of $\sim$70 km s^{-1}. Our main conclusions are as follows.

(i) We show that IRAS F23199+0123 is an interacting pair with a tidal tail connecting the two galaxies and detect two OH maser sources associated with the eastern member.

(ii) Both nuclei present extended radio emission at 3 and 20 cm, with intensity peaks at the each nucleus. The 20 cm radio emission of the eastern nucleus is elongated in the direction of the most extended emission in the *HST* continuum image (north-east–south-west), while in the western nucleus the 20 cm radio emission is tilted by about 45° eastwards relative to the orientation of the most extended continuum emission. In the better spatially resolved 3-cm observations, some elongation is observed at low brightness level towards the north in the eastern nucleus.

(iii) One of the main results of this paper is the discovery of a Seyfert 1 nucleus in IRAS F23199E, via the detection of an unresolved broad (FWHM $\approx 2200\,\rm km\,s^{-1}$) double-peaked component in the Hα emission line from the BLR. This is important in regard to the OH maser emission, because the two masing sources are detected in this galaxy that hosts an AGN, rather than the other member of the pair. In addition, the masing sources are observed in the vicinity of enhanced velocity dispersion and higher line ratios, suggesting that they are associated with shocks driven by AGN outflows. The blue- and redshifted maser sources are associated with the blue- and redshifted ionized gas velocity residuals. This combination of evidence from *HST* images, VLA line spectroscopy, and IFU spectroscopy strongly indicates that in this system the OHM sources are associated with the AGN rather than star formation.

(iv) Using the width and luminosity of the broad Hα profile, we estimate a mass of $M_{\rm BH} = 3.8^{+0.3}_{-0.2} \times 10^6\,\rm M_\odot$ for the central supermassive black hole.

(v) The comparison between the *HST* [N II]+Hα image and GMOS-IFU emission-line flux distributions of IRAS F23199E shows that they are similar, being more elongated in the north-east–south-west direction, following the continuum emission. In addition, the GMOS Hα flux map reveals the presence of three extranuclear knots, attributed to star-forming regions.

(vi) From the measurement of the Hα fluxes from the star-forming regions, we obtain: (1) SFRs in the range (0.05–0.12) $\rm M_\odot\,yr^{-1}$; (2) ionized gas content in the range (1.8–4.1) $\times 10^5\,\rm M_\odot$; and (3) ionized photons rate $\log Q[\rm H^+] = 51.9$–$52.2\,\rm s^{-1}$. From the FIR luminosity we obtain SFR $\approx 61\,\rm M_\odot\,yr^{-1}$ suggesting that most of the FIR luminosity may be due to the AGN or due to star formation embedded in dust.

(vii) The [N II] λ6583/Hα flux ratio map of IRAS 23199E presents the highest values coincident with the regions with highest σ values, which surround the radio source and suggests that the radio-emitting plasma interacts with the ambient gas via shocks that seem to play a role in the gas excitation. The lowest [N II] λ6583/Hα values are cospatial with the star-forming regions detected in the Hα emission.

(viii) The velocity fields of IRAS F23199E show a disturbed rotation pattern with the line of nodes oriented along PA = 95°, as derived by the fit of the Hα velocities with a rotation disc model. The residuals between the observed and modelled velocity field combined with the velocity dispersion maps suggest the presence of non-circular motions, possibly due to outflows from the nucleus along the directions north and south and inflows towards the nucleus in its vicinity.

ACKNOWLEDGEMENTS

We thank an anonymous referee for useful suggestions that helped to improve the paper. This work is based on observations obtained at the Gemini Observatory, which is operated by the Association of Universities for Research in Astronomy, Inc., under a cooperative agreement with the NSF on behalf of the Gemini partnership: the National Science Foundation (USA), the Science and Technology Facilities Council (UK), the National Research Council (Canada), CONICYT (Chile), the Australian Research Council (Australia), Ministério da Ciência e Tecnologia (Brazil), and south-eastCYT (Argentina). This research has made use of the NASA/IPAC Extragalactic Database (NED) that is operated by the Jet Propulsion Laboratory, California Institute of Technology, under contract with the National Aeronautics and Space Administration. The National Radio Astronomy Observatory is a facility of the National Science Foundation operated under cooperative agreement by Associated Universities, Inc. We acknowledge the usage of the HyperLeda data base (http://leda.univ-lyon1.fr). CH thanks for CAPES financial support. The Brazilian authors acknowledge support from FAPERGS and CNPq.

REFERENCES

Albareti F. D. et al., 2017, ApJS, 233, 25
Allington-Smith J. et al., 2002, PASP, 114, 892
Baldwin J. A., Phillips M. M., Terlevich R., 1981, PASP, 93, 5
Belfiore F. et al., 2016, MNRAS, 461, 3111
Bertola F., Bettoni D., Danziger J., Sadler E., Sparke L., de Zeeuw T., 1991, ApJ, 373, 369
Brum C., Riffel R. A., Storchi-Bergmann T., Robinson A., Schnorr Muller A., Lena D., 2017, MNRAS, 469, 3405
Bundy K. et al., 2015, ApJ, 798, 7

Capetti A., Axon D. J., Macchetto F. D., Marconi A., Winge C., 1999, ApJ, 518, 187
Cid Fernandes R., Stasinska G., Schlickmann M. S, Mateus A., Vale Asari N., Schoenell W., Sodre L., 2010, MNRAS, 403, 1036
Cid Fernandes R., Stasinska G., Mateus A., Vale Asari N., 2011, MNRAS, 413, 1687
Conway J. E., Cornwell T. J., Wilkinson P. N., 1990, MNRAS, 246, 490
Darling J., Giovanelli R., 2001, AJ, 121, 1278
Darling J., Giovanelli R., 2002, ApJ, 572, 810
Darling J., Giovanelli R., 2006, AJ, 132, 2596
Díaz Á. I., Terlevich E., Castellanos M., Hägele G. F., 2007, MNRAS, 382, 251
Dors O. L., Storchi-Bergmann T., Riffel R. A., Schmidt A. A., 2008, A&A, 482, 59
Falcón-Barroso J., Ramos Almeida C., Boker T., Schinnerer E., Knapen J. H., Lançon A., Ryder S., 2014, MNRAS, 438, 329
Galliano E., Alloin D., 2008, A&A, 487, 519
Gonzalez R. C., Woods R. E., 2002, Digital Image Processing, 2nd edn. Prentice-Hall, Englewood Cliffs, NJ
Greene J. E., Ho L. C., 2005, ApJ, 630, 122
Hook I., Jorgensen I., Allington-Smith J. R., Davies R. L., Metcalfe N., Murowinski R. G., Crampton D., 2004, PASP, 116, 425
Hoopes C. G., Walterbos R. A. M., Rand R. J., 1999, ApJ, 522, 669
Kennicutt R. C., 1998, ARA&A, 36, 189
Kharb P., Subramanian S., Vaddi S., Das M., Paragi Z., 2017, ApJ, 846, 12
Lawrence A. et al., 1999, MNRAS, 308, 897
Lena D., 2014, preprint (arXiv:1409.8264)
Lo K. Y., 2005, ARA&A, 43, 625
McMullin J. P., Waters B., Schiebel D., Young W., Golap K., 2007, in Shaw R. A., Hill F., Bell D. J., eds, ASP Conf. Ser. Vol. 376, Astronomical Data Analysis Software and Systems XVI. Astron. Soc. Pac., San Francisco, p. 127
Markwardt C. B., 2009, in Bohlender D. A., Durand D., Dowler P., eds, ASP Conf. Ser. Vol. 411, Astronomical Data Analysis Software and Systems XVIII. Astron. Soc. Pac., San Francisco, p. 251
Menezes R. B., Steiner J. E., Ricci T. V., 2014, MNRAS, 438, 2597
Menezes R. B., da Silva P., Ricci T. V., Steiner J. E., May D., Borges B. W., 2015, MNRAS, 450, 369
O'Dea C. P. et al., 2002, AJ, 123, 2333
Osterbrock D. E., 1989, Astrophysics of Gaseous Nebulae and Active Galactic Nuclei. University Science Books, Mill Valley, CA
Pearson T. J., Readhead A. C. S., 1984, ARA&A, 22, 97
Peterson B. M., 1997, An Introduction to Active Galactic Nuclei. Cambridge Univ. Press, Cambridge
Rau U., Cornwell T. J., 2011, A&A, 532, A71
Riffel R. A., 2010, Ap&SS, 327, 239
Riffel R. A., Storchi-Bergmann T., Winge C., Barbosa F. K. B., 2006, MNRAS, 373, 2
Riffel R. A., Storchi-Bergmann T., Dors O. L., Winge C., 2009, MNRAS, 393, 783
Riffel R. A., Storchi-Bergmann T., Riffel R., 2015, MNRAS, 451, 3587
Riffel R. A. et al., 2016, MNRAS, 461, 4192
Rossa J., Dettmar R.-J., 2000, A&A, 359, 433
Rossa J., Dettmar R.-J., 2003, A&A, 406, 505
Sales D. A. et al., 2015, ApJ, 799, 25
Schwab F. R., 1984, AJ, 89, 1076
Storchi-Bergmann T., Dors O. L., Jr, Riffel R. A., Fathi K., Axon D. J., Robinson A., Marconi A., Ostlin G., 2007, ApJ, 670, 959
Storchi-Bergmann T., Schimoia J. S., Peterson B. M., Elvis M., Denney K. D., Eracleous M., Nemmen R. S., 2017, ApJ, 835, 236
Tody D., 1986, in Crawford D. L., ed., Proc. SPIE Vol. 627, Instrumentation in Astronomy VI. SPIE, Bellingham, p. 733
Tody D., 1993, in Hanisch R. J., Brissenden R. J. V., Barnes J., eds, ASP Conf. Ser. Vol. 52, Astronomical Data Analysis Software and Systems II. Astron. Soc. Pac., San Francisco, p. 173
van der Kruit P. C., Allen R. J., 1978, ARA&A, 16, 103
van Dokkum P. G., 2001, PASP, 113, 1420
Wold M., Galliano E., 2006, MNRAS, 369, 47

This paper has been typeset from a TEX/LATEX file prepared by the author.

5 RESULTADOS E DISCUSSÕES PARA IRAS03056+2034

A editora Oxford University Press(OUP) reserva aos autores que contribuem para suas revistas o direito de incluir seus manuscritos na íntegra ou trechos dos mesmos em dissertações ou teses, sem a necessidade autorização prévia. [1]

[1] https://academic.oup.com/journals/pages/access_purchase/rights_and_permissions_publication_rights.

Monthly Notices of the ROYAL ASTRONOMICAL SOCIETY

MNRAS **479,** 3966–3977 (2018) doi:10.1093/mnras/sty1606
Advance Access publication 2018 June 18

Star formation and gas inflows in the OH megamaser galaxy IRAS03056+2034

C. Hekatelyne,[1⋆] Rogemar A. Riffel,[1⋆] Dinalva Sales,[2] Andrew Robinson,[3] Thaisa Storchi-Bergmann,[4⋆] Preeti Kharb,[5] Jack Gallimore,[6] Stefi Baum[7,8] and Christopher O'Dea[7,9]

[1]*Departamento de Física, CCNE, Universidade Federal de Santa Maria, Santa Maria 97105-900, RS, Brazil*
[2]*Instituto de Matemática, Estatística e Física, Universidade Federal do Rio Grande, Rio Grande 96203-900, Brazil*
[3]*School of Physics and Astronomy, Rochester Institute of Technology, 84 Lomb Memorial Drive, Rochester, NY 14623, USA*
[4]*Departamento de Astronomia, Universidade Federal do Rio Grande do Sul. 9500 Bento Gonçalves, Porto Alegre 91501-970, Brazil*
[5]*National Centre for Radio Astrophysics, Tata Institute of Fundamental Research, S. P. Pune University Campus, Post Bag 3, Ganeshkhind, Pune 411 007, India*
[6]*Department of Physics, Bucknell University, Lewisburg, PA 17837, USA*
[7]*Department of Physics and Astronomy, University of Manitoba, Winnipeg, MB, R3T 2N2, Canada*
[8]*Center for Imaging Science, Rochester Institute of Technology, 84 Lomb Memorial Dr., Rochester, NY 14623, USA*
[9]*School of Physics & Astronomy, Rochester Institute of Technology, 84 Lomb Memorial Dr., Rochester, NY 14623, USA*

Accepted 2018 June 11. Received 2018 June 8; in original form 2018 April 20

ABSTRACT

We have obtained observations of the OH megamaser galaxy IRAS03056+2034 using the Gemini Multi-Object Spectrograph (GMOS) Integral Field Unit (IFU), Very Large Array (VLA), and *Hubble Space Telescope* (*HST*). The *HST* data reveals spiral arms containing knots of emission associated with star-forming regions. The GMOS-IFU data cover the spectral range of 4500–7500 Å at a velocity resolution of 90 km s^{-1} and spatial resolution of 506 pc. The emission-line flux distributions reveal a ring of star-forming regions with radius of 786 pc centred at the nucleus of the galaxy, with an ionized gas mass of 2.1×10^5 M$_\odot$, an ionizing photon luminosity of log Q[H$^+$] = 53.3, and a star formation rate of 1.4 M$_\odot$ yr^{-1}. The emission-line ratios and radio emission suggest that the gas at the nuclear region is excited by both starburst activity and an active galactic nucleus. The gas velocity fields are partially reproduced by rotation in the galactic plane, but show, in addition, excess redshifts to the east of the nucleus, consistent with gas inflows towards the nucleus, with velocity of ∼45 km s^{-1} and a mass inflow rate of $\sim 2.2 \times 10^{-3}$ M$_\odot$ yr^{-1}.

Key words: galaxies: individual: IRAS03056+2034 – galaxies: kinematics and dynamics – galaxies: nuclei.

1 INTRODUCTION

OH megamasers (hereafter OHMs) are powerful extragalactic masers in which emission occurs predominantly in the 1667/1665 MHz lines with typical luminosities of about 10^3 L$_\odot$. The isotropic luminosity of OHMs is 10^8 times greater than the luminosity of the OH masers in the Milk Way. The megamasers can be explained on the basis of amplification of the nuclear radio continuum by foreground molecular material with inverted level populations arising from some pumping source (e.g. Baan, Salzer & LeWinter 1998; Lo 2005).

In general, OHMs have been observed in (ultra) luminous infrared galaxies [(U)LIRGs] with infrared luminosities of $L_{\rm IR} >= 10^{11}$ L$_\odot$. These merging systems fulfill all the requirements for producing OHM emission. The merger interaction concentrates molecular gas in the galactic nuclei, creates strong dust emission from the starburst (SB) and active galactic nucleus (AGN) activity, and produces radio continuum emission from the AGN or SB (e.g. Henkel, Guesten & Baan 1987; Darling & Giovanelli 2000).

It is not well understood if the mechanism of ionization in the systems that host OHM is dominated by star formation or AGN activity, in the sense that the hosts of OHM emission usually present features of both phenomena in their spectra. A possible explanation for these features is that they originate in a central AGN, contaminated by emission of circumnuclear star-forming regions, as

⋆ E-mail: hekatelyne.carpes@gmail.com (CH); rogemar@ufsm.br (RAR); thaisa@ufrgs.br (TS-B)

the angular resolution of the observations usually corresponds to a few kiloparsecs at the galaxies. Alternatively, the OHM galaxies could represent a transition stage between a starburst and the emergence of an AGN, as suggested by Darling & Giovanelli (2006).

In an effort to investigate the nature of the ionization in OHM galaxies, we have been performing a multiwavelength study of a sample of these galaxies (Sales et al. 2015; Hekatelyne et al. 2018). In this paper, we present Gemini Multi-Object Spectrograph (GMOS) Integral Field Unit (IFU) observations, Very Large Array (VLA) continuum data, and *Hubble Space Telescope* (*HST*) narrow and broad-band images of the galaxy IRAS03056+2034, which is an LIRG that hosts OHM emission. This target is part of a sample including another 14 OHM galaxies, for which we have the same combination of *HST* and VLA data. The targets selected for IFU observations were chosen based on the morphology revealed by the *HST* images. This paper is part of a series based on multiwavelength observations with the aim of studying the gas kinematics and excitation of OHM galaxies.

In a previous paper (Hekatelyne et al. 2018), we mapped the eastern nucleus of the OHM galaxy IRASF23199+0123 using *HST*, VLA, and GMOS data. We were able to conclude that the object is an interacting pair with a tail connecting the two galaxies and detected two OH maser sources associated with the eastern member. Moreover, we discovered a Seyfert 1 nucleus in the eastern member of the pair, via detection of an unresolved broad double-peaked component in the H_α emission line. In addition, the masing sources were observed in the vicinity of a region of enhanced velocity dispersion and higher line ratios, suggesting that they are associated with shocks driven by AGN outflows. These results suggest that the OH megamaser emission in IRASF23199+0123 is associated with AGN activity. Sales et al. (2015) presented a multiwavelength study of the OH megamaser galaxy IRAS16399–0937 using *HST*, VLA, 2MASS, *Herschel*, and *Spitzer* data. This galaxy has two nuclei separated by 3.4 kpc and its infrared spectrum is dominated by strong polycyclic aromatic hydrocarbon, but the northern nucleus shows in addition deep silicate and molecular absorption features. The analysis of the spectral energy distribution reveals that the northern nucleus contains an AGN with bolometric luminosity of 10^{44} erg s^{-1}.

IRAS03056+2034 (hereafter IRAS03056) is a spiral galaxy (SB(rs)B; Vaucouleurs et al. 1991) that presents strong OHM emission. This detection was obtained with the Nancay radio telescope in 1990, indicating F_{IR} luminosity of 15×10^{10} L$_\odot$ (Bottinelli et al. 1990). Baan et al. (1998) used spectroscopic data obtained with the 200 inch Hale telescope at the Palomar Observatory in order to determine the optical classifications of 42 OHM galaxies, based on line ratios, and classified IRAS03056 as a starburst galaxy. We adopt the distance of 116 Mpc as derived by Theureau et al. (2007) from the Tully–Fisher relation.

We have obtained GMOS-IFU data covering the central region of IRAS03056 in order to map the distribution and kinematics of the emitting gas and investigate the origin of the line emission in the central region of this object. This paper is organized as follows. The observations and the data reduction procedure are described in Section 2. The emission-line flux distributions, emission-line ratio, and kinematics maps obtained from GMOS data, as well as the *HST* and VLA images, are presented in Section 3. These results are discussed in Section 4 and then in Section 5 we present the final remarks.

2 OBSERVATIONS AND DATA REDUCTION

2.1 *HST* images

The *HST* images of IRAS03056 were obtained with the Advanced Camera for Surveys (ACS). The acquired images consist of continuum and emission-line imaging of a sample of 15 OHM galaxies (Program id 11604; PI: D.J. Axon). The observations were done with the wide-field channel (WFC) using broad- (F814W), narrow- (FR656N), and medium-band (FR914M) filters. The total integration times were 600 s for the broad-band filter, 200 s for the medium-band filter, and 600 s for the narrow-band filter, which contains the Hα and [N II] lines.

The images were processed using IRAF packages (Tody 1986, 1993). First of all, the cosmic rays were removed from the images using the *LACOS IM* task (van Dokkum 2001). In order to build a continuum-free Hα + [N II] image of IRAS03056, we estimated the count rate for foreground stars considering the medium- and narrow-band images. This procedure allowed us to define a mean scaling factor that was applied to the medium-band image. It provided us a scaled image that was subtracted from the narrow-band image (Sales et al., in preparation).

Finally, the continuum-free image was inspected to certify that the residuals at the positions of the foreground stars are negligible. This procedure results in typical uncertainties of 5–10 per cent in flux (see Hoopes, Walterbos & Rand 1999; Rossa & Dettmar 2000, 2003).

2.2 VLA radio continuum data

We reduced archival VLA A-array data at 1.425 GHz from the project AB660. These data were acquired on 1992 December 14. The data were reduced following standard procedures in AIPS. The final image of IRAS03056 was created after a couple of phase-only and phase+amplitude self-calibrations, using the AIPS tasks CALIB and IMAGR iteratively. The r.m.s. noise in the image is $\sim 7 \times 10^{-5}$ Jy beam^{-1}. The restoring beam is 1.49 × 1.38 arcsec at a position angle (PA) = −35°. The peak intensity of the compact radio core seen in the image is ∼11 mJy beam^{-1}. An image at 4.86 GHz from the project AB660 at a resolution of 0.38 × 0.34 arcsec (beam PA = −34.5°) was also available in the NRAO image archive. A point source of peak intensity ∼1.7 mJy beam^{-1} is visible in this image; the r.m.s. noise is $\sim 8.7 \times 10^{-5}$ Jy beam^{-1}.

2.3 GMOS-IFU data

Optical spectroscopic data for IRAS03056 was obtained at the Gemini North telescope, using the GMOS-IFU (Allington-Smith et al. 2002; Hook et al. 2004). The observations were performed in 2013 October, November, and December (Gemini project GN-2013B-Q-97 – PI: D. Sales). The observations were carried out using the B600 grating in combination with the G5307 filter, with the major axis of the IFU oriented along PA = 120°, approximately along the major axis of the galaxy.

The total integration time was 12000 s divided into 10 individual exposures of 1200 s each. The one slit mode of GMOS-IFU was used, resulting in a total angular coverage of 5.0 × 3.5 arcsec, and a spectral range that includes the H α, [N II]λ6583, [S II]λ6717, Hβ, [O III]λ5007, and [O I]λ6300 emission lines.

In order to process the data, we followed the standard steps for spectroscopic data reduction using GEMINI package routines of

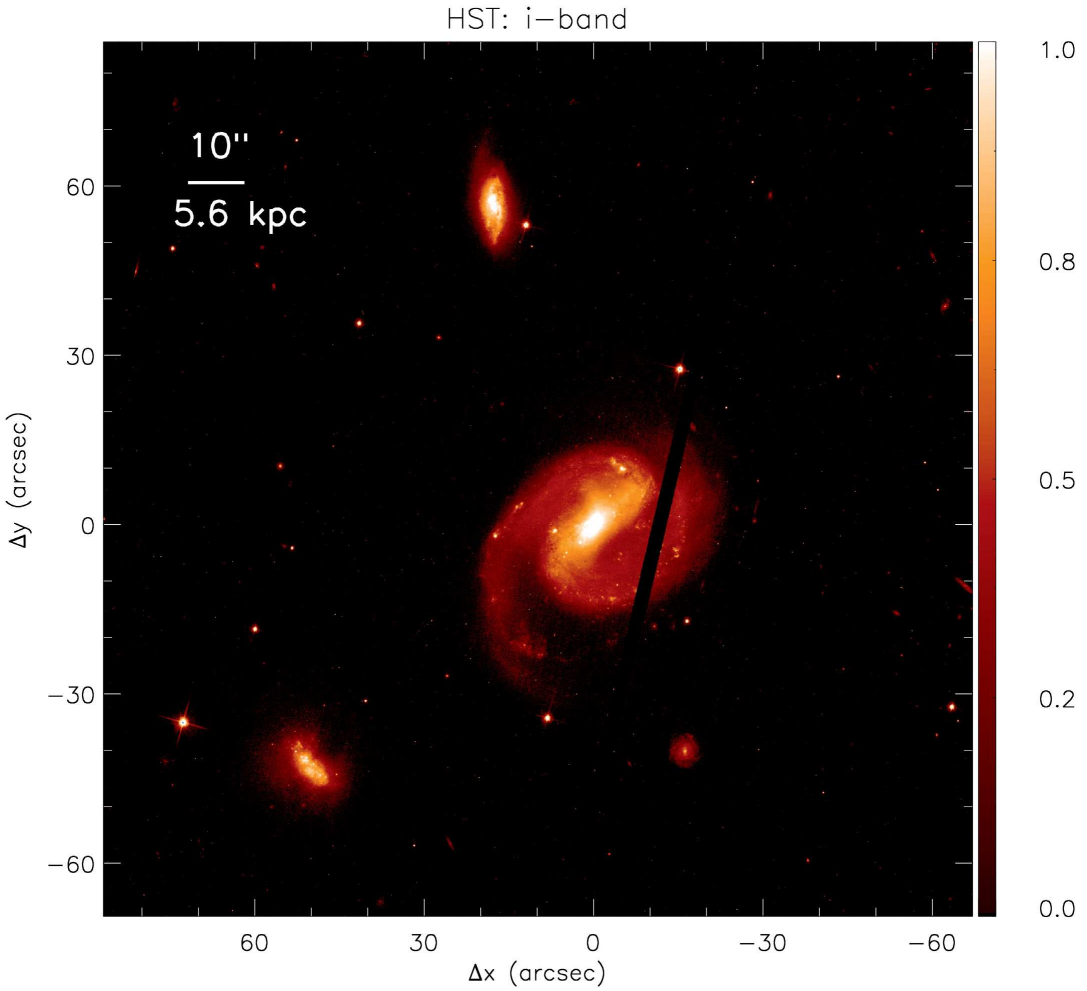

Figure 1. Large-scale *i*-band image of IRAS03056 obtained with *HST*.

IRAF (Lena 2014). The basic steps of the data reduction comprise bias level subtraction, flatfielding, trimming, and wavelength calibration. We used the CuAr arc lamps as reference in order to apply the wavelength calibration to the data and subtracted the sky emission contamination. In order to apply the flux calibration, we used a sensitivity function that was generated from a spectrum of the BD+28 4211 photometric standard star, observed on the same night as the galaxy exposures.

After flux calibration, we created data cubes for each exposure at a sampling of 0.1 × 0.1 arcsec. These data cubes were median combined using the IRAF *GEMCOMBINE* task resulting in the final data cube for the object. In the mosaicking process, we used as a reference the peak of the continuum emission and used the AVSIGCLIP algorithm to remove bad pixels.

The adopted GMOS configuration resulted in a spectral resolution of 1.8 Å, as obtained from the full width at half-maximum (FWHM) of the CuAr arc lamp lines used to perform the wavelength calibration, corresponding to 90 km s^{-1}. The angular resolution is 0.9 arcsec, as measured from the FWHM of field stars in the acquisition image. This corresponds to 506 pc at the galaxy.

As the final cube presented unwanted noise, we performed a spatial filtering using the IDL routine *bandpass_filter.pro*,[1] which allows the choice of the cut-off frequency (ν) and the order of the filter n. The filtering process does not change the angular resolution of the data and all measurements presented in the forthcoming sections were done using the filtered cube.

3 RESULTS

3.1 Large-scale structure and merger stage

IRAS03056+2034 has been spectroscopically classified as a starburst (Baan et al. 1998) with infrared and OH maser luminosities of $L_{IR} = 1.6 \times 10^{11}\,L_{\odot}$ and $\log L_{OH} = 1.3\,L_{\odot}$ (Baan et al. 2008; Kandalian 1996).

Fig. 1 shows the large-scale *i*-band image of IRAS03056 obtained with *HST*. This image shows a barred spiral galaxy with two symmetric arms. Two smaller companion galaxies at projected distances

[1]The routine is available at https://www.harrisgeospatial.com/docs/bandpass_-filter.html

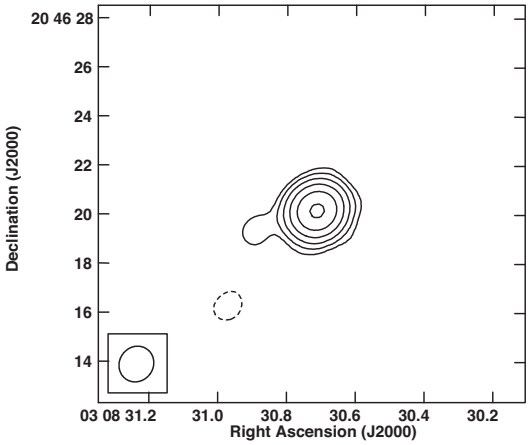

Figure 2. VLA radio continuum image of IRAS03056 at 20 cm. The contour levels are in percentage of the the peak intensity (=10.9 mJy beam^{-1}) and increase in steps of two, with the lowest contour levels being ±2.8 per cent.

of roughly 31 kpc and 34.1 kpc from the nucleus of IRAS03056 are seen to the north and to the south-east, respectively.

Haan et al. (2011) studied a sample of 73 nearby ($0.01 < z < 0.05$) LIRGs and classified the objects into six different merger stages, based on *H*-band *HST* images. Using their classification scheme, IRAS03056 is classified as type 1 (separated galaxies) and this group constitutes only 8.3 per cent of their sample.

Our large-scale images exhibit a scenario that, in general, IRAS03056 is a fairly typical example of an LIRG that has low infrared luminosity ($L_{IR} = 1.6 \times 10^{11}$ L$_\odot$) with a wide nuclear projected separation between the nuclear components, however presenting composite (starburst + AGN) spectra (see figure 12 and table 6 of Yuan, Kewley & Sanders 2010). In terms of star formation and molecular gas content, it is also important to note that IRAS03056 is widely similar to (U)LIRGs lying at the high end of the linear relation between the surface density of dense molecular gas (as traced by HCN) and the surface density of star formation rate (SFR) with a positive correlation coefficient (see figure 5 and table 2 of Liu, Gao & Greve 2015).

The two OHM galaxies previously studied by our group (Sales et al. 2015; Hekatelyne et al. 2018) show a more advanced merger stage than IRAS03056, presenting 'close binary' nuclei. In addition, the previously studied galaxies are slightly more luminous (log L_{IR} ≈ 11.5–11.6 L$_\odot$) than IRAS03056.

3.2 VLA and *HST* images

Fig. 2 shows the 20 cm continuum image of IRAS03056 obtained with VLA. A compact radio source is detected at the nucleus of the galaxy and no extended emission is seen. We created a (1.425 – 4.86) GHz spectral index image of IRAS03056 and found that the core has a steep spectral index of -1.02 ± 0.09; this is consistent with optically thin synchrotron emission that could arise in an AGN jet (Pacholczyk 1970). Moreover, we estimated the brightness temperature (T_B) of the 1.4 GHz radio core by using the total flux density (=11.7 mJy) and the beam-deconvolved size of the core (=0.51 x 0.24 arcsec), as derived from the AIPS Gaussian-fitting task JMFIT, and the T_B relation for an unresolved component from Ulvestad, Antonucci & Barvainis (2005). This turned out to be $= 1.8 \times 10^5$ K, supporting an AGN-related origin (e.g. Berton et al. 2018).

The *HST* images of IRAS03056 are presented in Fig. 3. The left-hand panels present the broad-band continuum (F814W) image (top panel) and the narrow-band [N II]+H α image (bottom panel) of the inner 20 × 20 arcsec^2 of IRAS03056. The green boxes represent the field of view (FoV) of the GMOS-IFU data. The right-hand panels shows a zoom of the central region of the *HST* images, corresponding to the GMOS FoV. The *HST* images were rotated to the same orientation of the GMOS-IFU data.

The *HST* continuum image shows the most elongated emission along PA ∼ 100/280° and presents a structure that seems to be associated with a spiral arm seen to the north-east of the nucleus. Moreover, the zoomed image (top right panel) shows a strip of emission that extends from 1 arcsec north to 1 arcsec south of the nucleus.

The H α+[N II] flux distribution is similar to that in the continuum but shows more clearly the presence of spiral arms, one to the west and another to the south-east of the nucleus. At the central region (bottom right panel), unresolved knots of emission are seen in both the H α+[N II] and the *i*-band images, one at 1.5 arcsec north and another at 1.5 arcsec east of the nucleus.

3.3 Emission-line flux distributions

Fig. 4 shows examples of IRAS03056 spectra obtained from the GMOS-IFU data cube for the three locations indicated as blue circles in the top-middle panel of Fig. 5 and labelled as N (nucleus), A (1.5 arcsec east), and B (1.0 arcsec south-west). These spectra were obtained by integrating the fluxes within circular apertures of 0.45 arcsec radius. The strongest emission lines are identified in the nuclear spectrum.

Aiming to map emission-line flux distributions, line-of-sight velocity (V_{LOS}), and velocity dispersion (σ) of the emitting gas, we have fitted the emission-line profiles of H α, [N II] λ6548,6583, H β, [S II] λ6717, [O I] λ6300 and [O III] λ5007 by Gaussian curves. The fitting procedure was performed using modified versions of the line-PROfile FITting (PROFIT) routine (Riffel 2010). This routine performs the modelling of the observed emission-line profile using the MPFITFUN routine (Markwardt 2009), via a non-linear least-squares fit. The outputs of the routine are the emission-line flux, the centroid velocity, the velocity dispersion, and their corresponding uncertainties for each emission line.

The fitting process for the [N II] λ6548,6583+H α complex was performed simultaneously, considering one Gaussian per line. During the fit, we kept tied the kinematics (V_{LOS} and σ) of the [N II] and fixed the [N II] λ6583/[N II] λ6548 intensity ratio to its theoretical value (3, Osterbrock 1989). The underlying continuum was fitted by a linear equation, constrained by the adjacent continuum regions.

Fig. 5 presents the flux distributions for H α, [N II] λ6583, [S II] λ6717, H β, [O III] λ5007, and [O I] λ6300 emission lines. The colour bars show the flux in logarithmic units of erg s^{-1} cm^2 and the grey regions represent masked locations where the signal-to-noise ratio was not high enough to obtain good fits of the emission-line profiles. These locations present flux uncertainty larger than 30 per cent. The central crosses mark the location of the nucleus, defined as the position of the peak of continuum emission. H α, [N II] λ6583, and [S II] λ6717 emission-lines flux distributions are similar, presenting extended emission over the whole GMOS FoV. One can notice the presence of unresolved knots of emission surrounding the nucleus at ∼1 arcsec from it.

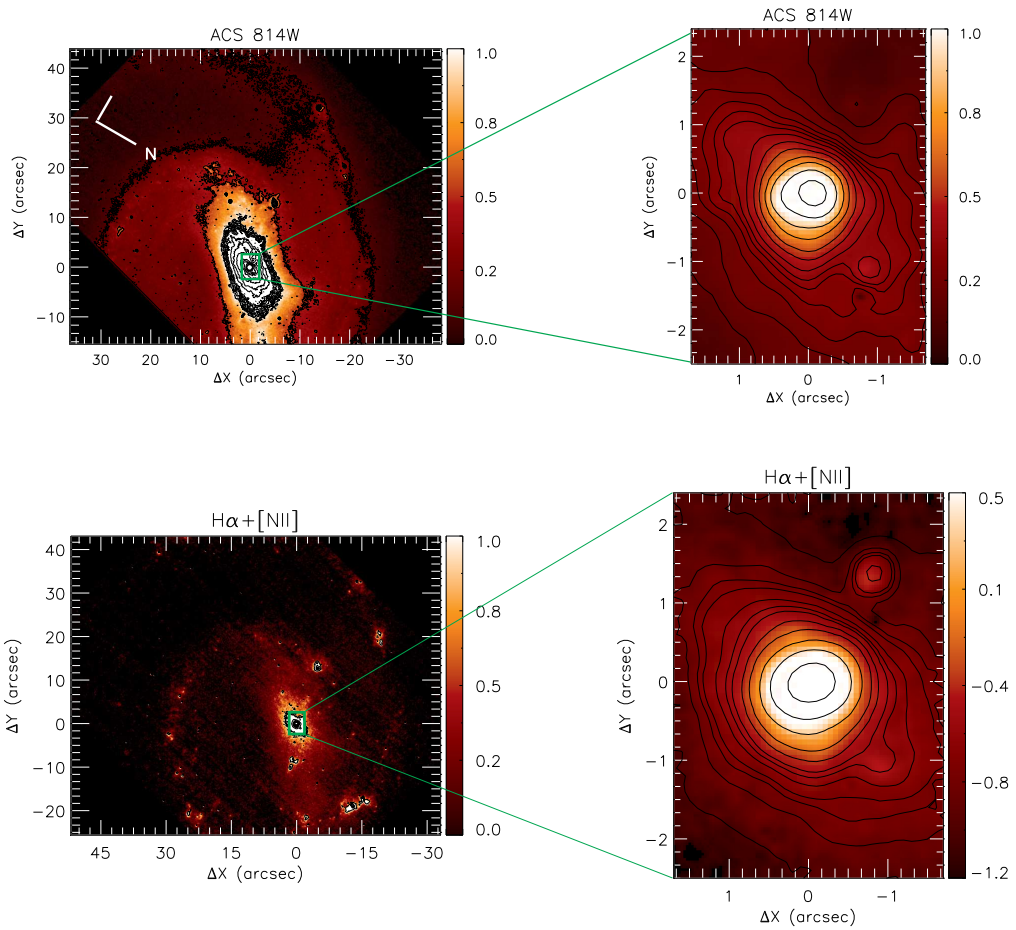

Figure 3. *HST* images of IRAS03056. Top panels: left – large-scale image (ACS/*HST* F814W – *i*-band); right – zoom of *i*-band image for the region observed with GMOS-IFU. Bottom panels: left – large-scale continuum-free H α+[N II] image; right – zoom at the region observed with GMOS-IFU. The green boxes show the GMOS-IFU FoV (3.5 × 5.5 arcsec) and the colour bars show the fluxes in arbitrary units.

The bottom panels of Fig. 5 show the flux distribution maps for H β, [O III] λ5007, and [O I] λ6300, which are generally detected only within a smaller region around the nucleus. As for H α, the H β flux map shows some unresolved knots of emission ∼1 arcsec away from the nucleus and faint extended emission is seen to up to 2 arcsec from it. The [O III] λ5007 emission is detected only very close to the nucleus, at distances smaller than 1 arcsec. The [O I] λ6300 emission is also mostly concentrated within ∼1 arcsec of the nucleus.

3.4 Line-ratio maps

The [N II] λ6583/H α, [S II] λ6717/H α, [O I] λ6300/H α, and [O III] λ5007/H β emission-line flux ratios can be used to investigate the origin of the line emission. The lines of each ratio above are close in wavelength and thus the effects of dust extinction can be neglected. Fig. 6 presents the flux ratio maps for [N II] λ6583/H α, [S II] λ6717/H α, [O I] λ6300/H α, and [O III] λ5007/H β.

The [N II] λ6583/H α ratio map is remarkably uniform, presenting small values of roughly 0.75, except for the regions located to the north and north-west of the nucleus, close to the borders of the GMOS FoV. The [S II] λ6717/H α map shows constant values of ∼0.2 surrounding the nucleus at ∼1 arcsec, approximately coincident with the ring of enhanced H α emission seen in Fig. 5. Some smaller values are seen within the ring and values of up to 0.5 are seen at larger distances from the nucleus. The [O I] λ6300/H α ratio map presents constant values of 0.02 within the inner 1 arcsec. The [O III] λ5007/H β ratio typically has values close to 0.2, but a few knots show higher values, reaching ∼0.5.

Fig. 7 shows the electron density N_e map, measured from the [S II] λ 6717/λ 6731 line ratio, assuming an electron temperature of 10000 K for the ionized gas as input for the *temden* routine in the STSDAS.IRAF package. The N_e map shows values ranging from 100 to 2200 cm^{-1}, with the highest ones observed at the nucleus and in unresolved structures in its surroundings.

3.5 Gas velocity fields and velocity dispersion maps

Fig. 8 presents the line-of-sight velocity fields (top panels) and the velocity dispersion maps (bottom panels) for the H α, [N II] λ6583, and [S II] λ6717 emission lines. As the H β, [O III] λ5007, and [O I] λ6300 emission is seen only closer to the nucleus, and the measured kinematics is similar to that seen in the other lines showing more extended emission, we do not show the corresponding maps for

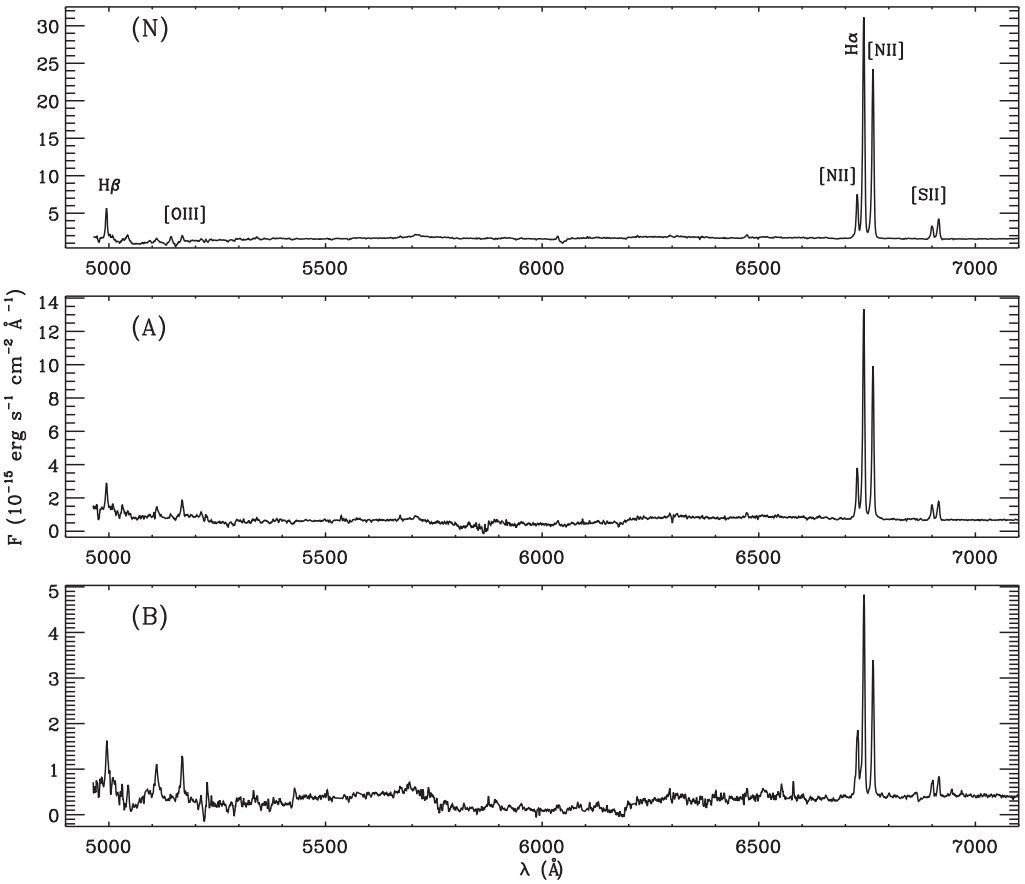

Figure 4. Examples of spectra for IRAS03056 obtained within a circular aperture of 0.45 arcsec for the nucleus (top), region A (middle) and B (bottom) labelled in Fig. 5. The strongest emission lines are identified in the nuclear spectrum.

these lines. The grey regions in all maps represent masked locations following the same criteria used for the flux maps, described in Section 3.3. The heliocentric systemic velocity of 8087 km s^{-1} was subtracted from the observed velocities. This value was derived by modelling of the H_α velocity field with a disc rotation model (see Section 4.4).

The velocity fields for all emission lines are similar, presenting blueshifts and redshifts of ∼40 km s^{-1} to the south and north, respectively. In addition, redshifts can be seen to the north-east at ∼2 arcsec from the nucleus, close to the border of the GMOS FoV (identified by a circle in the top right panel of Fig. 8).

The velocity dispersion map for H α presents values smaller than 100 km s^{-1} at most locations. The [N II] λ6583 σ map presents some higher values of 130 km s^{-1} to the north and surrounding the nucleus, while the highest σ values are seen for the [S II] λ6717 emitting gas, with values higher than 100 km s^{-1} observed at most locations.

4 DISCUSSION

4.1 Merger stage

IRASF23199+0123 (Hekatelyne et al. 2018) and IRAS16399−0937 (Sales et al. 2015) show clear evidence of an advanced merger stage, as tidal tails seen in *HST* images. On the other hand, IRAS03056 appears to be an isolated barred spiral galaxy, as our *HST* images (Figs 1 and 3) show no clear evidence of interaction.

Regarding the OH maser emission, IRAS23199+0123 and IRAS16399−0937 present $L_{OH} = 10^{2.35}$ and $L_{OH} = 10^{1.7}$ $L_\odot$, respectively (Baan et al. 1998; Darling & Giovanelli 2000). On the other hand, IRAS03056 shows a smaller luminosity $L_{OH} = 10^{1.3}$ $L_\odot$ (Baan et al. 2008), suggesting that these objects are at more advanced merger stages present stronger OH maser emission.

4.2 Gas excitation and BPT diagram

Baldwin, Phillips & Terlevich (1981, BP) proposed three diagnostic diagrams using emission-line ratios that allow us to distinguish gas excitation by AGN or starburst activity. These BPT diagrams are based on the following four line ratios: [N II] λ6583/H α, [O III] λ5007/H β, [S II] λ6717/H α, and [O I] λ6300/H α. The advantage of the BPT diagrams is that emission lines of each ratio are close in wavelength and thus the extinction effects can be neglected.

Fig. 9 presents the BPT diagrams for IRAS03056, where the x-axis shows the [N II] λ6583/H α, [S II] λ6717/H α, and [O I] λ6300/H α line ratios, respectively, and the y-axis shows the [OIII] λ5007/H β line ratios. The dotted curve corresponds to the line of

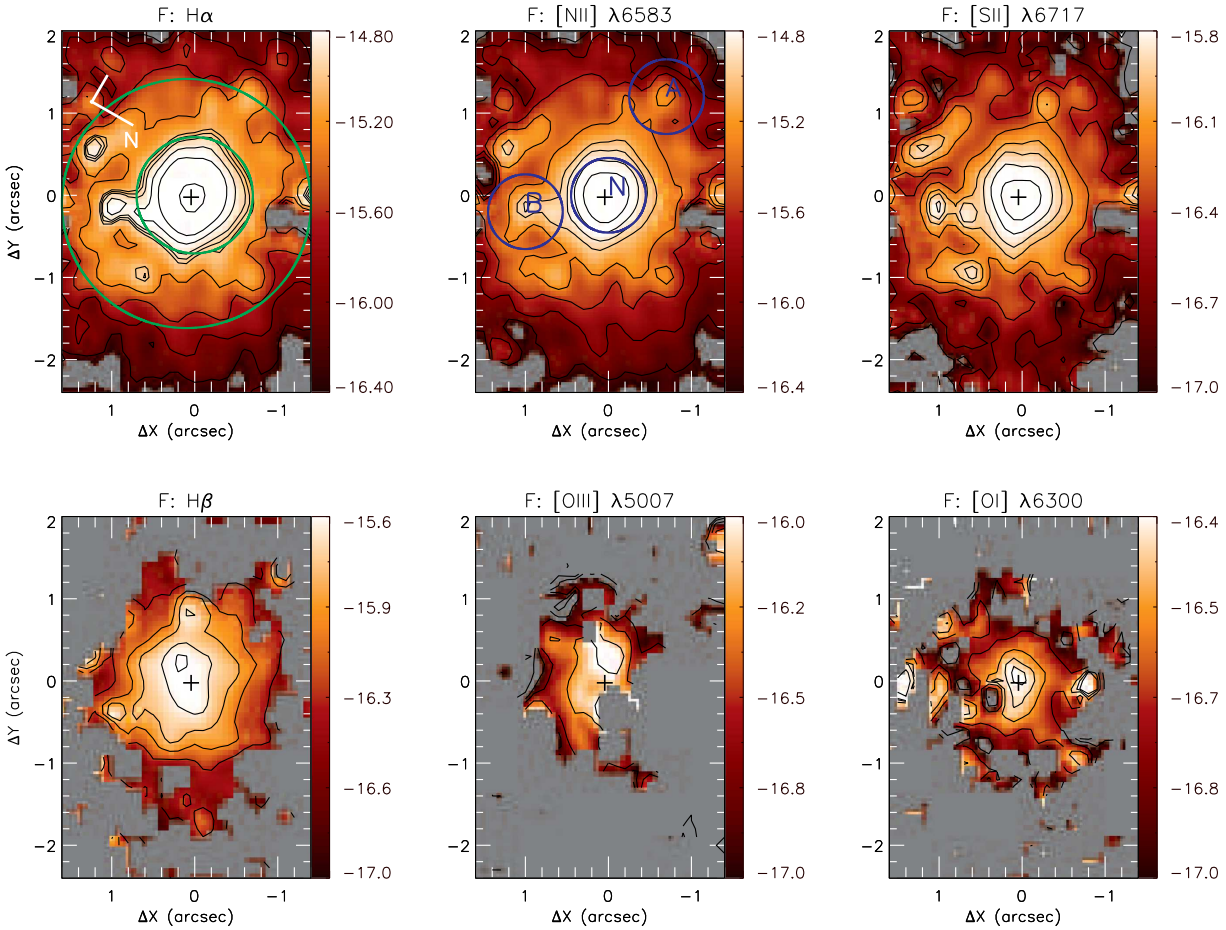

Figure 5. Top panels: flux maps for H α (left), [N II] λ6583 (centre), and [S II] λ6717 (left) emission lines of IRAS03056. The green circle delimits a ring where we have extracted spectra in order to characterize the star formation. The blue circles labelled as N, A, and B represent the circular regions where we extracted the spectra shown in Fig. 4. Bottom panels: flux maps for H β (left), [O III] λ5007 (centre), and [O I] λ6300 (right). The central crosses in all maps mark the position of the nucleus and grey regions represent masked locations, where the signal to noise was not high enough to obtain reliable fits of the emission-line profiles or locations with no line detection. The colour bars show the fluxes in logarithmic units of erg s^{-1} cm^{-2} per fiber and the grey regions represent masked locations where the signal-to-noise ratio was not high enough to obtain good fits of the emission-line profiles. These locations present flux uncertainty larger than 30 per cent.

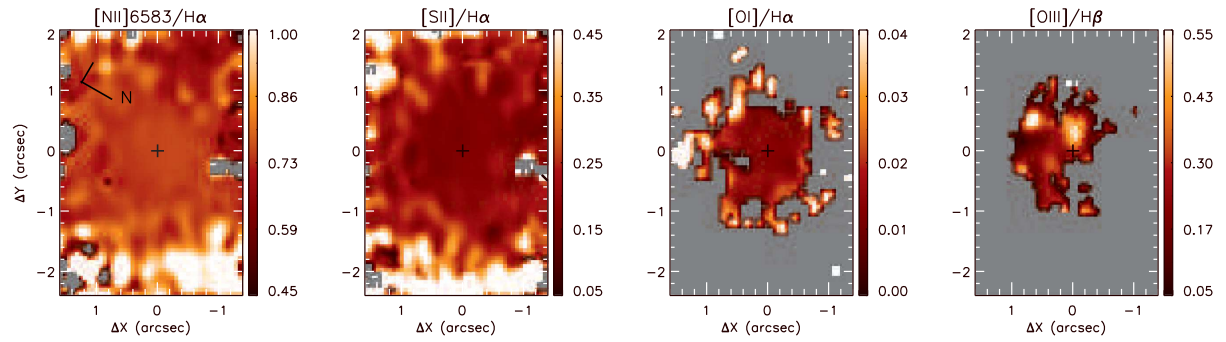

Figure 6. Emission-line ratio maps for IRAS03056. From left to right: [N II] λ6583/H α, [S II] λ6717/H α, [O I] λ6300/H α, and [O III] λ5007/H β flux-ratio maps. Grey regions correspond to locations where the signal-to-noise ratio was not high enough to measure one or both lines of each ratio map.

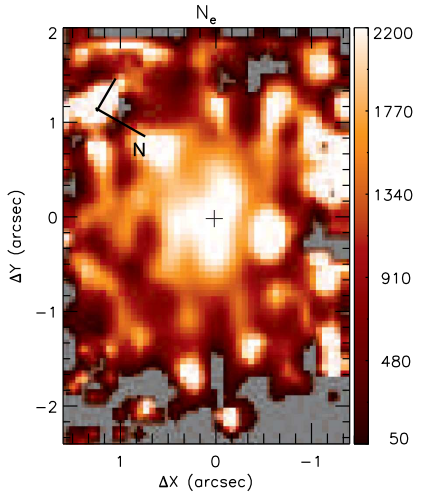

Figure 7. Electron density map for IRAS03056 obtained from the [S II] emission lines. The colour bar shows the N_e values in units of cm^{-3}.

Kewley et al. (2001) that delineates the region occupied by the AGN (to the right and above the line), while the solid line represents the revised Kauffmann criteria that separates pure star-forming galaxies (to the left and below the line) from AGN-HII composite objects (Kauffmann et al. 2003). Points located between the solid and dotted lines represent regions that have contributions to the gas excitation from both AGN and starbursts (Kewley et al. 2006). To construct the BPT diagrams shown in Fig. 9, we calculated the flux ratio for each spaxel, excluding flux measurements with uncertainties larger than 30 per cent.

The [N II] λ6583/H α versus [O III] λ5007/H β diagnostic diagram (left-hand panel of Fig. 9) shows all observed points in the region between the Kewley et al. (2001) and Kauffmann et al. (2003) lines, suggesting a contribution of both AGN and star formation to the gas excitation. The other two diagrams show observed line ratios below the Kewley et al. (2001) criteria for all locations.

In Fig. 9, the red asterisk corresponds to the nuclear position of the galaxy, as obtained from the measurements of the emission-line ratios within a circular aperture of 0.5 arcsec radius. The green diamond corresponds to the line ratios measured by Baan et al. (1998), which are similar to our nuclear values. These authors performed optical classification of 42 galaxies using spectroscopic data obtained at the Palomar Observatory and classified the nucleus of IRAS03056+2034 as starburst. However, their spectra were obtained with a long-slit of width of 2 arcsec and extractions of ∼6 arcsec, which corresponds to 1.1 × 2.8 kpc^2 at IRAS03056 and thus includes a large fraction of circumnuclear emission. The GMOS angular resolution is about three times better than that provided by the aperture used by Baan et al. (1998).

Although we were able to map the [O III] λ5007 emission only for the inner 1 arcsec region, we notice that the [O III] λ5007/H β line ratio values vary with the distance from the nucleus, where the highest values are seen. On the other hand, the [N II] λ6583/H α line ratio values do not change. This behaviour can be interpreted as an increasing contribution of an AGN to the production of the high excitation [O III] emission at the nucleus, which might be confirmed with higher resolution observations.

4.3 Star-forming regions

The H α flux map (Fig. 5) suggests the presence of a ring of circumnuclear star-forming regions located between 0.7 and 1.5 arcsec from the nucleus, as several unresolved knots of higher fluxes are seen at this location.

In order to characterize the star formation in the ring, we have extracted spectra from within a ring with an inner radius of 0.7 arcsec and an outer radius of 1.5 arcsec (identified as green circles in Fig. 5).

Using the H_α/H_β emission-line ratio and following Freitas et al. (2018), we obtained an extinction of $A_V \sim 0.2$ mag for the ring, which can be used to correct the observed line intensities. The H α luminosity of the ring (corrected by reddening) is $L_{H\alpha} \approx 1.79 \times 10^{41}$ erg s^{-1}, which can be used to estimate the mass of ionized gas, rate of ionizing photons, and star formation rate of the ring.

In order to estimate the mass of ionized gas, we used (e.g. Peterson 1997)

$$\frac{M_{\rm H\,II}}{\rm M_\odot} \approx 2.3 \times 10^5 \frac{L_{41}(H\alpha)}{n_3^2}, \quad (1)$$

where L_{41}(H α) is the H α luminosity in units of 10^{41} erg s^{-1} and n_3 is the electron density (N_e) in units of 10^3 cm^{-3}.

Using the ratio between the fluxes of the [S II] emission lines for the ring ([S II] λ 6717/λ 6731≈0.8) we obtain an electron density $N_e \approx 1385$ cm^{-3}, assuming an electron temperature $T_e = 10\,000$ K. This value is larger than those typically observed in star-forming regions (Díaz et al. 2007; Dors et al. 2008).

The estimated mass of ionized gas is $M_{\rm H\,II} = 2.1 \times 10^5$ M$_\odot$, which is similar to the values previously found for rings of circumnuclear star-forming regions (e.g. Riffel et al. 2016, 2009; Hennig et al. 2018).

We estimated the rate of ionizing photons (Q[H$^+$]) and SFR under the assumption of a continuous star formation regime. We derived Q[H$^+$] using Osterbrock (1989):

$$Q[{\rm H}^+] = \frac{\alpha_{\rm B} L_{\rm H_\alpha}}{\alpha_{\rm H_\alpha}^{\rm EFF} h \nu_{\rm H_\alpha}}, \quad (2)$$

where α_B is the hydrogen recombination coefficient to all energy levels above the ground level, $\alpha_{H_\alpha}^{EFF}$ is the effective recombination coefficient for H α, h is the Planck's constant, and ν_{H_α} is the frequency of the H α emission line. Using $\alpha_B = 2.59 \times 10^{13}$ cm^3 s^{-1} and $\alpha_{H_\alpha}^{EFF} = 1.17 \times 10^{-17}$ cm^3 s^{-1} (Osterbrock 1989) we obtain

$$\left(\frac{Q[{\rm H}^+]}{\rm s^{-1}}\right) = 1.03 \times 10^{12} \left(\frac{L_{\rm H_\alpha}}{\rm s^{-1}}\right). \quad (3)$$

The SFR was computed using the following relation (Kennicutt 1998):

$$\frac{\rm SFR}{\rm M_\odot\ yr^{-1}} = 7.9 \times 10^{-42} \frac{L_{\rm H_\alpha}}{\rm erg\ s^{-1}} \quad (4)$$

We found values of ionizing photons rate of log Q[H$^+$] = 53.3 and star formation rate of SFR = 1.4 M$_\odot$ yr^{-1}, which are in agreement with previous reported values for circumnuclear star-forming regions in nearby galaxies (e.g. Wold & Galliano 2006; Dors et al. 2008; Galliano & Alloin 2008; Riffel et al. 2009, 2016; Hekatelyne et al. 2018).

4.4 Gas kinematics

The gas velocity fields of IRAS03056 presented in Fig. 8 show a clear rotation pattern with blueshifts to the south and redshifts to

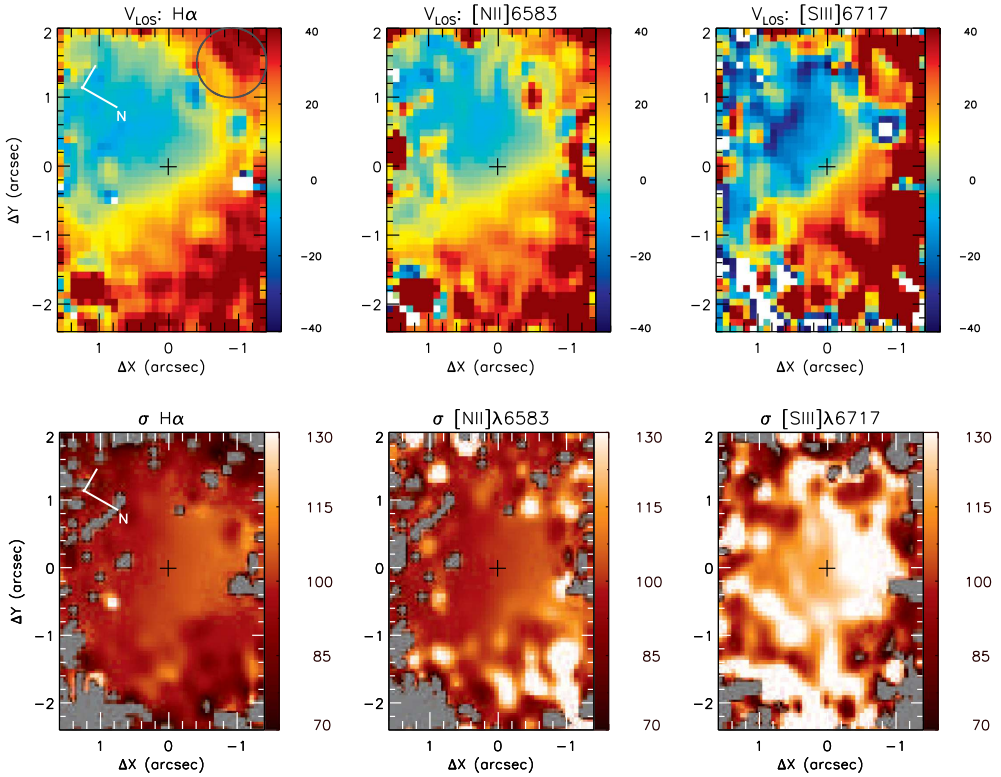

Figure 8. Top panels: line-of-sight velocity fields for the H α (left), [N II] λ6583 (centre), and [S II] λ6717 (right) emitting gas. The colour bars show the velocities in units of km s^{-1}, after the subtraction of the systemic velocity of the galaxy. Bottom panels: velocity dispersion maps for the H α (left), [N II] λ6583 (centre), and [S II] λ6717 (right) emission-lines, corrected for the instrumental broadening. The colour bars show the σ values in units of km s^{-1}. The central cross in all panels marks the position of the nucleus. The circle in the top right panel identifies the region where the inflows are detected.

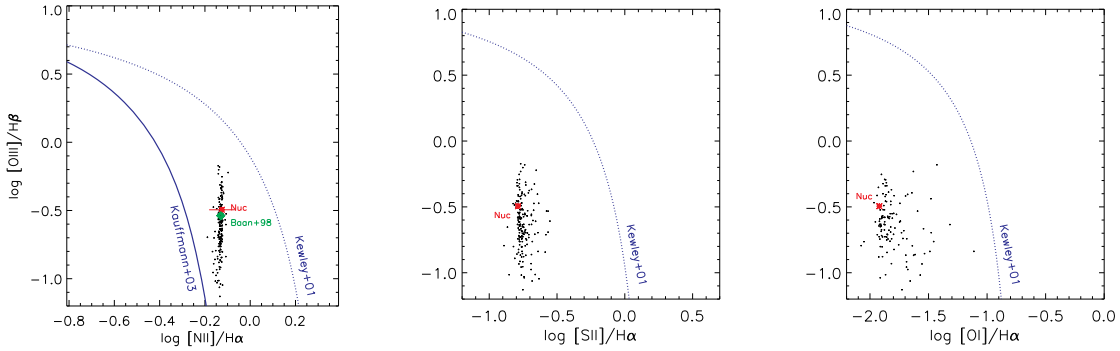

Figure 9. Left-hand panel: [N II] λ6583/H α versus [O III] λ5007/H$_\beta$ diagnostic diagram of IRAS03056. The dotted and dashed lines represent the Kewley and Kauffmann criteria, respectively. Central panel: [S II]/H$_\alpha$ versus [O III] λ5007/H$_\beta$ diagnostic diagram. Right-hand panel: [O III]/H$_\alpha$ versus [O III] λ5007/H$_\beta$ diagnostic diagram. The red asterisks correspond to the nucleus and the green diamond corresponds to Baan et al. (1998) measurements.

the north of the nucleus. In order to model these kinematics, we used a simple rotation model (van der Kruit & Allen 1978; Bertola et al. 1991), under the assumption that the gas moves in circular orbits in the plane of the galaxy, subjected to a central gravitational potential. In this model, the rotation velocity field is given by

$$V_{\rm mod}(R,\psi) = v_{\rm s} + \frac{A\,R\cos(\psi-\psi_0)\sin(i)\cos^p(i)}{\{R^2[\sin^2(\psi-\psi_0)+\cos^2(i)\cos^2(\psi-\psi_0)]+c_0{}^2\cos^2(i)\}^{\frac{p}{2}}}, \quad (5)$$

where R and ψ are the coordinates of each spaxel in the plane of the sky, $v_{\rm s}$ is the systemic velocity of the galaxy, A is the velocity amplitude, ψ_0 is the major axis position angle, i is the disc inclination in relation to the plane of the sky ($i = 0$ for a face-on disc), p is a model-fitting parameter (for $p = 1$ the rotation curve at large radii is asymptotically flat while for $p = 3/2$ the system has a finite mass), and c_0 is a concentration parameter, defined as the radius where the rotation curve reaches 70 per cent of the velocity amplitude.

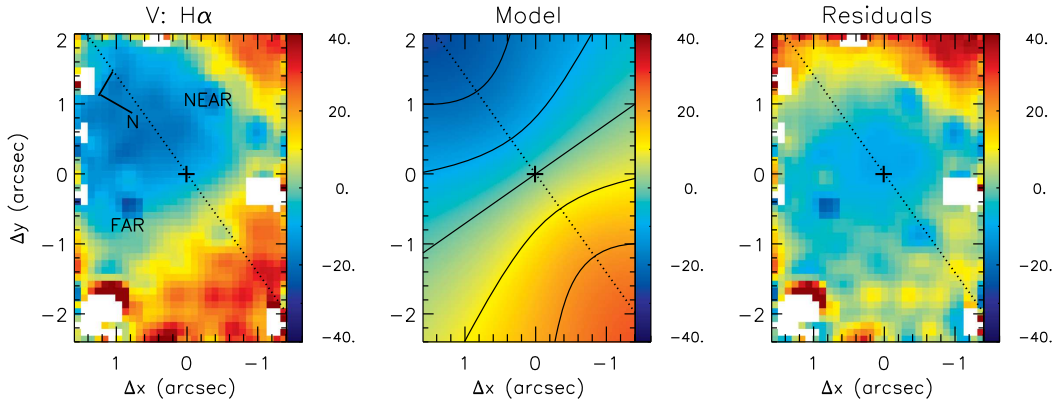

Figure 10. Observed H α velocity field (left), rotating disc model (middle), and residual map (right) obtained as the difference between the observed velocities and the model. The central cross marks the position of the nucleus, the white regions are masked locations where we were not able to fit the emission line profiles, and the dotted lines represent the orientation of the line of nodes.

The fit of this model provides information about the physical parameters of the system, such as the systemic velocity and orientation of the kinematic major axis. Moreover, the residual map (difference between the observed velocities and the model) allows us to detect deviations from pure rotation and identify non-circular motions.

We have chosen the velocity field of the H_α emission line to perform the fit, as this is the brightest line at most locations. We used the IDL[2] routine MPFITFUN (Markwardt 2009) in order to fit the observed velocity field with equation (5). During the fit, we excluded the redshifted region to the east of the nucleus, which clearly does not follow the rotation pattern.

The resulting best-fitting model is shown in the central panel of Fig. 10 and its parameters are $A = 40.5 \pm 5\,\mathrm{km\,s^{-1}}$, $v_s = 8\,087 \pm 20\,\mathrm{km\ s^{-1}}$ (corrected to the heliocentric rest frame), Ψ_0=156 $\pm$ 2°, c_0=1.″9 $\pm$ 0.″4, $i = 54° \pm 3°$. The obtained systemic velocity is about $140\,\mathrm{km\,s^{-1}}$ smaller than that quoted in the NASA/IPAC Extragalactic Database (NED).[3] The Ψ_0 value is consistent with the orientation of the apparent major axis of IRAS03056 as seen in the *HST* *i*-band image (Fig. 3), and is displaced by about 20° from the value quoted in NED (135°) as obtained from 2MASS K_S photometry (Skrutskie et al. 2006). The disc inclination is consistent with the value shown in NED, obtained from the 2MASS photometry.

Fig. 10 also presents the observed H_α velocity field in the left-hand panel and residual map in the right-hand panel. The velocity field presents redshifts to the north and blueshifts to the south, which are well described by the rotating-disc model, as indicated by the residual map, which shows values at most locations that are within $-10\,\mathrm{km\,s^{-1}}$ and $+10\,\mathrm{km\,s^{-1}}$, except for a region to the east of the nucleus (close to the border of the GMOS FoV, identified as a circle in Fig. 8), whose kinematics is not reproduced by our model. At the same location, the *HST* H α +[N II] narrow-band image (Fig. 3) shows a strip of enhanced emission, which may be due to a patchy spiral arm.

Considering the observed velocity fields of Fig. 8 and the orientation of the spiral arms seen in the bottom left panel of Fig. 3, we conclude that the north-east is the near side of the galaxy disc, while the south-west is the far side of the galaxy, under the assumption that the spiral arms seen in IRAS03056 are trailing. This assumption is supported by the fact that the vast majority of galaxies present spiral arms of the trailing type (e.g. Binney & Tremaine 2008). Thus, the excess of redshifts seen to the east of the nucleus can be interpreted as being due to gas-streaming motions along a nuclear spiral arm, under the assumption that the gas is located at the plane of the galaxy. Similar gas inflows along nuclear spiral arms have been previously observed in nearby active galaxies (e.g. Riffel et al. 2008; Müller Sánchez et al. 2009; van de Ven & Fathi 2010; Fathi et al. 2013; Riffel, Storchi-Bergmann & Winge 2013; Schnorr-Muller et al. 2014; Luo et al. 2016; Busch et al. 2017).

We can use these residual velocities observed along the nuclear spiral arm to estimate the mass inflow rate. Assuming that the gas is streaming towards the centre, we estimate the mass inflow rate as

$$M_{\rm in} = N_{\rm e} v \pi r^2 m_{\rm p} f, \tag{6}$$

where $N_{\rm e}$ is the electron density, v is the inflowing velocity, $m_{\rm p}$ is the proton mass, πr^2 is the area through which the gas is flowing, and f is the filling factor. One can estimate the filling factor using

$$L_{\rm H\alpha} \sim f N_{\rm e}^2 J_{\rm H\alpha}(T) V, \tag{7}$$

where $J_{\rm H\alpha}(V) = 3.534 \times 10^{-25}$ erg cm^{-3} s^{-1} (Osterbrock 1989) and $L_{\rm H_\alpha}$ is the H_α luminosity emitted by a region with volume V.

We assume that the volume of the inflowing gas region can be approximated by that of a cylinder with radius r and height h. Thus we obtain

$$\dot{M} = \frac{m_{\rm p} v L_{\rm H\alpha}}{J_{\rm H_\alpha}(T) N_{\rm e} h}. \tag{8}$$

In order to obtain $L_{\rm H\alpha}$ and $N_{\rm e}$, we measured the integrated flux of H α and the [S II] line ratio within the redshifted region seen in the residual map. The resulting H α flux is $F_{\rm H\alpha} \approx 1.87 \times 10^{-14}$ erg s^{-1} cm^{-2}, which corresponds to $L_{H\alpha} \approx 0.3 \times 10^{41}$ erg s^{-1} assuming the distance of 116 Mpc for IRAS03056. The mean [S II] λ 6717/λ 6731 ratio for the redshifted region is ~0.88. Using the *temden* IRAF task and adopting an electron temperature of $T_{\rm e}$= 10000K, we estimate $N_{\rm e} = 988 \pm 100$ cm^{-3}.

To estimate the mass inflow rate, we assume $h = 1$ kpc (1.8 arcsec), as the distance between the nucleus of the galaxy and the redshifted region (centre of the circle in Fig. 10), as measured directly from our maps. The mean inflow velocity is $v = 45\,\mathrm{km\ s^{-1}}$,

[2] http://www.harrisgeospatial.com/ProductsandSolutions/GeospatialProducts/IDL.aspx
[3] http://ned.ipac.caltech.edu

measured from the residual map and corrected for the inclination of the disc ($i = 54^\circ$, as derived from the rotation model). The resulting mass inflow rate obtained from equation (8) is $\dot{M} \approx 2.2 \times 10^{-3}\,M_\odot\,yr^{-1}$. The determination of the uncertainty in $\dot{M}$ is not an easy task. Considering the derived uncertainties for i and N_e, we obtain an uncertainty of $3.4 \times 10^{-4}\,M_\odot\,yr^{-1}$. The $\dot{M}$ value derived for IRAS03056 is consistent with those of previous estimates of mass inflow rates in ionized gas for nearby Seyfert galaxies (e.g. Storchi-Bergmann et al. 2007; Müller Sánchez et al. 2009; van de Ven & Fathi 2010; Schnorr-Muller et al. 2011, 2014, 2017a,b; Riffel, Storchi-Bergmann & Riffel 2014).

As speculation, we can estimate the dynamical time (Δt_{in}) it takes for the inflowing gas to move from 1 kpc (the adopted distance) to the nucleus. Assuming that the inflow has a constant velocity ($v = 45\,km\,s^{-1}$), we obtain $\Delta t_{in} \approx 2 \times 10^7$ yr, which is consistent with typical AGN lifetimes (e.g. Hopkins & Hernquist 2006).

5 CONCLUSIONS

We have analysed Gemini GMOS-IFU, VLA, and *HST* data of the galaxy IRAS03056+2034, which is known to host a source of OH megamaser emission. The GMOS observations cover the inner $1.7 \times 2.5\,kpc^2$ at a spatial resolution of 506 pc and velocity resolution of $90\,km\,s^{-1}$. Our main conclusions are

(i) The *HST* images reveal flocculent spiral arms, evidencing several knots of emission along them. Comparing the GMOS-IFU flux distributions with the [N II]+H_α *HST* image, we associate these knots with star-forming regions located within a ring with an inner radius of 337 pc and an outer radius of 786 pc.

(ii) The 6 and 20 cm VLA image shows compact radio emission at the nucleus of IRAS03056. No extended emission is observed.

(iii) Considering the H_α flux of the ring of circumnuclear star-forming regions, we derived that it has a mass of ionized gas of $2.1 \times 10^5\,M_\odot$, ionized photons rate of $\log Q[H^+] = 53.3$, and star formation rate of $1.4\,M_\odot\,yr^{-1}$.

(iv) Based on emission-line ratios, we conclude that the nucleus of IRAS03056 shows line ratios consistent with the presence of both an AGN and starburst activity.

(v) The electron density derived from the [S II] λ6719/λ6731 lines reaches values of up to $2200\,cm^{-3}$ in the nucleus of the galaxy.

(vi) The gas velocity fields show a rotation pattern with the south side of the disc approaching and the north side receding. The observed projected velocity amplitude is $\sim 40\,km\,s^{-1}$ and the kinematic major axis is oriented along $\Psi_0 = 156^\circ$. The gas kinematics is well reproduced by a rotating-disc model, assuming circular orbits in the galaxy plane.

(vii) Besides the rotating-disc component, the gas kinematics also reveal an excess of redshifts seen at 1.8 arcsec east of the nucleus with a velocity of $45\,km\,s^{-1}$. This component, which is possibly associated with a patchy nuclear spiral arm seen in the *HST* image, is located at the far side of the galaxy, and can be interpreted as inflows towards the nucleus. In this case, we estimate an ionized gas mass inflow rate of $2.2 \times 10^{-3}\,M_\odot\,yr^{-1}$, which is similar to the inflow rate observed in nearby Seyfert galaxies.

ACKNOWLEDGEMENTS

We thank the referee for his/her suggestions that improved the paper. This work is based on observations obtained at the Gemini Observatory, which is operated by the Association of Universities for Research in Astronomy, Inc., under a cooperative agreement with the NSF on behalf of the Gemini partnership: the National Science Foundation (United States), the Science and Technology Facilities Council (United Kingdom), the National Research Council (Canada), CONICYT (Chile), the Australian Research Council (Australia), Ministério da Ciência e Tecnologia (Brazil), and south-east CYT (Argentina). Support for programme *HST*-SNAP 11604 was provided by NASA through a grant from the Space Telescope Science Institute, which is operated by the Association of Universities for Research in Astronomy, Inc., under NASA contract NAS 5-26555. This research has made use of the NASA/IPAC Extragalactic Database (NED), which is operated by the Jet Propulsion Laboratory, California Institute of Technology, under contract with the National Aeronautics and Space Administration. We acknowledge the usage of the HyperLeda database (http://leda.univ-lyon1.fr). CH thanks CAPES for financial support. RAR and DAS acknowledge support from CNPq and FAPERGS.

REFERENCES

Allington-Smith J. et al., 2002, PASP, 114, 892
Baan W. A., Salzer J. J., LeWinter R. D., 1998, ApJ, 509, 633
Baan W. A., Henkel C., Loenen A. F., Baudry A., Wiklind T., 2008, A&A, 477, 747
Baldwin J. A., Phillips M. M., Terlevich R., 1981, PASP, 93, 5
Bertola F., Bettoni D., Danziger J., Sadler E., Sparke L., de Zeeuw T., 1991, ApJ, 373, 369
Berton M. et al., 2018, A&A, 614, 36,
Binney J., Tremaine S., 2008, Galactic Dynamics, 2nd edn. Princeton Univ. Press, Princeton, NJ
Bottinelli L., Gouguenheim L., Fouque P., Paturel G., 1990, A&A, 391, 488
Busch G., Eckart A., Valencia-S. M., Fazeli N., Scharwächter J., Combes F., García-Burillo S., 2017, A&A, 598, 55
Darling J., Giovanelli R., 2000, AJ, 119, 3003
Darling J., Giovanelli R., 2002, ApJ, 572, 810
Darling J., Giovanelli R., 2006, ApJ, 132, 2596
de Vaucouleurs G., de Vaucouleurs A., Corwin H. G., , Jr, Buta R. J., Paturel G., Fouque P., 1991, Third reference catalogue of bright galaxies, version 3.9. Springer, New York
Díaz Á. I., Terlevich E., Castellanos M., Hägele G. F., 2007, MNRAS, 382, 251
Dors O. L., Storchi-Bergmann T., Riffel R. A., Schmidt A. A., 2008, A&A, 482, 59
Fathi K. et al., 2013, ApJ, 770, 27
Freitas I. C. et al., 2018, MNRAS, 476, 2760
Galliano E., Alloin D., 2008, A&A, 487, 519
Haan S. et al., 2011, ApJS, 197, 27
Hekatelyne C. et al., 2018, MNRAS, 474, 5319
Henkel C., Guesten R., Baan W. A., 1987, A&A, 185, 14
Hennig M. G., , Riffel R. A., Dors O. L., Riffel R., Storchi-Bergmann T., Colina L., 2018, MNRAS, 477, 1086
Hook I., Jorgensen I., Allington-Smith J. R., Davies R. L., Metcalfe N., Murowinski R. G., Crampton D., 2004, PASP, 116, 425
Hoopes C. G., Walterbos R. A. M., Rand R. J., 1999, ApJ, 522, 669
Hopkins P. F., Hernquist L., 2006, ApJS, 166, 1
Kandalian R. A., 1996, Astrophys., 39, 237
Kauffmann G. et al., 2003, MNRAS, 346, 1055
Kennicutt R. C., 1998, ARA&A, 36, 189
Kewley L. J., Dopita M. A., Sutherland R. S., Heisler C. A., Trevena J., 2001, ApJ, 556, 121
Kewley L. J., Groves B., Kauffmann G., Heckman T., 2016, MNRAS, 372, 961
Lena D., 2014, ApJ, 806, 84
Liu L., Gao Y., Greve T. R., 2015, ApJ, 805, 31
Lo K. Y., 2005, ARA&A, 43, 625
Luo R., Hao L., Blanc G. A., Jogee S., van den Bosch R. C. E., Weinzirl T., 2016, ApJ, 823, 85

Markwardt C. B., 2009, in Bohlender D. A., Durand D., Dowler P., eds, ASP Conf. Ser. Vol. 411, Astronomical Data Analysis Software and Systems XVIII. Astron. Soc. Pac., San Francisco, p. 251
Osterbrock D. E., 1989, Astrophysics of Gaseous Nebulae and Active Galactic Nuclei. Univ. Science Books, California
Pacholczyk A. G., 1970, Radio Astrophysics. Freeman, San Francisco
Peterson B. M., 1997, An Introduction to Active Galactic Nuclei. Cambridge Univ. Press, Cambridge
Riffel R. A., 2010, Ap&SS, 327, 239
Riffel R. A., Storchi-Bergmann T., Winge C., McGregor P. J., Beck T., Schmitt H., 2008, MNRAS, 385, 1129
Riffel R. A., Storchi-Bergmann T., Dors O. L., Winge C., 2009, MNRAS, 393, 783
Riffel R. A., Storchi-Bergmann T., Winge C., 2013, MNRAS, 430, 2249
Riffel R. A., Storchi-Bergmann T., Riffel R., 2014, MNRAS, 451, 3587
Riffel R. A. et al., 2016, MNRAS, 461, 4192
Rossa J., Dettmar R.-J., 2000, A&A, 359, 433
Rossa J., Dettmar R.-J., 2003, A&A, 406, 505
Sales D. A. et al., 2015, ApJ, 799, 25
Sánchez F. M., Davies R. I., Genzel R., Tacconi L. J., Eisenhauer F., Hicks E. K. S., Friedrich S., Sternberg A., 2009, ApJ, 691, 749
Schnorr Muller A., Storchi-Bergmann T., Riffel R. A., Ferrari F., Steiner J. E., Axon D. J., Robinson A., 2011, MNRAS, 413, 149
Schnorr Muller A., Storchi-Bergmann T., Ferrari F., Nagas N. M., 2014, MNRAS, 438, 3332
Schnorr Muller A., Storchi-Bergmann T., Ferrari F., Nagar N. M., 2017a, MNRAS, 466, 4370
Schnorr Muller A., Storchi-Bergmann T., Ferrari F., Nagar N. M., Robinson A., Lena D., 2017b, MNRAS, 466, 4370
Skrutskie M. F. et al., 2006, AJ, 131, 1163
Storchi-Bergmann T., Dors O. L., Jr, Riffel R. A., Fathi K., Axon D. J., Robinson A., Marconi A., Ostlin G., 2007, ApJ, 670, 959
Theureau G., Hanski M. O., Coudreau N., Hallet N., Martin J.-M., 2007, A&A, 465, 71
Tody D., 1986, in Crawford D. L., ed., Proc. SPIE Conf. Ser. Vol. 627, Instrumentation in astronomy VI. SPIE, Bellingham, p. 733
Tody D., 1993, in Hanisch R. J., Brissenden R. J. V., Barnes J., eds, ASP Conf. Ser. Vol. 32, IRAF in the Nineties in Astronomical Data Analysis Software and Systems II. Astron. Soc. Pac., San Francisco, p. 173
Ulvestad J. S., Antonucci R. R. J., Barvainis R., 2005, ApJ, 621, 123
van de Ven G., Fathi K., 2010, ApJ, 723, 767
van der Kruit P. C., Allen R. J., 1978, ARA&A, 16, 103
van Dokkum P. G., 2001, PASP, 113, 1420
Wold M., Galliano E., 2006, MNRAS, 369, 47
Yuan T.-T., Kewley L. J., Sanders D. B., 2010, ApJ, 709, 884

This paper has been typeset from a TEX/LATEX file prepared by the author.

6 CONCLUSÕES

Nessa tese foram apresentados resultados obtidos a partir de dados coletados com os telescópios Gemini, VLA e HST das galáxias IRASF23199+0123 e IRAS03056+2034 referentes à dinâmica e excitação do gás em suas regiões centrais. Nossos principais objetivos foram identificar o mecanismo central de ionização do gás nesses objetos (AGN e/ou Starburst) e propor um cenário que justifique a emissão megamaser.

- **Emissão estendida do gás e estado de fusão:** Os dados de espectroscopia IFU óptica mostraram que as duas galáxias apresentam emissão estendida em todo o campo de visão GMOS-IFU. Além disso, no caso de IRAS23199, foi possível mostrar com dados HST que IRASF23199+0123 é na verdade um par de galáxias em interação e não apenas uma galáxia isolada conforme acreditava-se anteriormente. Por outro lado, imagem obtidas com o HST mostram que IRAS03056+2034 é uma galáxia espiral com braços floculentos e que não apresenta evidências morfológicas de interação.

- **Formação estelar:** Para IRAS23199, através da comparação entre as imagens obtidas com o HST e a distribuição de fluxos das linhas de emissão obtidas com espectroscopia IFU foi possível notar que as distribuições são similares porém o mapa do fluxo em Hα revelou a presença de três regiões de formação estelar extranucleares para as quais foram estimados valores para algumas propriedades físicas. No caso de IRAS03056, as imagens obtidas com o HST revelaram diversas regiões de formação estelar ao longo dos braços espirais. A comparação entre essas imagens e os mapas de fluxos GMOS-IFU permitiu a identificação de um anel de formação estelar circumnuclear para os quais também foram estimadas algumas propriedades físicas.

- **A natureza da emissão nuclear:** Um dos principais resultados obtidos sobre IRAS23199 foi a identificação de um núcleo Seyfert 1, através da detecção de uma componente larga (FWHM $\approx$ 2200 km/s) de duplo pico não resolvida na linha de emissão de Hα proveniente da BLR. Além disso, o diagrama WHAN mostra que o AGN central tem um papel importante na excitação do gás. Por outro lado, com base nos diagramas de diagnóstico, cálculo de índice espectral e temperatura de brilho, concluímos que a excitação do gás em IRAS03056 é devido a um Starburst e também à presença de um AGN envolto em poeira.

- **Cinemática do gás:** Foi realizado um ajuste de modelo de disco em rotação aos campos de velocidade observados de ambas galáxias. Com isso, foi possível identificar peculiaridades que destoam de um padrão de rotação usual. No caso de

IRAS23199, o mapa de velocidades apresenta um padrão de rotação bastante perturbado. O mapa de resíduos obtido através da diferença entre o campo de velocidades observado e o modelo sugeriu a presença de movimentos não circulares que se devem possivelmente a presença de outflows provenientes do núcleo ao longo das direções norte e sul e inflows na vizinhança do núcleo.

Para IRAS03056 também foi realizado o ajuste de um modelo de disco em rotação com o lado sul do disco se aproximando e o lado norte se afastando. Embora a cinemática do gás seja bem reproduzida na maior parte do campo, o mapa de resíduos revela um excesso de redshift no lado próximo que parece estar associado a um braço espiral descontínuo observado na imagem em grande escala obtida com o HST. Com base nessa evidência, sugerimos que esse excesso esteja associado a inflows em direção ao núcleo.

- **A emissão megamaser:** No caso de IRAS23199 foi possível detectar duas fontes de emissão de maser de OH associadas ao membro leste que compõe o par. A detecção foi realizada na galáxia que tem um AGN e além disso as fontes maser foram observadas nas regiões de maior dispersão de velocidades e razão de linhas mais intensa. Dessa forma, sugerimos que a emissão maser está associada com choques causados por outflows provenientes do AGN.

  Já no caso de IRAS03056 não foi possível fornecer a localização do maser, mas podemos concluir que há a presença de um AGN obscurecido e atividade starburst que poderiam ocasionar o pumping necessário para produção do maser.

A análise multicomprimento de onda das duas galáxias estudadas nessa tese contribuem para a compreensão do mecanismo de ionização desse tipo de objeto e fornece informações sobre os processos de formação estelar e de evolução de galáxias, uma vez que os processos de ignição da fase ativa de uma galáxia, através da alimentação do buraco negro central não são totalmente compreendidos. Nesse sentido, cabe ressaltar ainda a contribuição desta tese para compreensão dos mecanismos que favorecem a emissão maser e que no caso destes dois objetos parece estar relacionada com a presença de um AGN.

6.1 PERSPECTIVAS

Conforme mencionado anteriormente, estão sendo analisados os dados de IRAS11506-3851 e os resultados serão publicados nos próximos meses. Além disso, foi realizada uma proposta de tempo observacional que foi aprovada (Projetos: GS-2017B-Q-37 e GN-2017B-Q-38) com o objetivo de analisar dados GMOS-IFU de outras galáxias da amos-

tra desse projeto, para as quais temos dados complementares com outros instrumentos. Foram ainda aprovadas as propostas observacionais para 2018B para novos objetos da amostra (Projeto: GS-2018B-Q-203).

REFERÊNCIAS BIBLIOGRÁFICAS

ALLINGTON-SMITH, J. et al. Integral Field Spectroscopy with the Gemini Multiobject Spectrograph. I. Design, Construction, and Testing. **The Publications of the Astronomical Society of the Pacific**, v. 114, p. 892–912, ago. 2002.

ANTONUCCI, R. Unified models for active galactic nuclei and quasars. **Annual review of astronomy and astrophysics**, v. 31, p. 473–521, 1993.

ARGON, A. L. et al. The IC 133 Water Vapor Maser in the Galaxy M33: A Geometric Distance. **The Astrophysical Journal**, v. 615, p. 702–719, nov. 2004.

BAAN, W. A. Powerful extragalactic masers. **Nature**, v. 315, p. 26–31, maio 1985.

BAAN, W. A.; HASCHICK, A. D.; HENKEL, C. Molecular outflows in powerful OH megamasers. **Astrophysical Journal**, v. 346, p. 680–689, nov. 1989.

BAAN, W. A.; HASCHICK, A. D.; SCHMELZ, J. T. The fourth OH megamaser - Markarian 273. **Astrophysical Journal Letters**, v. 298, p. L51–L54, nov. 1985.

BAAN, W. A.; SALZER, J. J.; LEWINTER, R. D. Optical Classification of Megamaser Galaxies. **The Astronomical Journal**, v. 509, p. 633–645, dez. 1998.

BAAN, W. A.; WOOD, P. A. D.; HASCHICK, A. D. Broad hydroxyl emission in IC 4553. **Astrophysical Journal Letters**, v. 260, p. L49–L52, set. 1982.

BALDWIN, J. A.; PHILLIPS, M. M.; TERLEVICH, R. Classification parameters for the emission-line spectra of extragalactic objects. **The Publications of the Astronomical Society of the Pacific**, v. 93, p. 5–19, fev. 1981.

BERTOLA, F. et al. Testing the gravitational field in elliptical galaxies - NGC 5077. **Astrophysical Journal**, v. 373, p. 369–390, jun. 1991.

BOTTINELLI, L. et al. MRK 273 - A new OH megamaser. **Astronomy and Astrophysics**, v. 151, p. L7–L9, out. 1985.

____. An extragalactic data base. II - The HI data. **Astronomy and Astrophysics Supplement Series**, v. 82, p. 391–488, mar. 1990.

BOURNAUD, F. et al. ISM properties in hydrodynamic galaxy simulations: turbulence cascades, cloud formation, role of gravity and feedback. **Monthly Notices of the Royal Astronomical Society**, v. 409, p. 1088–1099, dez. 2010.

BRAATZ, J. A.; GUGLIUCCI, N. E. The Discovery of Water Maser Emission from Eight Nearby Galaxies. , v. 678, p. 96–101, maio 2008.

BRUNTHALER, A. et al. Towards proper motions in the Local Group. In: **Astronomische Gesellschaft Abstract Series**. [S.l.: s.n.], 2002. (Astronomische Gesellschaft Abstract Series, v. 19), p. 66–66.

CHEUNG, A. C. et al. Detection of Water in Interstellar Regions by its Microwave Radiation. **Nature**, v. 221, p. 626–628, fev. 1969.

CHURCHWELL, E. et al. Detection of H2O maser emission in the Galaxy M 33. **Astronomy and Astrophysics**, v. 54, p. 969–971, fev. 1977.

CLAUSSEN, M. J.; HEILIGMAN, G. M.; LO, K. Y. Water-vapor maser emission from galactic nuclei. **Nature**, v. 310, p. 298–300, jul. 1984.

CLAUSSEN, M. J.; LO, K.-Y. Circumnuclear water vapor masers in active galaxies. **The Astrophysical Journal**, v. 308, p. 592–599, set. 1986.

CONWAY, J. E.; CORNWELL, T. J.; WILKINSON, P. N. Multi-Frequency Synthesis - a New Technique in Radio Interferometric Imaging. **Monthly Notices of the Royal Astronomical Society**, v. 246, p. 490, out. 1990.

COUTO, G. S.; STORCHI-BERGMANN, T.; SCHNORR-MÜLLER, A. Gas rotation, shocks and outflow within the inner 3 kpc of the radio galaxy 3C 33. **Monthly Notices of the Royal Astronomical Society**, v. 469, p. 1573–1586, ago. 2017.

DARLING, J.; GIOVANELLI, R. A Search for OH Megamasers at Z0.1. II. Further Results. **The Astronomical Journal**, v. 121, p. 1278–1293, mar. 2001.

____. A Search for OH Megamasers at z0.1. III. The Complete Survey. **The Astronomical Journal**, v. 124, p. 100–126, jul. 2002.

____. Optical Spectral Classification of Major Mergers: OH Megamaser Hosts versus Non-masing (Ultra)Luminous Infrared Galaxies. **The Astronomical Journal**, v. 132, p. 2596–2617, dez. 2006.

DIAMOND, P. J. et al. Global VLBI Observations of the Compact OH Megamaser Emission from III ZW 35 and IRAS 17208-0014. **The Astrophysical Journal**, v. 511, p. 178–184, jan. 1999.

DOKKUM, P. G. van. Cosmic-Ray Rejection by Laplacian Edge Detection. **The Publications of the Astronomical Society of the Pacific**, v. 113, p. 1420–1427, nov. 2001.

FERNANDES, R. C. et al. Alternative diagnostic diagrams and the 'forgotten' population of weak line galaxies in the SDSS. **Monthly Notices of the Royal Astronomical Society**, v. 403, p. 1036–1053, abr. 2010.

GARDNER, F. F.; WHITEOAK, J. B. The groundstate OH spectrum of the galaxy NGC 253. **Monthly Notices of the Royal Astronomical Society**, v. 173, p. 77P–82P, dez. 1975.

____. The Circinus galaxy - A second case of intense nuclear H2O emission. **Monthly Notices of the Royal Astronomical Society**, v. 201, p. 13P–15P, out. 1982.

GENZEL, R. et al. Structure and kinematics of H2O sources in clusters of newly-formed OB stars. **Astronomy and Astrophysics**, v. 66, p. 13–29, maio 1978.

HEKATELYNE, C. et al. Gemini IFU, VLA, and HST observations of the OH megamaser galaxy IRAS F23199+0123: the hidden monster and its outflow. **Monthly Notices of the Royal Astronomical Society**, v. 474, p. 5319–5329, mar. 2018.

____. Star formation and gas inflows in the OH Megamaser galaxy IRAS03056+2034. **ArXiv e-prints**, jun. 2018.

HERNQUIST, L.; MIHOS, J. C. Excitation of activity in galaxies by minor mergers. **The Astrophysical Journal**, v. 448, p. 41, 1995.

HERRNSTEIN, J. R. et al. Polarimetric Observations of the Masers in NGC 4258: An Upper Limit on the Large-Scale Magnetic Field 0.2 Parsecs from the Central Engine. **The Astrophysical Journal**, v. 508, p. 243–247, nov. 1998.

____. A geometric distance to the galaxy NGC4258 from orbital motions in a nuclear gas disk. **Nature**, v. 400, p. 539–541, ago. 1999.

HO, L. C. “Low-State” Black Hole Accretion in Nearby Galaxies. **Astrophysics and Space Science**, v. 300, p. 219–225, nov. 2005.

HOOK, I. M. et al. The Gemini-North Multi-Object Spectrograph: Performance in Imaging, Long-Slit, and Multi-Object Spectroscopic Modes. **The Publications of the Astronomical Society of the Pacific**.

HUCHTMEIER, W. K. et al. Further detections of H2O-emission from external galaxies. **Astronomy and Astrophysics**, v. 64, p. L21–L24, mar. 1978.

KAUFFMANN, G. et al. The host galaxies of active galactic nuclei. **Monthly Notices of the Royal Astronomical Society**, v. 346, p. 1055–1077, dez. 2003.

KEWLEY, L. J. et al. Theoretical Modeling of Starburst Galaxies. **The Astrophysical Journal**, v. 556, p. 121–140, jul. 2001.

KIM, S. et al. Antarctic Submillimeter Telescope and Remote Observatory Observations of CO J=7–6 and J=4–3 Emission toward the Galactic Center Region. **The Astrophysical Journal**, v. 580, p. 896–903, dez. 2002.

KLÖCKNER, H.-R.; BAAN, W. A. An embedded circumnuclear disk in Mrk 273. **Astronomy and Astrophysics**, v. 419, p. 887–896, jun. 2004.

KLÖCKNER, H.-R.; BAAN, W. A.; GARRETT, M. A. Investigation of the obscuring circumnuclear torus in the active galaxy Mrk231. **Nature**, v. 421, p. 821–823, fev. 2003.

KRUIT, P. C. van der; ALLEN, R. J. The kinematics of spiral and irregular galaxies. **Annual review of astronomy and astrophysics**, v. 16, p. 103–139, 1978.

LI, Y. et al. Formation of z 6 quasars from hierarchical galaxy mergers. **The Astrophysical Journal**, v. 665, p. 187, 2007.

LONSDALE, C. J. et al. Symmetric Parsec-scale OH Megamaser Structures in ARP 220. **The Astrophysical Journal**, v. 493, p. L13–L16, jan. 1998.

____. VLBI Imaging of Luminous Infrared Galaxies: Active Galactic Nucleus Cores in Markarian 231, UGC 5101, and NGC 7469. , v. 592, p. 804–818, ago. 2003.

LYNDEN-BELL, D. Galactic Nuclei as Collapsed Old Quasars. **Nature**, v. 223, p. 690–694, ago. 1969.

MARKWARDT, C. B. Non-linear Least-squares Fitting in IDL with MPFIT. In: BOHLENDER, D. A.; DURAND, D.; DOWLER, P. (Ed.). **Astronomical Data Analysis Software and Systems XVIII**. [S.l.: s.n.], 2009. (Astronomical Society of the Pacific Conference Series, v. 411), p. 251.

MCMULLIN, J. P. et al. CASA Architecture and Applications. In: Shaw, R. A.; Hill, F.; Bell, D. J. (Ed.). **Astronomical Data Analysis Software and Systems XVI**. [S.l.: s.n.], 2007. (Astronomical Society of the Pacific Conference Series, v. 376), p. 127.

MIHOS, J. C.; HERNQUIST, L. Gasdynamics and Starbursts in Major Mergers. **The Astrophysical Journal**, v. 464, p. 641, jun. 1996.

MIYOSHI, M. Development of VLBI maser astronomy. **Astronomical Herald**, v. 89, p. 11–16, 1996.

PIHLSTRÖM, Y. M. et al. High-Resolution Imaging of the OH Megamaser Emission in IRAS 12032+1707 and IRAS 14070+0525. **The Astrophysical Journal**, v. 618, p. 705–711, jan. 2005.

RAU, U.; CORNWELL, T. J. A multi-scale multi-frequency deconvolution algorithm for synthesis imaging in radio interferometry. **Astronomy Astrophysics**, v. 532, p. A71, ago. 2011.

REID, M. J. The magnetic field of the Milky Way. **Highlights of Astronomy**, v. 12, p. 716–718, 2002.

RIFFEL, R. A. profit: a new alternative for emission-line profile fitting. **Astrophysics and Space Science**, v. 327, p. 239–244, jun. 2010.

SALPETER, E. E. Accretion of Interstellar Matter by Massive Objects. **The Astrophysical Journal**, v. 140, p. 796–800, ago. 1964.

SANDERS, D. B.; MIRABEL, I. F. Luminous Infrared Galaxies. **Annual Review of Astronomy and Astrophysics**, v. 34, p. 749, 1996.

SANDERS, D. B. et al. Ultraluminous infrared galaxies. In: Lonsdale Persson, C. J. (Ed.). **NASA Conference Publication**. [S.l.: s.n.], 1987. (NASA Conference Publication, v. 2466).

SANTOS, P. M. D.; LEPINE, J. R. D. Detection of strong H2O emission from galaxy NGC4945. **Nature**, v. 278, p. 34, mar. 1979.

SCHMELZ, J. T. et al. An Arecibo survey for extragalactic hydroxyl absorption. I - Presentation of results. **Astronomical Journal**, v. 92, p. 1291–1302, dez. 1986.

SCHWAB, F. R. Relaxing the isoplanatism assumption in self-calibration; applications to low-frequency radio interferometry. **Astronomical Journa**, v. 89, p. 1076–1081, jul. 1984.

SNYDER, L. E. et al. Microwave Detection of Interstellar Formaldehyde. **Physical Review Letters**, v. 22, p. 679–681, mar. 1969.

SOIFER, B. T. et al. The IRAS bright galaxy sample. II - The sample and luminosity function. **The Astrophysical Journal**, v. 320, p. 238–257, set. 1987.

SWINGS, P.; ROSENFELD, L. Considerations Regarding Interstellar Molecules. **The Astrophysical Journal**, v. 86, p. 483–486, nov. 1937.

TOOMRE, A.; TOOMRE, J. Galactic Bridges and Tails. **The Astrophysical Journal**, v. 178, p. 623–666, 1972.

VAUCOULEURS, G. de et al. **Third Reference Catalogue of Bright Galaxies, version3.9**. New York: [s.n.], 1991.

WEINREB, S. et al. Radio Observations of OH in the Interstellar Medium. **Nature**, v. 200, p. 829–831, nov. 1963.

WHITEOAK, J. B.; GARDNER, F. F. A 5-GHz Survey of the Galactic Center Region with a Resolution of 4 arc min. **Astrophysical Letters**, v. 13, p. 205, abr. 1973.

WOODS, D. F.; GELLER, M. J. Minor galaxy interactions: Star formation rates and galaxy properties. **The Astrophysical Journal**, v. 134, p. 527–540, 2007.

APÊNDICE A – PARTICIPAÇÃO EM OUTROS TRABALHOS

No início do doutorado a doutoranda reduziu os dados obtidos com o instrumento GMOS-IFU da galáxia NGC5643. Os resultados originaram o artigo em anexo.

Publications of the Astronomical Society of Australia (PASA)
doi: 10.1017/pas.2018.xxx.

Nuclear outflows in the Seyfert 2 galaxy NGC 5643

Rogemar A. Riffel[1], C. Hekatelyne[1], Izabel C. Freitas[1,2]
[1]Universidade Federal de Santa Maria, Departamento de Física, CCNE, 97105-900, Santa Maria, RS, Brazil
[2]Universidade Federal de Santa Maria, Colégio Politécnico, 97105-900, Santa Maria, RS, Brazil

Abstract

We use Gemini Multi-Object Spectrograph (GMOS) Integral Field Unit (IFU) observations of the inner $285\times400\,\mathrm{pc}^2$ region of the Seyfert 2 galaxy NGC 5643 to map the [S III]λ9069 emission-line flux distribution and kinematics, as well as the stellar kinematics, derived by fitting the Ca II$\lambda\lambda\lambda$8498,8542,8662 triplet, at a spatial resolution of 45 pc. The stellar velocity field shows regular rotation, with a projected velocity of 100 $\mathrm{km\,s^{-1}}$ and kinematic major axis along Position Angle $PA = -36°$. A ring of low stellar velocity dispersion values ($\sim$70 $\mathrm{km\,s^{-1}}$), attributed to young/intermediate age stellar populations, is seen surrounding the nucleus with radius of 50 pc. We found that the [S III] flux distribution shows an elongated structure along the east-west direction and its kinematics is dominated by outflows within a bi-cone at an ionized gas outflow rate of $0.3\,\mathrm{M_\odot\,yr^{-1}}$. In addition, velocity slices across the [S III]λ9069 emission-line reveal a kinematic component attributed to rotation of gas in the plane of the galaxy.

Keywords: galaxies: active – galaxies: Seyfert – galaxies: kinematics – galaxies: individual (NGC 5643)

1 INTRODUCTION

The unified model of Active Galactic Nuclei (AGN) postulates the existence of ionization bi-cones, delineating the Narrow Line Region (NLR; Antonucci, 1993; Urry & Padovani, 1995). Within the bi-cone, winds from the accretion disk are expected to be observed. Indeed these conical shaped structures were seen in early ground based images (Wilson & Tsvetanov, 1994). However, later, [O III]λ5007 high-resolution narrow-band images obtained with the Hubble Space Telescope (HST) showed that the conical morphology is not as common as previously thought (e.g. Schmitt et al., 2003). Fischer et al. (2013) used HST long-slit observations of a sample of 48 AGN to map the [O III] kinematics and found that only 35 % of the galaxies with extended NLR show outflows. Integral Field Spectroscopy (IFS) on 8-10 m telescopes is a powerful tool to map the central region of active galaxies, as they provide the spatial and spectral resolutions and spatial coverage, needed to properly map the NLR kinematics and geometry (e.g. Riffel et al., 2006; Barbosa et al., 2009; Riffel et al., 2013, 2015; Medling et al., 2015; Lena et al., 2016; Fischer et al., 2017; Thomas et al., 2017; Wylezalek et al., 2017; Freitas et al., 2018).

We present near-infrared (near-IR) IFS of the inner $5''\times7''$ region of the Seyfert 2 galaxy NGC 5643, obtained with the Gemini Multi-Object Spectrograph (GMOS). NGC 5643 is a widely studied spiral galaxy, morphologically classified as SBc and located at a distance of 11.8 Mpc, for which $1''$ corresponds to 57 pc at the galaxy (de Vaucouleurs et al., 1976; Fischer et al., 2013). It harbors a Seyfert 2 nucleus and its optical spectra shows high ionization lines (Sandage, 1978; Phillips et al., 1983).

Ground-based [O III]λ5007 and Hα+[N II]$\lambda\lambda$6548, 84 narrow-band images of NGC 5643 show an elongated structure with size of $30''$ (1.9 kpc) aligned along the east-west direction, with higher excitation gas observed to the east of the nucleus (Schmitt et al., 1994). High resolution narrow-band images obtained with the HST have confirmed the presence of higher excitation gas to the east of the nucleus and reveal a well defined one-sided cone with vertex at the location of the continuum emission peak and oriented to the east (Simpson et al., 1997). Such structure is also detected in soft X-ray images (Bianchi et al., 2006). Fischer et al. (2013) used HST narrow-band images and long-slit spectroscopy of the NLR of NGC 5643 and found that the [O III] kinematics is consistent with outflows within a cone oriented along Position Angle $PA = 80°$, with inclination of 25° and maximum opening angle of 55°.

Near-IR IFS of the inner $8''\times8''$ region of NGC 5643, obtained with the Very Large Telescope (VLT), reveals that the Brγ emission-line shows a similar flux distribution to the optical lines, while the $H_2 1-0\,S(1)$ flux

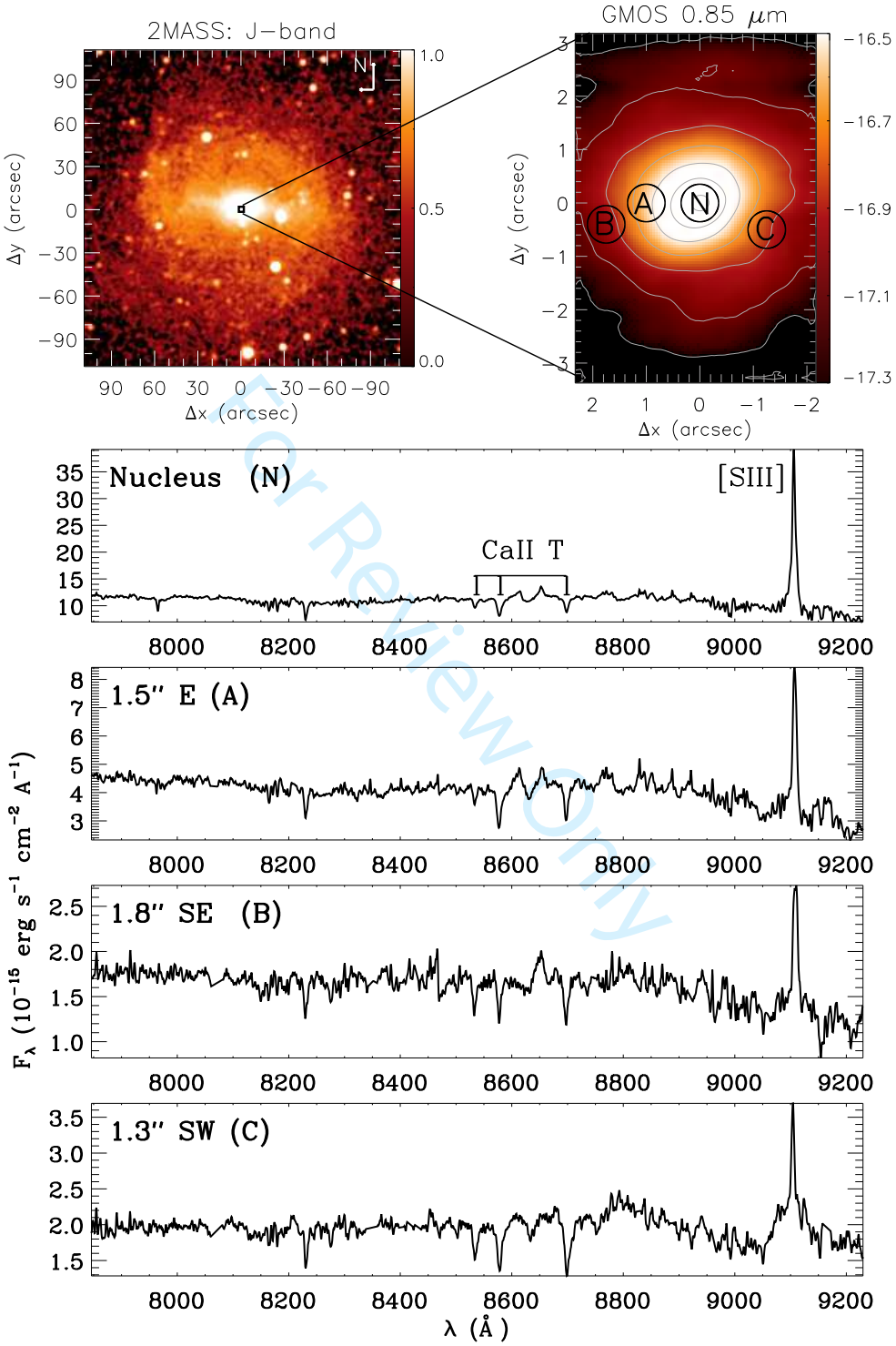

Figure 1. Top panels – Left: Large scale J-band image of NGC 5643 from 2MASS (Jarrett et al., 2003). The color bar shows the flux in arbitrary units. Right: 0.85 μm continuum image obtained from the GMOS datacube, by averaging the fluxes within a 300 Å spectral range. The color bar shows the fluxes in logarithmic units of erg s^{-1} cm^{-2} Å^{-1} spaxel^{-1}. Bottom panels show the spectra extracted within the circular apertures of 0.7″ diameter, identified in the top-right panel.

distribution presents two clear spiral arms one to the northwest and another to the southeast (Davies et al., 2014; Menezes et al., 2015). The H_2 velocity field shows kinematic structures associated the spiral arms seen in the H_2 flux distribution, and consistent with gas flows towards the nucleus along a bar. To the northeast, the H_2 kinematics is consistent with outflows of molecular gas excited around the edge of the ionization cone. These authors found also that the Brγ emission traces the ionization cone with velocities of up to 150 km s^{-1}. The stellar velocity field of the central region of NGC 5643, derived by fitting the K-band CO absorption band heads, shows regular rotation with the line of nodes oriented along $PA = -39°$ and projected velocity amplitude of $\sim$100 km s^{-1} (Hicks et al., 2013; Davies et al., 2014).

This paper is organized as follows. Section 2 presents the observations and data treatment, Section 3 shows the two-dimensional maps for the emission-line flux distribution and kinematics, as well as for the stellar kinematics. These results are discussed in Section 4 and the conclusions of this work are presented in Section 5.

2 OBSERVATIONS AND DATA REDUCTION

We use Gemini Observatory archival data of NGC 5643 obtained with the Gemini Multi-Object Spectrograph Integral Field Unit (GMOS IFU; Allington-Smith et al., 2002; Hook et al., 2004) on the Gemini South Telescope. The observations were done in the two-slit mode, resulting in a Field of View (FoV) of 5″×7″, centered at the nucleus of the galaxy. The R400 grating in combination to the G5325 filter, resulting in a spectral range 7750 – 9950 Å. The total on source exposure time was 65 min, divided in three individual exposures of 22 min each.

The data reduction followed the standard procedures (e.g. Lena, 2014; Brum et al., 2017) using the GEMINI package in IRAF software (Tody, 1986, 1993). These procedures include trimming of the images, bias subtraction, flat-fielding, cosmic rays cleaning, extraction of the spectra, wavelength calibration using as reference the observed spectra of Ar lamps and sky subtraction. The flux calibration is performed using a sensitivity function generated from the spectrum of a photometric standard. Individual datacubes for each exposure were created at an angular sampling of 0.05″×0.05″. These datacubes were then median combined using a sigma clipping algorithm to remove spurious features and the location of the continuum peak was used to perform the alignment among the cubes.

The final datacube of NGC 5643 covers the inner 5″×7″ (285×400 pc^2) at an angular resolution of 0.8″ ($\sim$45 pc), as obtained from measurement of the Full Width at Half Maximum (FWHM) of the flux distribution of the standard star. The velocity resolution is $\sim$95 km s^{-1}, as the FWHM of typical arc lamp lines used to the wavelength calibration of the spectra.

3 RESULTS

Figure 1 (on the top) shows a large scale J-band image of NGC 5643 obtained from the Two Micron All Sky Survey (2MASS; Jarrett et al., 2003). This image clearly reveals the presence of a bar oriented along the east-west direction. The top right panel of Fig. 1 shows the continuum image obtained from the GMOS datacube, by averaging the fluxes within a spectral window of 300 Å centered at 8500 Å. One can observe that the GMOS flux contours are slightly more elongated along the orientation of the bar. The bottom panels show the integrated spectra within apertures of 0.7″ diameter centered at (from the top to the bottom): the nucleus, 1.5″ east, 1.8″ southeast and 1.3″ southwest of the nucleus. The [S III]λ9069 emission line and Ca II$\lambda\lambda\lambda$8498,8542,8662 absorption triplet are identified in the nuclear spectrum. These features are used to map the gas kinematics and distribution and the stellar kinematics.

3.1 Stellar Kinematics

In order to obtain measurements of the line-of-sight velocity ($V_{los\star}$) and velocity dispersion ($\sigma_\star$) of the stars in NGC 5643, we used the penalized pixel-fitting (PPXF) method (Cappellari & Emsellem, 2004; Cappellari, 2017) to fit the Ca II$\lambda\lambda\lambda$8498,8542,8662 absorption triplet present in the galaxy spectra. As spectral templates, we used selected spectra from the stellar library of Cenarro et al. (2001), which cover the spectral range of 8348-9020Å at spectral resolution of 1.5 Å. The choice of this spectral library was done because it spans a wide range in stellar atmospheric parameters and the spectral resolution of the spectra is similar to that of our GMOS data.

Before fitting the observed spectra, we have rebinned the datacube to 0.15″×0.15″ spaxels in order to increase the signal-to-noise ratio (SNR) and allow reliable measurements. In Figure 2 we show the $V_{los\star}$ (left) and $\sigma_\star$ (right) maps for NGC 5643. The systemic velocity of the galaxy (1241 km s^{-1}, as derived in Sec. 4.1) was subtracted from the observed velocity field and the white/grey regions in the $V_{los\star}/\sigma_\star$ maps represent locations where the SNR was not high enough to obtain reliable fits of the observed spectra. At these locations, the uncertainties in $V_{los\star}$ and $\sigma_\star$ are higher than 30 km s^{-1}.

The stellar velocity field (left panel of Fig. 2) of NGC 5643 shows a projected velocity amplitude of $\sim$100 km s^{-1}, with redshifts observed to the northwest and blueshifts to the southeast. The stellar velocity dispersion map (right panel of Fig. 2) shows values ranging from 50 to 140 km s^{-1}, with the highest values seen mostly to the north and southeast of the nucleus. Surrounding the nucleus, the lowest $\sigma_\star$ are observed, delin-

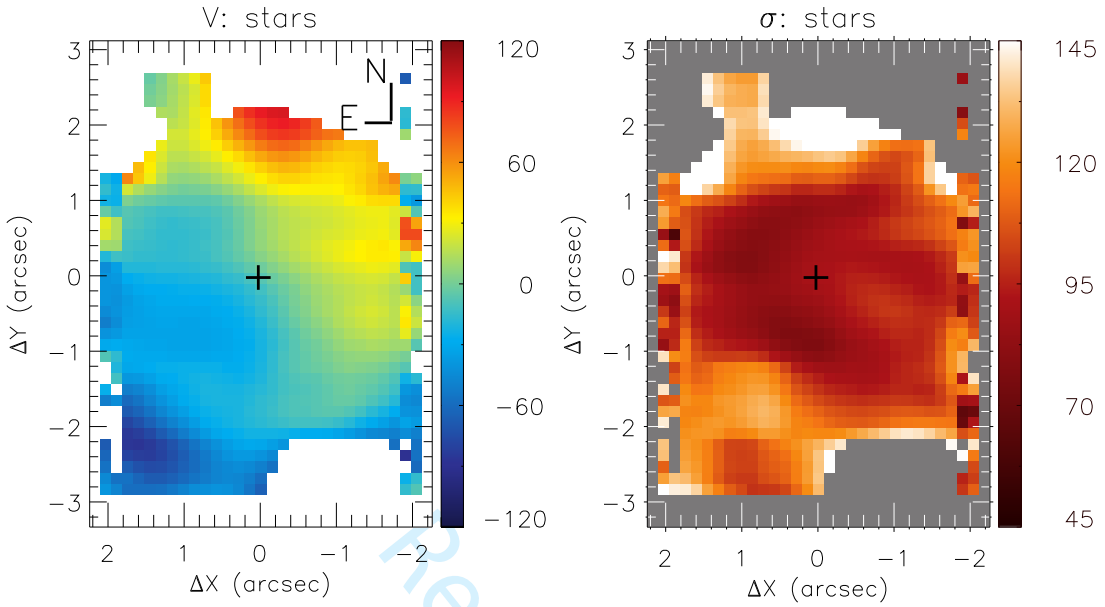

Figure 2. Stellar velocity field (left) and stellar velocity dispersion map (right). The white/grey regions in the velocity/σ_* map are masked locations due to the low SNR of the spectra. The color bars show the velocities in km s^{-1} units and the central cross marks the position of the continuum peak.

eating a partial ring with radius ∼1″.

3.2 [S III]λ9069 flux distribution and kinematics

We used the Emission-line PROfile FITting (PROFIT) routine (Riffel, 2010) to fit the observed [S III]λ9069 profile at each spaxel by Gaussian curves and obtain measurements for its flux, centroid velocity (V_{SIII}) and velocity dispersion (σ_{SIII}). Figure 3 shows the corresponding maps. The masked locations correspond to regions where the SNR of the [S III]λ9069 line was not high enough to obtain good fits. In these maps, we excluded regions farther than 1.8″ to the north and south directions, where no line emission was detected.

The top panel of Fig. 3 presents the [S III]λ9069 flux distribution, which shows an elongated structure along the east-west direction. This structure extends to up to 2.2″ to the east of the nucleus and is narrower to the west side of it, extending to 1.8″. Along the north-south direction, the [S III] shows extended emission only at locations closer than 1″ of the nucleus of the galaxy.

The [S III] velocity field is shown in the middle panel of Fig. 3, after the subtraction of the systemic velocity of the galaxy, as obtained by the fitting of the stellar velocity field by a rotation disk model (see Sec. 4.1). The highest redshifts of up to 150 km s^{-1} are seen east of the nucleus, while similar velocities in blueshifts are observed west of the nucleus.

The bottom panel of Fig. 3 shows the resulting σ_{SIII} map. The σ_{SIII} values were corrected for the instrumental broadening and range from 40 to 150 km s^{-1}. At most locations $\sigma_{SIII} \approx 90 - 120$ km s^{-1}.

The relatively high spectral resolution of the GMOS spectra has allowed us to slice the [S III] emission-line profile into a sequence of velocity bins and construct the velocity channel maps, shown in Figure 4. These maps allow a better sample of the gas kinematics over the whole velocity distribution, including the wings of the line profiles. The velocity slices within bins of ∼70 km s^{-1} (corresponding to three spectral pixels) were obtained after subtraction of the continuum, determined as averages of the fluxes from both sides of the emission line. Each panel presents flux levels in logarithmic units for the velocity slice shown. The zero velocity is adopted as the value obtained from the modeling of the stellar velocity field (Sec. 4.1). The continuous line shown in each panel of Fig. 4 represents the orientation of the line-of-nodes of the galaxy, the dotted lines delineate the bi-cone geometry, as obtained by Fischer et al. (2013) and the central cross marks the location of the nucleus.

The channel maps trace the gas from negative ve-

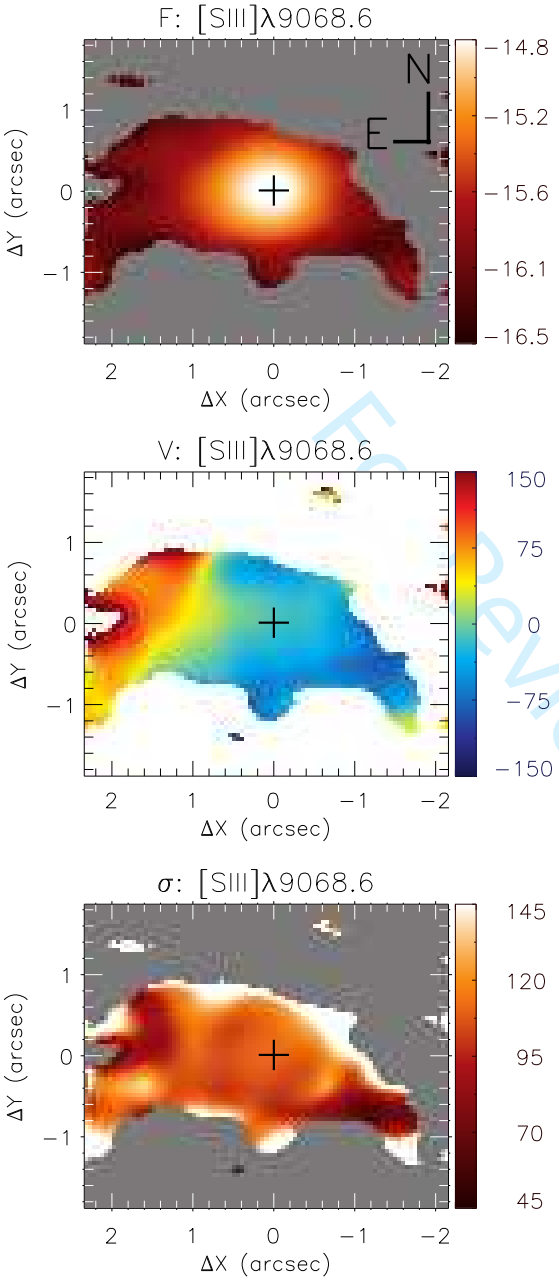

Figure 3. [S III]λ9069 flux map (top), velocity field, after the subtraction of the systemic velocity (middle) and velocity dispersion map (bottom). White and grey regions correspond to masked locations due to poor fits or non detection of the line. The fluxes are shown in logarithmic units of erg s^{-1} cm^{-2} spaxel^{-1} and the velocities are shown in km s^{-1}. The crosses mark the location of the continuum peak.

locities (blueshifts) to positive values (redshifts) relative to the systemic velocity of the galaxy. The highest blueshifts (of up to -410 km s^{-1}) and redshifts (of up to 350 km s^{-1}) are observed mainly at the nucleus of the galaxy. For smaller blueshifts, besides the nuclear emission, an elongated structure to the west-southwest is observed, co-spatial with the stripe seen in the [S III] flux map (top panel of Fig. 3). A similar redshifted structure is observed to the east. In addition, some emission northwest of the nucleus is seen in redshift, following the orientation of the major axis of the galaxy (green line), clearly seen at channel maps centered in velocities in the range 76–215 km s^{-1}. A slightly elongated structure along the major axis of the galaxy is also seen in blueshifts to the southeast, clearly observed in panels centered at -341 and -271 km s^{-1}.

4 DISCUSSIONS

4.1 Stellar Kinematics

The stellar velocity field (Fig. 2) of NGC 5643 shows a clear rotation pattern with the northwest side of the galaxy receding and the southeast side approaching, consistent with the velocity field presented by Davies et al. (2014), as obtained from the fit of the CO λ2.3 μm bands using VLT SINFONI observations. We fitted the observed $V_{\rm los\star}$ by an analytical model, under the assumption that the stars moves in circular orbits in the plane of the galaxy, within a central gravitational potential (Bertola et al., 1991). In this model, the rotation velocity field is given by:

$$V_{mod}(R,\psi) = V_s + \frac{AR\cos(\psi-\psi_0)\sin(i)\cos^p(i)}{\{R^2[\sin^2(\psi-\psi_0)+\cos^2(i)\cos^2(\psi-\psi_0)]+c_0{}^2\cos^2(i)\}^{\frac{p}{2}}}, \quad (1)$$

where R and ψ are the coordinates of each spaxel in the plane of the sky, V_s is the systemic velocity of the galaxy, A is the velocity amplitude, ψ_0 is the position angle of the major axis, i is the disc inclination relative to the plane of the sky. The p parameter measures the slope of the rotation curve where it flattens, being limited between $1 \leq p \leq 3/2$. For $p=1$ the rotation curve at large radii is asymptotically flat while for $p=3/2$ the system has a finite mass. c_0 is a concentration parameter, defined as the radius where the rotation curve reaches 70 % of its velocity amplitude.

We fitted the model to the observed velocities using the MPFITFUN routine (Markwardt, 2009) to perform a least-squares fit, in which initial guesses are given for the free parameters. As the GMOS FoV is small, the position of the kinematical center was kept fixed to the location of the continuum peak and the disc inclination was fixed to $i = 34°$ (Davies et al., 2014).

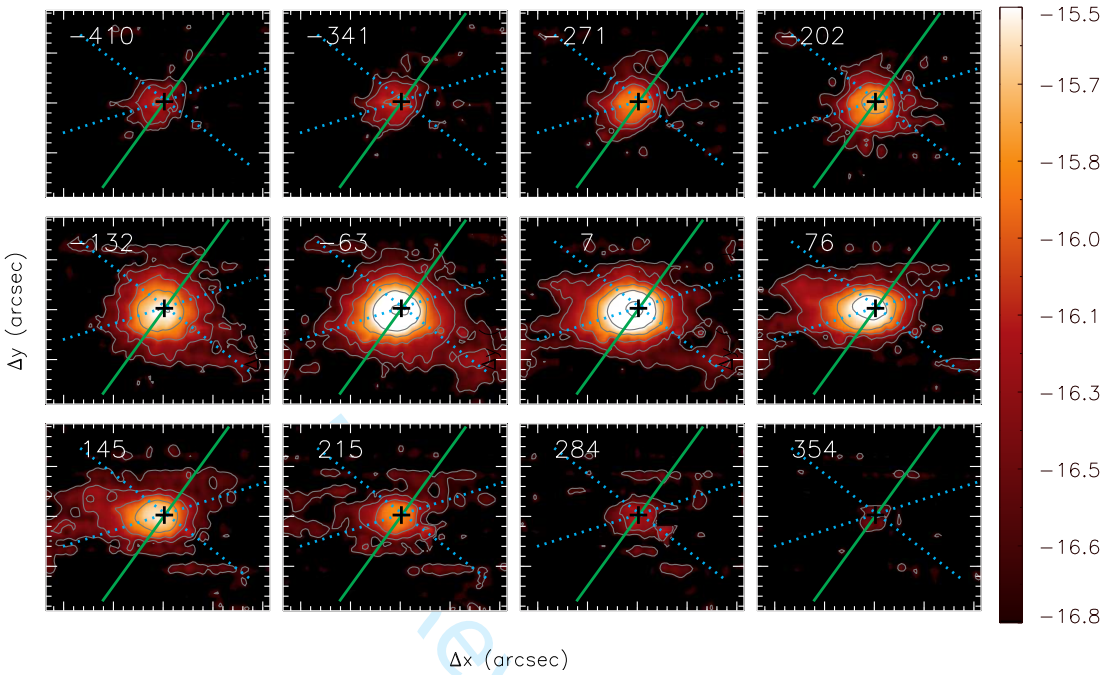

Figure 4. Velocity channel maps along the [S III]λ9069 emission-line profile for a velocity bin of $\sim$70 km s^{-1} (3 pixels). The color bar shows the fluxes logarithmic units of erg s^{-1} cm^{-2} spaxel^{-1}. The velocities relative to the systemic velocity of the galaxy are shown in the top-left corner of each panel. The continuous green lines represent the orientation of the line of nodes, as derived from the stellar velocity field. The dotted lines delineate the walls of the bi-cone, derived by Fischer et al. (2013). The central crosses mark the location of the continuum peak.

Figure 5 shows the stellar velocity field (left panel), the resulting best fit model (middle) and a residual map (right), obtained by subtracting the model from the observed velocity field. The residuals are smaller than 30 km s^{-1}at all locations, indicating that the observed velocities are well reproduced by the model.

The resulting parameters for the best fit model are: V_s = 1241 $\pm$ 7 km s^{-1}, relative to the heliocentric rest frame, A = 172 $\pm$ 22 km s^{-1}, ψ_0=−36°$\pm$ 3°, p = 1 and c_0 = 3.7″ $\pm$ 0.6″. The systemic velocity is about 40 km s^{-1} larger than the one obtained from 21 cm H I line (1199 $\pm$ 2 km s^{-1} Koribalski et al., 2004), possible due to the very distinct apertures used in the H I and GMOS observations. The orientation of the line of nodes is consistent with the value presented by Davies et al. (2014) derived from the stellar kinematics measured by fitting the CO absorption bandheads in the K-band.

The stellar velocity dispersion map (right panel of Fig. 2) shows values in the range 50–140 km s^{-1}. This range is similar to that derived using the CO absorptions at 2.3 μm presented by Hicks et al. (2013). However, their map is much noisier than ours, which reveals in addition a ring of low-$\sigma_\star$ values ($\sim$70–80 km s^{-1}) surrounding the nucleus (for which $\sigma_\star \sim$ 100 km s^{-1}) at a distance of 0.8″ ($\sim$50 pc). Similar rings have been observed for other Seyfert galaxies at scales of a few hundred parsecs and attributed to young/intermediate age stellar populations (e.g. Riffel et al., 2010, 2011, 2017; Diniz et al., 2017).

4.2 The [S III] Emission and Kinematics

The HST [O III]λ5007 image of NGC 5643 reveals a well defined triangular emission region east of the nucleus, extending to up to 1.8 kpc and showing several knots of emission (Simpson et al., 1997; Fischer et al., 2013). Their images show only a very faint emission to the west of the nucleus. This collimated structure is seen also in high resolution flux maps for the Brγ emission line, obtained from VLT SINFONI observations (Davies et al., 2014; Menezes et al., 2015). Besides the emission region east of the nucleus, the Brγ map clearly show extended emission to the west–southwest of the nucleus. Our [S III]λ9069 flux map (Fig. 3) is consistent with the [O III]λ5007 and Brγ flux maps, considering that the GMOS angular resolution is worse than that of HST and VLT–SINFONI.

The [S III] velocity field (Fig. 3) is similar to that of Brγ (Davies et al., 2014; Menezes et al., 2015), showing redshifts to the east of the nucleus and blueshifts to the west. The [O III] kinematics is modeled by a bi-cone

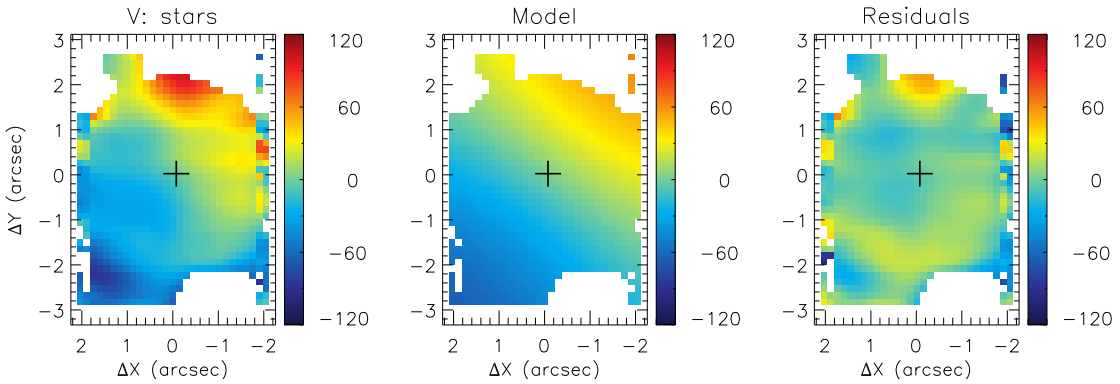

Figure 5. Left: stellar velocity field: Middle: rotating disc model for the stellar velocity field. Right: residual map between the observed and modeled velocities. The color bar shows the range of velocities in km s^{-1} and the cross marks the position of the nucleus.

with axis oriented along $PA = 80°$, being displaced by $i_{\rm cone} = 65°$ from the line-of-sight and with inner and outer opening angles of $\theta_{\rm min} = 50°$ and $\theta_{\rm max} = 55°$, respectively. Davies et al. (2014) argue that the Brγ and H_2 1–0 S(1) kinematics are consistent with this model. Besides the [S III] velocity field, the velocity channel maps are consistent with outflows within a bi-cone, as most of the redshifts and blueshifts are seen within the doted lines in Fig. 4, that delineates the geometry of the bi-cone model of Fischer et al. (2013). Thus, we conclude that the [S III] emission is originated from the same outflowing gas that originates the [O III] and Brγ emission.

Aside from the outflowing gas component, the [S III] velocity channel maps (Fig. 4) show a structure in redshifts northwest of the nucleus, extending to up to 1.5″ (observed in velocity slices from 76–215 km s^{-1}). Another slightly elongated structure is seen in blueshits to the southeast (panels centered at −341 and −271 km s^{-1}). These structures are seen at the same orientation of the kinematic major axis of the galaxy, as observed in the stellar velocity field (Fig. 2), that shows redshifts to the northwest and blueshifts to the southeast. The most plausible interpretation of these [S III] kinematic components is that they are due to emission of gas at the plane of the disc, possible heated by the outflowing gas and AGN radiation, as the bi-cone intercepts the disc plane.

Considering that the bulk of the [S III] kinematics is consistent with outflows within a bi-cone, we can use the geometric parameters of the bi-cone, in combination with our velocity measurements to estimate the mass outflow rate in ionized gas. Assuming that the redshifts seen to the east are originated from gas located in the front wall of the bi-cone, the observed projected velocity of ∼100 km s^{-1} (from Fig. 3) corresponds to outflows with velocity of $v_{\rm out} \approx 100/\sin(i_{\rm cone} - (\theta_{\rm max} - \theta_{\rm min})/2) \approx$ 330 km s^{-1}. We used the geometric parameters of the bi-cone from Fischer et al. (2013) and we note that $v_{\rm out}$ is consistent with their model (their Fig. 22). The ionized gas mass outflow rate can be estimated by

$$\dot{M} = 2\, m_p\, N_e\, A\, v_{\rm out}\, f. \qquad (2)$$

The factor 2 is included to consider both sides of the bi-cone, m_p is the proton mass, N_e is the electron density, f is the filling factor, $A = \pi r^2\,(\tan\theta_{\rm max} - \tan\theta_{\rm min})$ is the cross section of the outflow, and r is the distance from the nucleus along the bi-cone axis. Assuming typical values of $f = 0.01$ and $N_e = 500\,{\rm cm}^{-3}$ (e.g. Osterbrock & Ferland, 2006; Dors et al., 2015) and $r = 1'' \approx 50$ pc, we obtain $\dot{M} \approx 0.3\ {\rm M}_\odot\ {\rm yr}^{-1}$ for NGC 5643.

The mass outflow-rate derived for NGC 5643 is within the range of values observed in other Seyfert galaxies ($10^{-2} - 10^{1}\ {\rm M}_\odot\ {\rm yr}^{-1}$; Barbosa et al., 2009; Riffel, 2013; Revalski et al., 2018). These values are 10–100 times larger than the supermassive black hole mass accretion rates, supporting an origin in gas of the NLR.

5 CONCLUSIONS

We used GMOS IFU observations of the inner 285×400 pc^2 of the Seyfert 2 galaxy NGC 5643 to map the gas and stellar kinematics at a velocity resolution of 95 km s^{-1} (FWHM) and spatial resolution of 45 pc. Our main conclusions are:

- The [S III]λ9069 flux map shows a triangular emission region east of the nucleus, extending to up to the border of the field of view (140 pc). A more collimated structure is seen to the west-southwest to up to 100 pc from the nucleus. The [S III]λ9069 flux distribution is similar to that [O III]λ5007 and H I recombination lines, previously published.
- The [S III] kinematics is dominated by outflows within a bi-cone oriented along $PA \approx 80°$. The

projected velocity of the outflow is about 100 km s^{-1} and we derive a mass outflow rate of 0.3 M$_\odot$ yr^{-1} in ionized gas.

- Velocity channel maps along the [S III]λ9069 emission-line profile reveal a secondary kinematic component, originated from gas located in the plane of the galaxy, possible heated by the outflowing material.
- The stellar velocity field shows regular rotation with a projected velocity amplitude of 100 km s^{-1} and is well reproduced by a model of a rotating disc with major axis oriented along $\psi_0 = -36^0$.
- The stellar velocity dispersion map shows values ranging from 50 to 140 km s^{-1} and reveal a ring of low-$\sigma_\star$ values (70 km s^{-1}) surrounding the nucleus at a distance of 50 pc from it. This structure is attributed to young/intermediate age stellar populations, which still preserve the kinematics of the gas whence they were formed.

6 ACKNOWLEDGEMENTS

This work has been partially supported by the Conselho Nacional de Desenvolvimento Científico e Tecnológico (CNPq), Coordenação de Aperfeiçoamento de Pessoal de Nível Superior (CAPES) and Fundação de Amparo à Pesquisa do Estado do Rio Grande do Sul (FAPERGS). Based on observations obtained at the Gemini Observatory, acquired through the Gemini Observatory Archive and processed using the Gemini IRAF package, which is operated by the Association of Universities for Research in Astronomy, Inc., under a cooperative agreement with the NSF on behalf of the Gemini partnership: the National Science Foundation (United States), the National Research Council (Canada), CONICYT (Chile), Ministerio de Ciencia, Tecnología e Innovación Productiva (Argentina), and Ministério da Ciência, Tecnologia e Inovação (Brazil).

REFERENCES

Allington-Smith J., et al., 2002, PASP, 114, 892
Antonucci R., 1993, ARA&A, 31, 473
Barbosa F. K. B., Storchi-Bergmann T., Cid Fernandes R., Winge C., Schmitt H., 2009, MNRAS, 396, 2
Bertola F., Bettoni D., Danziger J., Sadler E., Sparke L., de Zeeuw T., 1991, ApJ, 373, 369
Bianchi S., Guainazzi M., Chiaberge M., 2006, A&A, 448, 499
Brum C., Riffel R. A., Storchi-Bergmann T., Robinson A., Schnorr Müller A., Lena D., 2017, MNRAS, 469, 3405
Cappellari M., 2017, MNRAS, 466, 798
Cappellari M., Emsellem E., 2004, PASP, 116, 138
Cenarro A. J., Cardiel N., Gorgas J., Peletier R. F., Vazdekis A., Prada F., 2001, MNRAS, 326, 959
Davies R. I., et al., 2014, ApJ, 792, 101
Diniz M. R., Riffel R. A., Riffel R., Crenshaw D. M., Storchi-Bergmann T., Fischer T. C., Schmitt H. R., Kraemer S. B., 2017, MNRAS, 469, 3286
Dors O. L., Cardaci M. V., Hägele G. F., Rodrigues I., Grebel E. K., Pilyugin L. S., Freitas-Lemes P., Krabbe A. C., 2015, MNRAS, 453, 4102
Fischer T. C., Crenshaw D. M., Kraemer S. B., Schmitt H. R., 2013, ApJS, 209, 1
Fischer T. C., et al., 2017, ApJ, 834, 30
Freitas I. C., et al., 2018, MNRAS, 476, 2760
Hicks E. K. S., Davies R. I., Maciejewski W., Emsellem E., Malkan M. A., Dumas G., Müller-Sánchez F., Rivers A., 2013, ApJ, 768, 107
Hook I. M., Jørgensen I., Allington-Smith J. R., Davies R. L., Metcalfe N., Murowinski R. G., Crampton D., 2004, PASP, 116, 425
Jarrett T. H., Chester T., Cutri R., Schneider S. E., Huchra J. P., 2003, AJ, 125, 525
Koribalski B. S., et al., 2004, AJ, 128, 16
Lena D., 2014, preprint, (arXiv:1409.8264)
Lena D., Robinson A., Storchi-Bergmann T., Couto G. S., Schnorr-Müller A., Riffel R. A., 2016, MNRAS, 459, 4485
Markwardt C. B., 2009, in Bohlender D. A., Durand D., Dowler P., eds, Astronomical Society of the Pacific Conference Series Vol. 411, Astronomical Data Analysis Software and Systems XVIII. p. 251 (arXiv:0902.2850)
Medling A. M., et al., 2015, MNRAS, 448, 2301
Menezes R. B., da Silva P., Ricci T. V., Steiner J. E., May D., Borges B. W., 2015, MNRAS, 450, 369
Osterbrock D. E., Ferland G. J., 2006, Astrophysics of gaseous nebulae and active galactic nuclei
Phillips M. M., Charles P. A., Baldwin J. A., 1983, ApJ, 266, 485
Revalski M., Crenshaw D. M., Kraemer S. B., Fischer T. C., Schmitt H. R., Machuca C., 2018, ApJ, 856, 46
Riffel R. A., 2010, Ap&SS, 327, 239
Riffel R. A., 2013, Boletin de la Asociacion Argentina de Astronomia La Plata Argentina, 56, 13
Riffel R. A., Storchi-Bergmann T., Winge C., Barbosa F. K. B., 2006, MNRAS, 373, 2
Riffel R. A., Storchi-Bergmann T., Riffel R., Pastoriza M. G., 2010, ApJ, 713, 469
Riffel R., Riffel R. A., Ferrari F., Storchi-Bergmann T., 2011, MNRAS, 416, 493
Riffel R. A., Storchi-Bergmann T., Winge C., 2013, MNRAS, 430, 2249
Riffel R. A., Storchi-Bergmann T., Riffel R., 2015, MNRAS, 451, 3587
Riffel R. A., Storchi-Bergmann T., Riffel R., Dahmer-Hahn L. G., Diniz M. R., Schönell A. J., Dametto N. Z., 2017, MNRAS, 470, 992

Sandage A., 1978, AJ, 83, 904
Schmitt H. R., Storchi-Bergmann T., Baldwin J. A., 1994, ApJ, 423, 237
Schmitt H. R., Donley J. L., Antonucci R. R. J., Hutchings J. B., Kinney A. L., Pringle J. E., 2003, ApJ, 597, 768
Simpson C., Wilson A. S., Bower G., Heckman T. M., Krolik J. H., Miley G. K., 1997, ApJ, 474, 121
Thomas A. D., et al., 2017, ApJS, 232, 11
Tody D., 1986, in Crawford D. L., ed., Proc. SPIEVol. 627, Instrumentation in astronomy VI. p. 733, doi:10.1117/12.968154
Tody D., 1993, in Hanisch R. J., Brissenden R. J. V., Barnes J., eds, Astronomical Society of the Pacific Conference Series Vol. 52, Astronomical Data Analysis Software and Systems II. p. 173
Urry C. M., Padovani P., 1995, PASP, 107, 803
Wilson A. S., Tsvetanov Z. I., 1994, AJ, 107, 1227
Wylezalek D., et al., 2017, MNRAS, 467, 2612
de Vaucouleurs G., de Vaucouleurs A., Corwin J. R., 1976, in Second reference catalogue of bright galaxies, Vol. 1976, p. Austin: University of Texas Press..